Electrical detection of Rydberg interactions in nitric oxide at room temperature

Von der Fakultät Mathematik und Physik der Universität Stuttgart
zur Erlangung der Würde eines Doktors der Naturwissenschaften
(Dr. rer. nat.) genehmigte Abhandlung

vorgelegt von

Fabian Munkes

aus Stuttgart

Hauptberichter:	Prof. Dr. Tilman Pfau
Mitberichter:	Prof. Dr. Jens Anders
Prüfungsvorsitzender:	Prof. Dr. Mathias Scheurer
Tag der mündlichen Prüfung:	15. Dezember 2023

5. Physikalisches Institut
Universität Stuttgart
2023

Zusammenfassung

In dieser Arbeit wird die Detektion von Rydbergzuständen Stickstoffmonoxids (NO) bei Raumtemperatur gezeigt. Die Detektion basiert auf der Messung durch freie Ladungen erzeugter kleinster Ströme, wobei die Ladungen durch Stoßionisation entstehen.

Rydbergzustände sind Zustände eines Atoms oder Moleküls, die durch die besonders hohe Anregung mindestens eines Valenzelektrons beschrieben werden können. Die mathematische Beschreibung eines solchen Zustandes ist insbesondere dann einfach, wenn lediglich ein einzelnes Valenzelektron angeregt wird, da die Beschreibung dadurch der des Wasserstoffatoms ähnelt. Bildlich gesprochen, befindet sich das einzelne Valenzelektron in einem großen Abstand zum Restatom oder –molekül, bestehend aus dem Kern und weiteren Elektronen. Das wiederum führt oftmals dazu, dass einzelne Übergänge bekannt sind, was die jeweilige Spezies attraktiv für Spektroskopieexperimente macht. Klassische Beispiele für Atome, mit welchen Spektroskopieexperimente basierend auf Rydbergzuständen durchgeführt werden, sind die Alkalielemente Rubidium (Rb) und Cäsium (Cs). Moleküle wie Kohlenstoffmonoxid (CO) [1, 2] und das für diese Arbeit relevante NO [3, 4] lassen sich ebenfalls mittels Laseranregungen in einen Rydbergzustand versetzen. Allen gemein ist, dass sie jeweils nur ein einziges freies Valenzelektron besitzen.

Die Detektion der hoch angeregten Zustände kann beispielsweise optisch durch die Nutzung von elektromagnetisch induzierter Transparenz erfolgen, welche auf der Detektion der Fluoreszenz des zerfallenden Zustandes basiert [5–7]. Eine andere häufig genutzte Variante ist die selektive Feldionisation, wobei hier ein immer größer werdendes Feld angelegt wird. Die Detektion selbst erfolgt durch Mikrokanalplatten, welche kleinste Ströme freier Ladungen mittels eines Lawinenprozesses verstärken [3, 4]. Dieser Detektortyp kann nur bei kleinstem Hintergrunddruck verwendet werden.

Die in dieser Arbeit genutzte Methodik hingegen unterscheidet sich von den typischerweise genutzten, und wurde innerhalb der letzten Jahre am 5. Physikalischen Institut in Kooperation mit dem Institut für Intelligente Sensorik und Theoretische Elektrotechnik (IIS), sowie dem Institut für Großflächige Mikroelektronik (IGM) an der Universität Stuttgart für die Detektion von Rydbergzuständen in Rubidium

entwickelt [7–13]. In einer Machbarkeitsstudie wurde zudem gezeigt, dass das Prinzip auf NO übertragen werden kann [14, 15]. Die Idee ist, dass eine Messzelle aus Glas mit Elektroden so ausgestattet wird, dass ein mit Hilfe der Elektroden erzeugtes elektrisches Feld freie Ladungen separiert, und ein anschließender Schaltkreis den entstehenden Strom verstärkt und in ein Spannungssignal konvertiert. Die freien Ladungen entstehen durch Stoßionisation der Rydbergteilchen mit einem anderen Teilchen des Hintergrundgases. Hierbei wird ausgenutzt, dass Rydbergzustände besonders leicht ionisieren, da das angeregte Elektron nur noch sehr schwach an das Restatom oder –molekül gebunden ist. Die Rydbergzustände selbst werden durch Laseranregung erzeugt, wobei in dieser Arbeit ausschließlich Dauerstrichlaser verwendet werden, um die Linienbreite kleinzuhalten. Der notwendige Schaltkreis basiert auf einem sogenannten Transimpedanzverstärker, welcher den Strom in ein Spannungssignal konvertiert und verstärkt.

Der für diese Arbeit notwendige experimentelle Aufbau besteht aus vier Hauptkomponenten, dem Gasmischsystem, dem optischen Aufbau, dem Frequenzstabilisierungsaufbau, sowie der Glaszelle. Das Gasmischsystem erlaubt definierte Konzentration von reinem NO, oder NO verdünnt in Stickstoff (N_2), herzustellen. Es wurde innerhalb einer vorherigen Promotion entwickelt [16]. Das entstandene Gasgemisch strömt nun durch die Messzelle, in welcher die Rydberganregungen von NO stattfinden. Hierzu werden insgesamt drei unterschiedliche Dauerstrichlasersysteme verwendet, welche die molekularen Übergänge $\mathrm{A}\,^2\Sigma^+ \leftarrow \mathrm{X}\,^2\Pi_{3/2}$, $\mathrm{H}\,^2\Sigma^+ \leftarrow \mathrm{A}\,^2\Sigma^+$ und $n(N^+) \leftarrow \mathrm{H}\,^2\Sigma^+$ treiben. Diese Übergänge liegen grob bei den Wellenlängen 226 nm, 540 nm und 835 nm. Im Allgemeinen verändert sich die Frequenz eines Lasers über die Zeit. Da die Übergänge jedoch nur dann angeregt werden, solange der Laser die korrekte Frequenz besitzt, müssen selbige stabilisiert wird. Dies geschieht über einen separaten optischen und technischen Aufbau zur Frequenzstabilisierung. Hierzu wurde innerhalb dieser Arbeit eine Software basierend auf PyRPL [17] entwickelt, welche das komfortable Stabilisieren mehrerer Lasersysteme ermöglicht. Zudem wurde der optische Aufbau der Stabilisierung so gewählt, dass er zukünftig leicht um weitere zu stabilisierende Laser erweitert werden kann. Die im Kapitel 5 vorgestellten Ergebnisse basieren alle darauf, dass die Laser der unteren beiden Übergänge auf eine bestimmte Wellenlänge stabilisiert werden, und der Rydberglaser kontinuierlich um einen gewissen Wellenlängenbereich verändert wird. Somit wird der Stabilisierungsaufbau bei diesem zur Frequenzreferenzierung basierend auf einem in der Länge stabilisierten Fabry–Pérot–Interferometer verwendet, wobei die Ungenauigkeit $2\pi \times 2.5\,\mathrm{MHz}$ beträgt. Der optische Aufbau an der Zelle selbst ist einfach, wobei der Laser des ersten Überganges entgegen der Richtung aber entlang der Achse des zweiten und dritten Lasers die Zelle passiert, um die Auswirkungen des Dopplereffektes gering zu halten. Typische Linienbreite im Rydbergzustand sind hierdurch $2\pi \times 130\,\mathrm{MHz}$.

Die Glaszelle ist das Herzstück des experimentellen Aufbaus und wurde innerhalb dieser Arbeit komplett neu entwickelt. Sie hat mittig einen nach oben und unten offenen Quader, wobei der Glasrahmen aus Borosilikat gefertigt ist. Es wird sich zunutze gemacht, dass es möglich ist, Platinen mittels eines Vakuumepoxies an den Glasrahmen zu kleben. An den Lasereintrittspunkten vorne und hinten wird ein Loch in den Glasrahmen gebohrt, um Quartzfenster aufzukleben, welche eine Transmission im Ultravioletten ermöglichen. Dies ist notwendig, da ansonsten eine Transmission bei 226 nm durch das Glas nicht gegeben wäre. Links und rechts ist der Glasrahmen mit Anschlussflanschen versehen, um eine Verbindung mit dem Gasmischsystem beziehungsweise den Vakuumpumpen herzustellen.

In dieser Arbeit werden zwei Schaltkreise vorgestellt, welche auf Platinen realisiert wurden. Beide Schaltkreise wurden in Zusammenarbeit mit dem IIS entwickelt. Oben auf den Quader wird die Platine geklebt, wohingegen auf die Unterseite eine Kupferplatte geklebt wird. Die Kupferplatte dient als Gegenelektrode. Die obige Platine ist mit einer Elektrode versehen, welche in die Zelle zeigt. Auf der anderen Seite der Platine ist die Ausleseelektronik, welche auf einem Transimpedanzverstärker basiert. Insbesondere die Nutzung eines sogenannten Guard–Rings in einer zweiten Version der Zelle brachte den erwünschten Effekt, dass möglichst homogene Felder erzeugt werden können, und gleichzeitig unerwünschte Nebeneffekte wie starkes Rauschen im Ausgangssignal unterdrückt werden. Zudem zeigt diese Arbeit auf, wie wichtig eine Abwägung zwischen Geschwindigkeit der Ausleseelektronik und Stabilität des verwendeten Schaltkreises ist.

In einem Großteil dieser Arbeit wird sich mit der Rydbergphysik NOs befasst. Zu Beginn des Projektes waren die erreichbaren Rydbergzustände $n(N^+)$ noch nicht klar. Mittels Messungen von Rydbergspektren zweier Rotationsserien wird gezeigt, dass das Anregungsschema verstanden ist. Hierzu wird der Abstand der jeweiligen Ionisationsgrenzen mit dem theoretisch zu erwartenden verglichen.

In einem weiteren Teil wird der Stark–Effekt von Rydbergzuständen in NO untersucht. Der Stark–Effekt selbst beschreibt die Aufspaltung energetischer Zustände durch das Anlegen eines elektrischen Feldes. Obwohl es in der Literatur zahlreiche Experimente zu Rydbergzuständen in NO gibt, beispielsweise [3, 4, 18], so finden diese zumindest unseres Wissens nach ausschließlich mit gepulsten Lasern statt. Die Ergebnisse dieser Arbeit weisen unserem Wissen nach eine bisher nicht vorhandene Auflösung auf. Insbesondere lässt sich die Aufspaltung auch bei kleinsten Feldern messen. Mit den Ergebnissen erhoffen wir uns zukünftig, den Quantendefekt von Rydberg–g–Zuständen zu präzisieren. Dieser ist in der Literatur lediglich in einem gewissen Bereich bekannt [19, 20]. Die Theorie zu diesen Ergebnissen wird innerhalb einer Kooperation mit Prof. Stephen Hogan und Matthew Rayment vom University College London erstellt, welche innerhalb dieser Promotion aufgebaut wurde.

Im letzten Teil wird sich mit der Verbreiterung und relativen Verschiebung von Rydbergzuständen in NO bei steigender Dichte des Hintergrundgases befasst. Das Experiment wurde einmal bei steigendem Druck von NO selbst, sowie bei steigendem Druck von N_2 durchgeführt. Diese Art von Experiment hat eine lange Geschichte in Alkalielementen [21–24], jedoch wurde solch ein Experiment nach unserem Stand nie mit NO durchgeführt. Die Ergebnisse werden unter anderem mithilfe der Theorie Fermis erklärt [21], wobei zusätzliche Effekte durch die komplexere Struktur von Molekülen gedeutet werden. Die Ergebnisse dieses Teils wurden in einer Veröffentlichung zusammengefasst [25].

Während sich diese Arbeit hauptsächlich mit fundamentalen Ergebnissen der Rydbergphysik in NO beschäftigt, so basiert die Ursprungsidee des Projektes darauf, einen Atemgassensor für NO zu realisieren. Anfang der 1990er Jahre wurde gezeigt, dass NO Teil der Ausatemluft mit einer Konzentration von ungefähr 8 ppb ist [26]. Vorherige Forschung hatte gezeigt, dass NO eine wichtige Rolle in der Zellkommunikation von Säugetieren spielt [27–30], was 1998 mit dem Nobelpreis für Physiologie oder Medizin [31] belohnt wurde. Weitere Studien ergaben, dass die NO–Konzentration in der Ausatemluft einen Hinweis auf Krankheiten wie Asthma, Atopien oder beispielsweise Lungenkrebs geben kann [32]. Bereits verfügbare Sensoren benötigen jedoch große Volumina, ungefähr 300 mL, über einen Zeitraum von mehreren Sekunden [32]. Das Volumen des hier vorgestellte Messprinzips allerdings ist lediglich durch die Laserstrahlgröße begrenzt, was es auch für die medizinische Forschung interessant macht. Die in dieser Arbeit vorgestellte Zelle ist auf die Homogenität des elektrischen Feldes optimiert. In zukünftigen Zelldesigns kann ein stärkerer Fokus auf die Ausleseeffizienz und –sensitivität gelegt werden. Diese Arbeit liefert die hierfür geeigneten Dichte– und Feldbereiche.

Abstract

In this work I will present measurements of Rydberg states in nitric oxide (NO) at room temperature. The detection of the Rydberg states is realized by measuring the current of free charges resulting from collisions of the excited molecules. All measurements are performed using continuous–wave (cw) lasers in a sub–Doppler configuration, which together with a stabilization setup yield a frequency error of only $2\pi \times 2.5\,\mathrm{MHz}$. The full width at half maximum (FWHM) of a typical Rydberg state is only about $2\pi \times 130\,\mathrm{MHz}$.

We take a look at the necessary theory of diatomic molecules first. Afterward, a thorough walkthrough of the experimental setup is given. The heart of our setup is a custom–designed measurement cell, which features readout electronics based on a transimpedance amplifier (TIA). As such I will also give an overview on the basics of operational amplifiers (OpAmps).

When all prerequisites are introduced, we will take an in-depth look on the Stark effect in Rydberg states. To our knowledge, the presented resolution is unmatched, and may enable us to give a more precise value to the g–quantum defect in NO in the future. In a final experimental section I show the collisional broadening and shift of Rydberg states of NO due to an increasing background gas density. Such measurements have a long history in alkalis, yet to our knowledge, no such measurements in NO exist.

The overall experiment is performed in the context of a trace–gas sensor for NO in a medical application. This work gives suitable density and electric field ranges for such a sensor.

List of abbreviations

AC	alternating current
AOM	acousto–optic modulator
Ar	argon
ASG	arbitrary signal generator
ASIC	application–specific integrated circuit
BBO	β barium borate crystal
CMOS	complementary metal–oxide–semiconductor
CMRR	common-mode rejection ratio
CO	carbon monoxide
Cs	cesium
cw	continuous–wave (lasers)
DC	direct current
EIT	electromagnetically induced transparency
EOM	electro-optic modulator
ESD	electrostatic discharge
FPGA	field–programmable gate array
FPI	Fabry–Pérot interferometer
FSR	free spectral range
FWHM	full width at half maximum
GBW	gain–bandwidth product
GMU	gas mixing unit
H_2	hydrogen (molecule)
H_2O	water
He	helium

IC	integrated circuit
IGM	Institute for Large Area Microelectronics/ Institut für Großflächige Mikroelektronik, University of Stuttgart
IIS	Institute of Smart Sensors/ Institut für Intelligente Sensorik und Theoretische Elektrotechnik, University of Stuttgart
IR	infrared
K	potassium
KF	Kleinflansch
LBO	lithium triborate crystal
MCP	micro–channel plate
MEPR	multi–element pseudo resistor
MFC	mass–flow controller
MQDT	multichannel quantum defect theory
N_2	nitrogen
Na	sodium
Ne	neon
NO	nitric oxide
NO_2	nitrogen dioxide
OpAmp	operational amplifier
PBSC	polarizing beam splitter cube
PCB	printed circuit board
PDH	Pound–Drever–Hall technique
PID	proportional–integral–derivative controller
PPLN	periodically–poled lithium niobate crystal
PSD	power spectral density
Rb	rubidium
REMPI	resonance–enhanced multiphoton ionization
RF	radio–frequency
RP	Red Pitaya STEMlab 125-14
SFDR	spurious–free dynamic range

SFI	selective field ionization
SNR	signal–to–noise ratio
TA	tapered amplifier
Ti:sa	titanium–sapphire laser
TIA	transimpedance amplifier
UCL	University College London
ULE	ultra-low expansion cavity
UV	ultraviolet (radiation)
Xe	xenon

Contents

1 Introduction

States of a molecule or atom, where at least one electron has a particularly high principal quantum number n, are called Rydberg states. Their mathematical treatment is easy, if only a single electron is excited to a high state, since they then can be described approximately hydrogenic. As such they are interesting for spectroscopic experiments, as individual transitions in the molecule or atom are oftentimes clearly known. One may simply picture a Rydberg state as a state, where a single electron is at a large distance from the nucleus. Typical examples for atoms, where Rydberg states are investigated, are alkalis such as rubidium (Rb) or cesium (Cs), as they only have a single valence electron. Some molecules like carbon monoxide (CO) [1, 2], nitric oxide (NO) [3, 4], and others also hold laser accessible Rydberg states of a single electron.

A typical way of detecting a coherently excited Rydberg state is the optical detection via electromagnetically induced transparency (EIT) [5–7], based on the fluorescence of the decaying Rydberg state. Another way uses selective field ionization (SFI), where an electric field is ramped up causing ionization. Here, a detector like a micro–channel plate (MCP), which is based on an avalanche process, yields the signal [3, 4]. These kinds of detectors are used, if low background pressures are ensured.

However, the approach used in this work is based on the collisional ionization of Rydberg states and detecting the resulting free charges by guiding them to electrodes and amplifying the current. In [8] an electrically contacted vapor cell to measure Rydberg states of Rb at room temperature was introduced, and [7] shows the striking difference in measurement simplicity and signal–to–noise ratio, when comparing the signal obtained by EIT versus the signal gained by the electrical detection of the Stark effect of the 42S state. In particular, the optical measurement required a lock–in amplifier and averaging for 15 min, whereas the electrical measurement was performed in a single shot.

The overall cell design and readout principle for Rydberg states of Rb and Cs at room temperature were investigated during the PhD of Renate Daschner [9, 10]. Here, the cells were equipped with electrodes on glass manufactured at the Institute for Large Area Microelectronics (IGM) at the University of Stuttgart, while the amplification electronics were external. The glass substrates themselves were bonded to the cell,

and the cell was sealed. The pressure of Rb or Cs within the cell volume was adjusted by an oven. Johannes Schmidt [11] refined the cell design during his PhD, and the electronics for the current amplification were integrated on the cell for the first time [12, 13]. Different designs were tested. For some the amplification electronics were part of the glass structure, and for others a custom–designed amplifier by the Institute of Smart Sensors (IIS) [33] was used. Additionally, through–flow measurements with background gases like nitrogen (N_2) and argon (Ar) were performed. Johannes Schmidt showed in a proof–of–concept experiment, that the readout principle is transferable to Rydberg states of NO [14, 15], where the Rydberg states where generated at room temperature by pulsed laser excitation in the group of Edward Grant at the University of British Columbia, Vancouver, Canada.

The proof–of–principle experiment is the base for research presented by my colleague Patrick Kaspar in his PhD thesis [16, 34], as well as in this thesis. NO is interesting from a fundamental physics point of view, as for example the existence of Rydberg bimolecules were recently predicted [35]. Yet NO is relevant from a medical point of view as well, which ultimately lead to the experiment at hand.

In 1998 the Nobel Prize in Physiology or Medicine was awarded to Ferid Murad, Robert F. Furchgott and Louis J. Ignarro [31], who showed that NO plays an important role in the mammalian system [27–30]. In subsequent years a broad field of research was built [30]. Research was done on different forms of cancer [36–39], as well as on general biological processes such as immunological responses, inflammation or apoptosis [40]. It was shown that NO plays a role as signaling molecule, in the cardiovascular system, the blood system, the respiratory cycle and is generated when defending tumor cells, bacteria or viruses [41].

In 1991, research proved that NO is also part of the exhaled breath [26] ($\approx$ 8 ppb), and subsequent research revealed that the NO concentration in exhaled breath changes when diseases like asthma, atopy and others are present [32]. This makes the breath gas analysis of NO relevant.

Besides giving a guide to what the demands on a sensor for NO are, [32] also describes how NO levels typically are measured in a clinical context. The patient has to inhale for about 2 s to 3 s and afterward exhale for at best 10 s at a constant flow to deliver about 300 mL of exhaled volume for further analysis, e. g. by mass spectrometry. When thinking about medical research, such large air volumes are not always available.

Our sensor scheme is visualized in figure 1.1. The heart of the setup is a glass cell with electrodes attached to top and bottom. The counterside of the top electrode is equipped with an electrical circuit for amplification. When a gas mixture of an

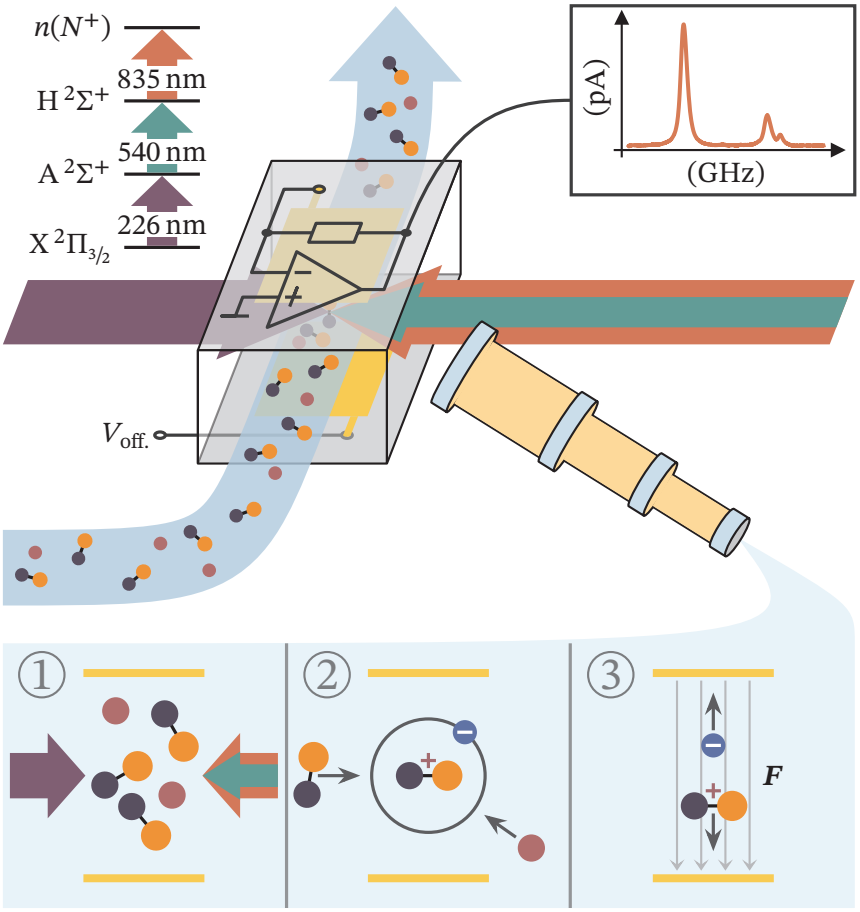

Figure 1.1: Sketch of the sensor principle. A gas mixture of NO and possibly other particles passes through a glass cell. **1.** The NO molecules are excited to a Rydberg state $n(N^+)$ via a three-photon excitation scheme shown on the top left, which is based on cw lasers. **2.** The molecules ionize by collisions with other particles. **3.** The charges are separated by a small potential $V_{off.}$ applied to the cell's electrodes, and on–cell electronics convert and amplify the current to a voltage signal.

unknown concentration of NO passes through the cell, the actual detection is performed in three steps. In a first step NO is excited to a Rydberg state $n(N^+)$ via a continuous–wave (cw) three–photon excitation scheme depicted on the top left. The involved wavelengths of the lasers are $\lambda_{A\leftarrow X} = 226\,\text{nm}$, $\lambda_{H\leftarrow A} = 540\,\text{nm}$ and $\lambda_{n(N^+)\leftarrow H} = 835\,\text{nm}$. In the second step the excited molecules ionize by collisions with other particles. In the final step the actual detection of the free charges happens, as a small potential applied to the electrodes guides the charges to them. The generated current is amplified and converted to a voltage.

This detection scheme does not have the disadvantages previously mentioned, such as the requirements on the air volume and the detection time. The required gas volume is in principle only limited by the volume of the smallest laser beam, which is in this work about 16 mL, but can in principle be made smaller. The selectivity is based on the amount of false positives measured. A high selectivity corresponds to a high sensitivity, as in the best case the sensor is only sensitive to a single particle. In our case the excitation scheme can be understood as a fingerprint of the molecule. It is basically impossible to excite any other particle to a Rydberg state with the shown scheme, as long as the laser linewidths are small. This is ensured by using cw lasers. The bandwidth of the sensor is essentially limited by the rate of the gas exchange. A proof–of concept experiment showed, that operation at ambient pressure is possible [14].

This work shows insights on Rydberg physics in NO, which is important background knowledge for the proposed trace–gas sensor for NO. As an example the substructure of the individual states clearly decides, which particular transitions (or wavelengths) are the most promising for a high signal–to–noise ratio (SNR) in the final sensor.

The thesis is outlined in the following way. At first an introduction to the general physics of diatomic molecules is given. In contrast to atoms, molecules have additional degrees of freedoms, namely rotation and vibration, which results in a richer energy structure. A large focus is taken on the theory of Rydberg states in NO. Next, the experimental setup is explained, showing the different laser systems, the gas mixing unit (GMU) and the frequency–stabilization setup. The glass cells used for readout are treated in their own chapter, where the electronics used are explained as well. The amplification and conversion of the readout current to a voltage is realized via a transimpedance amplifier (TIA). Thus, a more detailed look on the required electronic knowledge is taken, explaining the basics of operational amplifiers (OpAmps) and TIAs. The main results are in the final chapter, where we look at the splitting of Rydberg states of NO being subject to the Stark effect, as well as the shift and broadening of the spectroscopic lines with increasing pressure. These insights allow choosing particular sweet spots for the sensor. Additionally, they may be seen as a test bench for future cell designs and measurements.

2 The electronic structure of nitric oxide

2.1 Theoretical basics for diatomic molecules

This section summarizes the theory necessary to describe the physics in heteronuclear diatomic molecules like NO. It is based on [42–46]. In contrast to atoms, molecules have additional degrees of freedom, namely rotation and vibration. Thus, it is necessary to introduce new quantum numbers, and the rules which quantum numbers (or basis) diagonalize the Hamiltonian and which won't differ significantly. We refer to them as "good" or "bad" throughout this work. A strong dependence on a particular state might be present [47].

The Schrödinger equation for a diatomic molecule can be written as [42]:

$$\frac{1}{m_\mathrm{e}} \sum_i \Delta_{\mathrm{e},\,i} \psi + \sum_{j=1}^{2} \frac{1}{m_{\mathrm{n},\,j}} \Delta_{\mathrm{n},\,j} \psi + \frac{2}{\hbar^2} (E - V) \psi = 0 \tag{2.1}$$

Here, m_e is the electron mass, $m_{\mathrm{n},\,i}$ are the masses of the nuclei, E is the energy, $\hbar$ is the reduced Planck constant and V is the potential. The respective Laplace operators Δ act on either individual electrons or nuclei. The solution of equation (2.1) is in general not possible. However, Born and Oppenheimer show in [48] the ansatz of a product wavefunction

$$\psi = \psi_\mathrm{e}(\boldsymbol{r}_i) \cdot \psi_\mathrm{n}(\boldsymbol{r}_j) \quad , \tag{2.2}$$

is justified in very good approximation. The ansatz separates the wavefunction ψ in an electronic contribution ψ_e and nuclear contribution ψ_n. This is the result of the vast difference between the mass of an electron and the mass of the nucleus. $\boldsymbol{r} = (x, y, z)$ is the respective spatial coordinate. Equation (2.1) can then be rewritten

as [42]

$$\frac{1}{m_\mathrm{e}} \sum_i \Delta_{\mathrm{e},\,i} \psi_\mathrm{e} + \frac{2}{\hbar^2} \left(E_\mathrm{el} - V_\mathrm{e}\right) \psi_\mathrm{e} = 0 \quad , \tag{2.3a}$$

$$\sum_{j=1}^{2} \frac{1}{m_{\mathrm{n},\,j}} \Delta_{\mathrm{n},\,j} \psi_\mathrm{n} + \frac{2}{\hbar^2} \left(E - \left(E_\mathrm{el} + V_\mathrm{n}\right)\right) \psi_\mathrm{n} = 0 \quad . \tag{2.3b}$$

In equation (2.3a) the electrons are moving under the potential V_e and fixed nuclei. Note, that the potential V_e is a function of all involved electronic coordinates. In equation (2.3b) the nuclei are moving under the potential $E_\mathrm{el} + V_\mathrm{n}$, which is approximately the potential energy of the vibrational motion of the nuclei [42]. The nuclear Coulomb potential is

$$V_\mathrm{n} = \frac{1}{4\pi\epsilon_0} \frac{Z_1 Z_2 e^2}{r_b} \quad , \tag{2.4}$$

where Z_1 and Z_2 are the proton numbers, e is the elementary charge, ϵ_0 is the vacuum permittivity, and r_b is the distance of the nuclei. A bound electronic state exists, if the potential $E_\mathrm{el} + V_\mathrm{n}$ has a minimum. The electronic state lowest in energy is called ground state and chosen as zero of the energy axis. The total energy of a diatomic molecular state can be approximately written as [42]

$$E = E_\mathrm{e} + E_\mathrm{vib} + E_\mathrm{rot} \quad , \tag{2.5a}$$

$$T \equiv \frac{E}{hc} = T_\mathrm{e} + G + F \quad , \tag{2.5b}$$

where E_e is the electronic energy, the vibrational energy is given by E_vib and the rotational contribution is E_rot. In molecular physics it is common to give the energy in units of wavenumbers, i. e. dividing the energy by Planck constant h and speed of light c. Thus, $T_\mathrm{e} = E_\mathrm{e}/hc$, $G = E_\mathrm{vib}/hc$ and $F = E_\mathrm{rot}/hc$.

Next we look at the different contributions in equation (2.5b).

2.1.1 Vibrational structure

Due to the introduced separation the rotation of the molecule can be ignored at first. The molecular potential $V(r_b) \equiv E_\mathrm{e} + V_\mathrm{n}$ in equation (2.3b) has to be modeled. It depends on the bound distance r_b of the two involved atoms. The closer the atoms, the larger the repulsion must be, and vice versa, due to the Coulomb interaction. Hence, the potential must be asymmetric. An empirically found potential in good

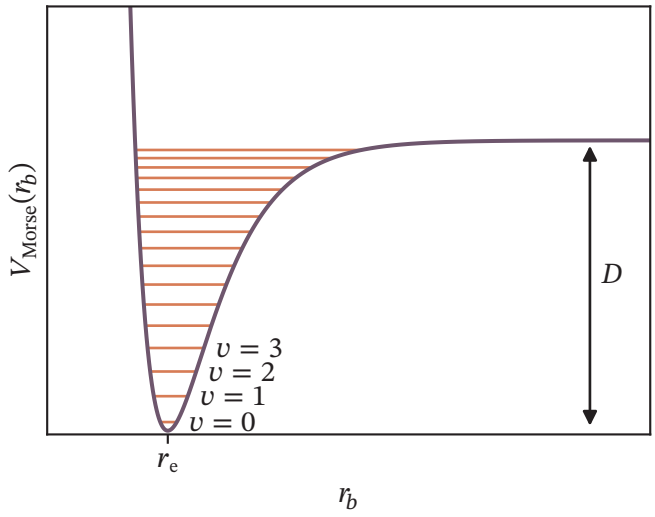

Figure 2.1: Plot of an exemplary Morse potential in accordance with [49]. The dissociation energy D is indicated, and typically given with respect to the lowest vibration level. The horizontal lines indicate vibrational levels, and the first four are labeled with their vibrational quantum number υ.

approximation is the Morse potential given by [46]

$$V(r_b) = D\left[1 - \exp(-a(r_b - r_e))\right]^2 \quad . \tag{2.6}$$

The constant a, the equilibrium distance r_e and the dissociation energy D are all specific to the molecule. Values are given in Morse's paper [49] and a plot of an exemplary Morse potential is shown in figure 2.1. The Schrödinger equation can be solved analytically and gives the vibrational levels as [42]

$$G(\upsilon) = \omega_e\left(\upsilon + \frac{1}{2}\right) - \omega_e\chi_e\left(\upsilon + \frac{1}{2}\right)^2 \quad . \tag{2.7}$$

In equation (2.7) the vibrational quantum number is denoted by $\upsilon = 0, 1, 2 \ldots$, ω_e is the vibrational frequency in equilibrium and χ_e is a constant. Within the Morse approximation,

$$\omega_e = \frac{a}{2\pi}\sqrt{\frac{2D}{m_\mu}} \quad , \tag{2.8a}$$

$$\chi_e = \frac{h^2}{4D} \quad , \tag{2.8b}$$

holds [49]. Here, $m_\mu = m_1 m_2/(m_1 + m_2)$ is the reduced mass.

Essentially equation (2.7) describes a harmonic oscillator with an additional quadratic contribution, leading to a smaller spacing between levels the higher the vibrational quantum number. Horizontal lines indicate these levels in figure 2.1. The higher order contributions are typically orders of magnitude smaller [50].

2.1.2 Rotational structure

To treat the rotational structure of a molecule, a combination of a classical and a quantum mechanical approach is used. The simplest model would be the "rigid rotator", as shown in figure 2.2a. The masses m_1 and m_2 of the atoms are considered point-like, and the bond is modeled by a rigid rod. These approximations are justified, as the distance between both atoms only alters marginally in reality, and the extent of the nuclei is small. There is no potential energy involved, as we only consider rotation. The introduction of the reduced mass m_μ allows simplifying the problem further, as the Schrödinger equation then only depends on the center–of–mass coordinate r_c, and can be written as [42]

$$\left[\frac{\hbar^2}{2m_\mu}\Delta + E\right]\psi(r_c) = 0 \quad . \tag{2.9}$$

The eigenenergies are

$$E(N^+) = \frac{\hbar^2}{2\Theta}N^+\left(N^+ + 1\right) \quad , \tag{2.10a}$$

$$F(N^+) = \frac{E(N^+)}{hc} \equiv B_\mathrm{e}N^+\left(N^+ + 1\right) \quad , \quad N^+ = 0, 1, 2, \ldots \quad , \tag{2.10b}$$

where N^+ is the rotational quantum number of the core, and $\Theta = m_\mu r_c^2$ is the classical momentum of inertia. Here, N^+ is also the total angular momentum. B_e is the rotational constant in equilibrium. The classical angular momentum $P = \Theta\omega$ yields the quantized eigenfrequencies, $\omega = \hbar\sqrt{N^+(N^+ + 1)}/\Theta$.

By introducing a massless spring with constant k between the atoms, we are able to refine the model further and obtain the non-rigid rotator as visualized in figure 2.2b. The spring's force $F_\mathrm{S} = k(r - r_\mathrm{e})$ and the centrifugal force $F_\mathrm{C} = m_\mu\omega r$ are counteracting each other. For small elongations, the elongation is the same as the equilibrium distance, $r \approx r_\mathrm{e}$. An expansion in second order pays respect to these contributions. The rotational energy is [43]

$$F(N^+) = B_\mathrm{e}N^+\left(N^+ + 1\right) - D_\mathrm{e}\left(N^+\right)^2\left(N^+ + 1\right)^2 \quad , \tag{2.11}$$

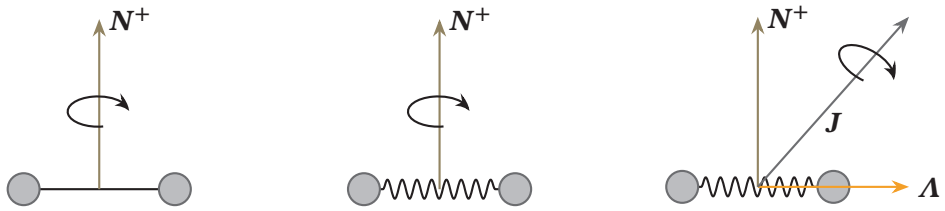

a) Rigid rotator **b)** Non-rigid rotator **c)** Vibrating symmetric top

Figure 2.2: Sketches of the rigid rotator, the non-rigid-rotator and the vibrating symmetric top, as an explanation for the rotational spectrum of diatomic molecules. The description becomes more precise from left to right. After [42].

where D_e is the centrifugal distortion constant. Both rotators treat the rotation independently of vibration. However, while the molecule vibrates, the moment of inertia changes slightly [43]. The so-called vibrating rotor accounts for this, and introduces additional constants α_e and β_e, such that the contributions from rotation and dissociation can be written with the vibrational quantum number v like

$$B_v = B_e - \alpha_e\left(v + \frac{1}{2}\right) + \ldots \quad , \tag{2.12a}$$

$$D_v = D_e - \beta_e\left(v + \frac{1}{2}\right) + \ldots \quad . \tag{2.12b}$$

We still have to take care of the moment of inertia along the internuclear axis. It is not zero due to the movement of the electrons, yet small, due to their mass [42]. Up to this point all models introduced neglected the electrons completely. The vibrating symmetric top accounts for this. Here, we neglect the individual movements of the electrons, which means the electron cloud is considered to be rigid. The total angular momentum is not perpendicular to the internuclear axis anymore. As $\boldsymbol{N}^+$ shall denote the angular momentum perpendicular to the internuclear axis, the total angular momentum is assigned the letter $\boldsymbol{J}$. The momentum along the internuclear axis is the electronic angular momentum and called $\boldsymbol{\Lambda}$, and $\boldsymbol{J}$ is the result of the coupling of $\boldsymbol{N}^+$ and $\boldsymbol{\Lambda}$ [42, 43]. The whole system rotates around $\boldsymbol{J}$. A sketch can be found in figure 2.2c. Depending on the sense of rotation of the electrons, the sketch in figure 2.2c "flips" along $\boldsymbol{N}^+$. Thus, for each value J there are two modes of motion. Important properties are:

$$|\boldsymbol{J}| = \hbar\sqrt{J(J+1)} \quad J = \Lambda, \Lambda+1, \Lambda+2, \ldots \tag{2.13a}$$

$$|\boldsymbol{\Lambda}| = \hbar\Lambda \tag{2.13b}$$

The rotational energy of the vibrating symmetric top is [42]:

$$F(J) = B_\upsilon J(J+1) - D_\upsilon J^2 (J+1)^2 + (A - B_\upsilon)\Lambda^2 \tag{2.14}$$

Equation (2.12a) and equation (2.12b) give B_υ and D_υ in equation (2.14). The constant A is defined the same way as B, see equation (2.10b), thus $A = \hbar^2/2\Theta_e hc$, though the moment of inertia of the electrons has to be used. The constant A is the spin-orbit constant. As can be seen, the last term only offsets the overall rotational energy, since Λ is constant for a given electronic state [42]. By evaluating the electric dipole moment we obtain the selection rules for a rotational transition within the same electronic state of a heteronuclear molecule as [42]

$$\Lambda = 0, \Delta J = \pm 1 \quad \text{or} \quad \Lambda \neq 0, \Delta J = 0, \pm 1 \quad . \tag{2.15}$$

As will be seen later, the transitions chosen in this work are such, that $\upsilon = 0$, making equation (2.14) even simpler.

Coming back to equation (2.5b), the energy of a diatomic molecular state is approximately given by

$$\begin{aligned} T &= T_\mathrm{e} + G + F \\ &= T_\mathrm{e} + \omega_\mathrm{e}\left(\upsilon + \frac{1}{2}\right) - \omega_\mathrm{e}\chi_\mathrm{e}\left(\upsilon + \frac{1}{2}\right)^2 + B_\upsilon J(J+1) - D_\upsilon J^2 (J+1)^2 + (A - B_\upsilon)\Lambda^2 \,. \end{aligned} \tag{2.16}$$

Databases such as [50] serve as a valuable reference for the necessary constants.

2.1.3 Hund's cases

The quantum numbers introduced in subsection 2.1.2 serve as a good starting point, though they do not describe the diatomic molecule in full detail. Instead, the different angular momenta couple in different ways. The angular momenta considered are the total angular momentum $\boldsymbol{J}$, the rotational angular momentum $\boldsymbol{N}$, the rotational angular momentum of the ionic core $\boldsymbol{N}^+$, the total spin $\boldsymbol{S}$ and the orbital angular momentum $\boldsymbol{L}$. The projection onto the internuclear axis of $\boldsymbol{L}$ is called Λ, the projection of $\boldsymbol{S}$ is called Σ and the projection of $\boldsymbol{L} + \boldsymbol{S}$ is called Ω. The so-called Hund's cases (a) to (e) describe different extreme cases of coupling [43]. Not all the introduced momenta are defined in each case. Hund's cases are assigned to each electronic molecular state in literature and were introduced by Friedrich Hund [42]. However, an assignment serves more like a starting point, such that the phrase "state

XY behaves mostly like a Hund's case *(z)*" holds true. Figure 2.3 gives an overview over all five Hund's cases. Depending on the case, some quantum numbers may be considered "good", whereas others are "bad" for the basis. Good quantum numbers form a basis of a state. This whole subsection is based on [42, 43]. Hund's case (a), (b) and (d) are of relevance for this thesis, whereas (c) and (e) are only shown for completeness.

Hund's case (a)

The core property of a Hund's case (a) is strong spin-orbit coupling, i. e. spin $\boldsymbol{S}$ couples strongly to $\boldsymbol{L}$. The spin-orbit constant A is much larger than the rotational constant B. A sketch is given in figure 2.3a. The rotational Hamiltonian and energy are given by

$$\frac{H_{\mathrm{rot}}}{hc} = B\,(\boldsymbol{N}^+)^2 = B\,(\boldsymbol{J}-\boldsymbol{L}-\boldsymbol{S})^2 \quad , \quad F = BJ(J+1) \quad . \tag{2.17}$$

The sense of precession of $\boldsymbol{L}$ and $\boldsymbol{S}$ has two cases, we associate $\pm\Lambda$ and $\pm\Omega$ with each J. We speak of Λ–doubling in the first case, and of Ω–doubling in the second. In this picture they are degenerate, though the degeneracy may be lifted due to the interaction of $\boldsymbol{N}^+$ and $\boldsymbol{L}$. A Hund's case (a) is a good case for low J.

Hund's case (b)

In a Hund's case (b) there is no spin-orbit coupling (or only very weak coupling) of $\boldsymbol{S}$ to the internuclear axis and $\Lambda \approx 0$. Figure 2.3b shows a vector representation. The newly introduced rotational angular momentum $\boldsymbol{N}$ is formed by $\boldsymbol{L}$ and $\boldsymbol{N}^+$. It is well-defined, since the precession of its summands is fast. Vector $\boldsymbol{N}$ couples with $\boldsymbol{S}$ to form $\boldsymbol{J}$. The rotational Hamiltonian is $H_{\mathrm{rot}} = B(N^+)^2 = B(N-L)^2$. For the specific case of $S = 1/2$ the spin-rotation interaction $\gamma \cdot NS$, where γ is a constant, has to be added to the rotational energy. The treatment is more complicated for $S > 1$.

Hund's case (c)

In a Hund's case (c), see figure 2.3c, the coupling between $\boldsymbol{L}$ and $\boldsymbol{S}$ is stronger than any coupling to the internuclear axis. Neither Λ nor Σ are defined. The projection Ω is defined and causes Ω–doubling, if $\Omega \neq 0$. $\boldsymbol{S}$ and $\boldsymbol{L}$ form a resultant vector named $\boldsymbol{J}_{\mathrm{a}}$, which couples with $\boldsymbol{N}^+$ to form $\boldsymbol{J}$. The rotational levels have energies as case (a), thus $F(J) = BJ(J+1)$.

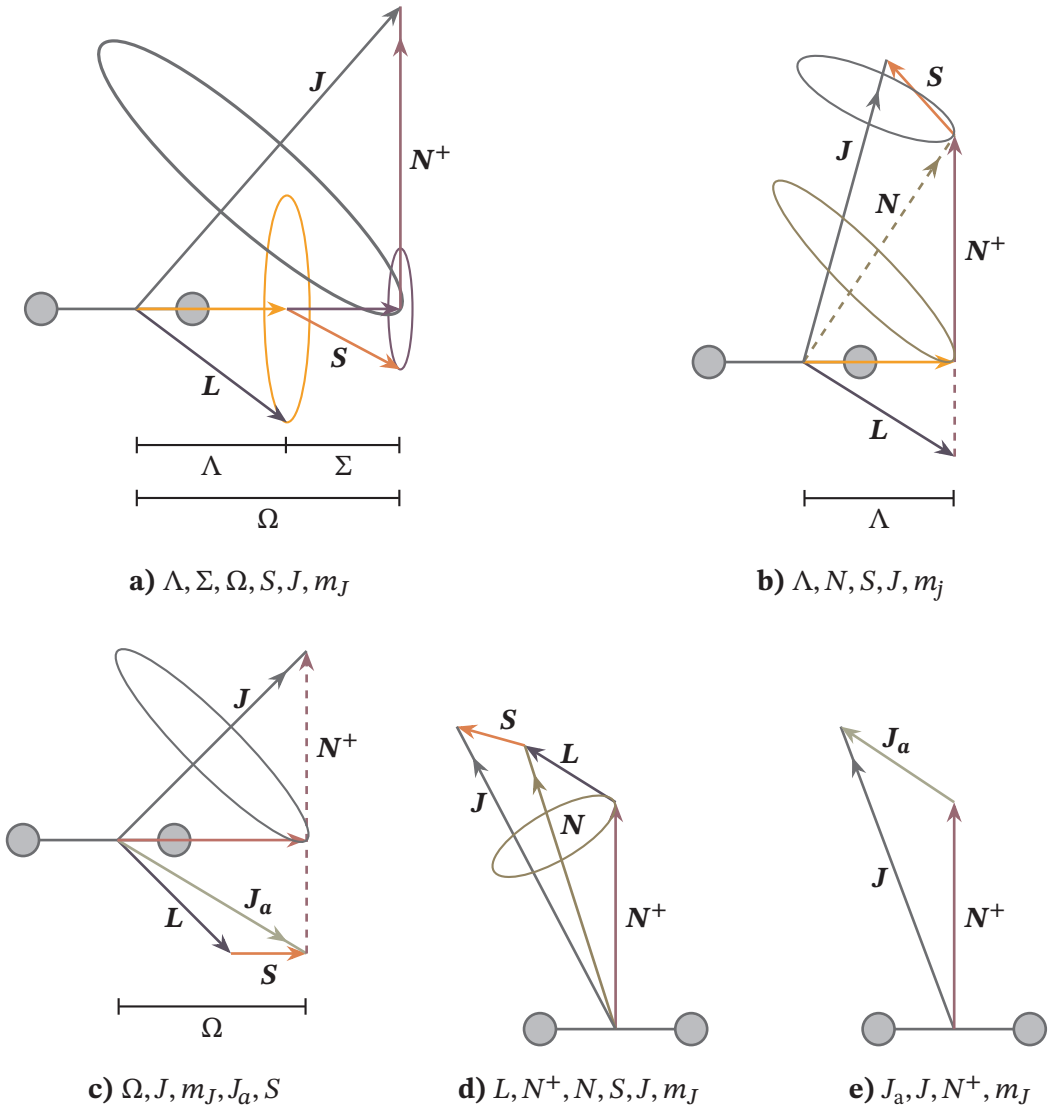

a) $\Lambda, \Sigma, \Omega, S, J, m_J$ **b)** Λ, N, S, J, m_j

c) Ω, J, m_J, J_a, S **d)** L, N^+, N, S, J, m_J **e)** J_a, J, N^+, m_J

Figure 2.3: Hund's cases (a) to (e). Graphics are following the one's found in [42, 43]. The caption gives "good" quantum numbers, which form a basis for each case. m_J is the magnetic quantum number, and the projection of $\boldsymbol{J}$.

Hund's case (d)

A Hund's case (d) is shown in figure 2.3d. The orbital angular momentum $\boldsymbol{L}$ couples only weakly to the internuclear axis, yet strongly to $\boldsymbol{N}^+$, i. e. the axis of rotation. Thus, $\boldsymbol{N}^+$ is well-defined here, and has values

$$|\boldsymbol{N}^+| = \hbar\sqrt{N^+(N^+ + 1)} \quad , \quad N = N^+ + L, N^+ + L - 1, \dots, N^+ - L \quad . \tag{2.18}$$

The rotational energy is approximately given by

$$F(N^+) = B_v N^+(N^+ + 1) \quad . \tag{2.19}$$

For each rotational level there are $2L + 1$ components.

Hund's case (e)

A Hund's case (e) is characterized by a strong coupling of $\boldsymbol{L}$ and $\boldsymbol{S}$, while there is only weak interaction with the internuclear axis. It is shown in figure 2.3e. An intermediate vector $\boldsymbol{J}_\mathrm{a}$ formed by $\boldsymbol{L}$ and $\boldsymbol{S}$ couples strongly to $\boldsymbol{N}^+$ to form $\boldsymbol{J}$.

2.1.4 Parity

Parity describes how a wavefunction $\psi(\boldsymbol{r})$ changes sign when mirrored at the origin, i. e. the inversion symmetry, and is important for transition probabilities. The wavefunction itself has to be an eigenfunction of the parity operator, i. e. it only describes a well-defined state in a molecule. In general, the parity must change for a transition to be allowed in first order [42]. If $\mathcal{P}$ is the parity operator, then [43]

$$\mathcal{P}\psi(\boldsymbol{r}) = \psi(-\boldsymbol{r}) = \pm\psi(\boldsymbol{r}) \quad . \tag{2.20}$$

We see, that the wavefunction either flips sign or not. If the function flips the sign it is called negative parity, otherwise positive parity. For molecules, the total wavefunction depends approximately on the product of the electronic wavefunction, the vibrational wavefunction and the rotational wavefunction [42, 43, 51]. The vibrational function does not change under reflection, as it only depends on the internuclear distance for diatomic molecules, i. e. $\mathcal{P}\,|v\rangle = +\,|v\rangle$ [42]. Additionally, we have to take the Hund's case of a particular state into account, i. e. parity has to be treated differently

depending on the Hund's case. For this thesis the parity rules of Hund's case (a) and (b) are of interest. For a Hund's case (a) we can write

$$\mathcal{P}\,|\Lambda,\Sigma,\Omega,S,J,m_J\rangle = (-1)^{J-S+\xi}\left|-\Lambda^{\xi},-\Sigma,-\Omega,S,J,m_J\right\rangle \quad , \tag{2.21}$$

and for a Hund's case (b)

$$\mathcal{P}\,|\Lambda,N,S,J,m_J\rangle = (-1)^{N+\xi}\left|-\Lambda^{\xi},N,S,J,m_j\right\rangle \tag{2.22}$$

holds [43]. Note that ξ accounts for the special case of Σ–states, and ξ is even for Σ^+ and odd for Σ^-–states [43]. The two eigenfunctions of the parity operator $\mathcal{P}$ in a Hund's case (a) are

$$\psi^{(a)}_{\text{positive}} = \frac{1}{\sqrt{2}}\left[\left|\Lambda^{\xi},\Sigma,\Omega,S,J,m_J\right\rangle + (-1)^{J-S+\xi}\left|-\Lambda^{\xi},-\Sigma,-\Omega,S,J,m_J\right\rangle\right] \quad ,$$
$$\psi^{(a)}_{\text{negative}} = \frac{1}{\sqrt{2}}\left[\left|\Lambda^{\xi},\Sigma,\Omega,S,J,m_J\right\rangle - (-1)^{J-S+\xi}\left|-\Lambda^{\xi},-\Sigma,-\Omega,S,J,m_J\right\rangle\right] \quad ,$$

and the degeneracy of these two functions is lifted by Λ–doubling [43].

The parity $\pm$ can be assigned to each (rotational) state of a molecule. However, it is also quite common to use a different naming scheme, to make the assignment independent of the coupling case and prevent the sign from alternating between different levels of J. The e– and f–labeling scheme is introduced in [52] as

$$\mathcal{P}\psi = +(-1)^{J+\zeta} \Rightarrow \text{e} \quad , \tag{2.24a}$$
$$\mathcal{P}\psi = -(-1)^{J+\zeta} \Rightarrow \text{f} \quad . \tag{2.24b}$$

If the diatomic molecule has an odd number of electrons $\zeta = 1/2$, and if the molecule has an even number of electrons $\zeta = 0$. The first case applies to NO.

As already stated, parity must change for a transition induced by radiation. Within the e– and f–labeling scheme this selection rule becomes [52]

$$\text{e} \leftrightarrow \text{f, if } \Delta J = 0 \qquad \text{e} \leftrightarrow \text{e, or f} \leftrightarrow \text{f, if } \Delta J = \pm 1 \quad . \tag{2.25}$$

An overview of all necessary selection rules for a molecular transition is given in subsection 2.1.7.

2.1.5 Labeling an electronic molecular state

The labeling of an electronic molecular state has a strong historic component. The old and frequently used way is

$$(\mathrm{A, B, C, \ldots})^{2S+1}\,\Lambda^{\pm}_{\Omega} \quad , \tag{2.26}$$

and has its origin in physical chemistry [45, 53].

The first letter follows the alphabet, and is assigned in order of the state's discovery. "X" always denotes a ground state. If the multiplicity $2S + 1$ changes for an excited state, when compared to the ground state, we use a lower-case letter. If a state is discovered later, an apostrophe is added. We only add the total electronic angular momentum Ω, if it is well-defined in the state's Hund's case.

Another way of naming a molecular state considers its electronic configuration. Here, we also have to take care if the literature already refers to a Rydberg state or not. As the principal quantum number is sometimes somewhat arbitrarily assigned, it is not always clear what might be considered a Rydberg state. Yet it is common to use a lower–case letter when referring to properties of a Rydberg state [3, 54]. For naming the quantum numbers of the formed complex, the principal quantum number n and the angular momentum l are used [54]. The molecular orbital λ is assigned as well [54], resulting in $nl\lambda$. For l the respective letter is used, i. e. $l = 0 \rightarrow s$, $l = 1 \rightarrow p$, $l = 2 \rightarrow d$, $l = 3 \rightarrow f$, $l = 4 \rightarrow g$ ..., and for λ the Greek equivalents are used, i. e. $\lambda = 0 \rightarrow \sigma$, $\lambda = 1 \rightarrow \pi$ and so on. Going back and forth between both naming schemes can be confusing. For example, in NO the H $^2\Sigma^+$ is the $3d\sigma$–state, the H' $^2\Pi$ is the $3d\pi$–state, yet the A $^2\Sigma^+$ is the $3s\sigma$–state [18, 54].

Sometimes the A $^2\Sigma^+$–state is already considered a Rydberg state [54], however, within the scope of this thesis a Rydberg state is a state behaving hydrogenic.

2.1.6 Labeling a molecular transition

A molecular transition has an electronic, vibrational and rotational component. In general, the initial state is on the right, whereas the final state is on the left of the arrow, i. e. $B \leftarrow A$. The vibrational quantum number can be given in parentheses [55], however, if it doesn't change, it is usually not given. Quantum numbers assigned to the initial state have an apostrophe, whereas the final one's have not. For example, in a level scheme the highest state lacks any apostrophes, yet the lowest one has the

most. To distinguish rotational branches we use the following convention [42]:

$$\Delta J = J - J' = -1\text{: P branch} \quad \Delta J = 0\text{: Q branch} \quad \Delta J = 1\text{: R branch} \tag{2.27a}$$

$$\Delta N = N - N' = -1\text{: p branch} \quad \Delta N = 0\text{: q branch} \quad \Delta N = 1\text{: r branch} \tag{2.27b}$$

For the application of equation (2.27b), N must be a good quantum number. In parentheses, we give the total angular momentum of the initial state, and add the index of the F_i–labeling scheme. The F_i–labeling scheme origins from Hund's case (a) and (b). We will see, that the ground state X $^2\Pi$ of NO is a Hund's case (a), where $\Lambda = 1$ and $S = 1/2$. As $\Omega = \Lambda \pm \Sigma$, we have spin-orbit coupling and as such to distinct electronic states with $\Omega = 1/2$ and $\Omega = 3/2$. The $\Omega = 1/2$–state is lower in energy, and labeled F_1, whereas the $\Omega = 3/2$–state is higher in energy and labeled as F_2. The first excited state of NO we use is the A $^2\Sigma^+$ and a Hund's case (b). In general a Hund's case (b) may have Λ–doubling, due to the sense of precession of L. For the specific case of $S = 1/2$ there are two values for J possible, where $J = N + 1/2$ is called the $F_1(J)$ series, and $J = N - 1/2$ is the $F_2(J)$ series. This splitting is called spin-rotation splitting. According to Herzberg [42], for a $^2\Sigma$–state (see subsection 2.1.5 for what this means) we have

$$F_1(N) = B_v N(N+1) + \frac{1}{2}\gamma N \quad , \tag{2.28a}$$

$$F_2(N) = B_v N(N+1) - \frac{1}{2}\gamma (N+1) \quad . \tag{2.28b}$$

For example, a rotational branch labeled as $P_{12}(5.5)$ means $\Delta J = -1$, $J' = 5.5$, index i of F_i' is 2 and of F_i is 1. As soon as we look at the excitation scheme, this becomes clearer.

2.1.7 Selection rules

Selection rules are the result of evaluating the electric dipole operator between transitions, i. e. evaluating the transition moment $\langle\psi_f|\boldsymbol{dE}|\psi_i\rangle$, if $\langle\psi_f|$ is the final state, $|\psi_i\rangle$ is the initial one, $\boldsymbol{E}$ is the electric field and $\boldsymbol{d}$ is the dipole operator [51]. In general the wavefunction, i. e. the good quantum numbers, depends on a particular Hund's case. The selection rules for a heteronuclear molecule are summarized in table 2.1.

Table 2.1: Different selection rules for a heteronuclear molecule as reproduced from [16], which in turn is based on [42].

Description	Rule	Application
J	$\Delta J = 0, \pm 1, J' \nleftrightarrow J$	general
Parity $\pm$	$+ \leftrightarrow -$	general
Parity e & f	e $\leftrightarrow$ f ; $\Delta J = 0$	general
	e $\leftrightarrow$ e; f $\leftrightarrow$ f; $\Delta J = \pm 1$	
Λ	$\Delta\Lambda = \pm 1, 0$	Hund's case (a) and (b)
$\Sigma^{\pm}$–states	$\Sigma^+ \nleftrightarrow \Sigma^-$	Hund's case (a) and (b)
S	$\Delta S = 0$	Hund's case (a) and (b)
Σ	$\Delta\Sigma = 0$	Hund's case (a)
Ω	$\Delta\Omega = 0, \pm 1,$	Hund's case (a)
	$\Delta\Omega = 0 \rightarrow \Delta J \neq 0$	
N	$\Delta N = 0, \pm 1,$	Hund's case (b)
	but for $\Sigma \leftarrow \Sigma$: $\Delta N = 0$	
L	$\Delta L = 0, \pm 1$	Hund's case (d)
N^+	$\Delta N^+ = 0$	Hund's case (d)

2.2 Nitric oxide

NO is radical with a single free valence electron having a total spin of $S = 1/2$ [54]. Its most abundant isotope is $^{14}N^{16}O$ (> 99 %) [56], and the only one considered in this work. At room temperature nitric oxide is in the gas phase, color– and odorless, though it immediately reacts to nitrogen dioxide (NO_2), if exposed to oxygen [57]. Both NO and NO_2 are toxic [58]. For NO, most molecules have no vibration $v = 0$ at room temperature [42]. As such, we only excite with $v = 0$. In figure 2.4 a molecular orbital diagram of NO is drawn.

To excite NO to a Rydberg state $n(N^+)$, we use a three-photon excitation scheme employing only cw lasers. In literature, NO is typically excited to a Rydberg state by

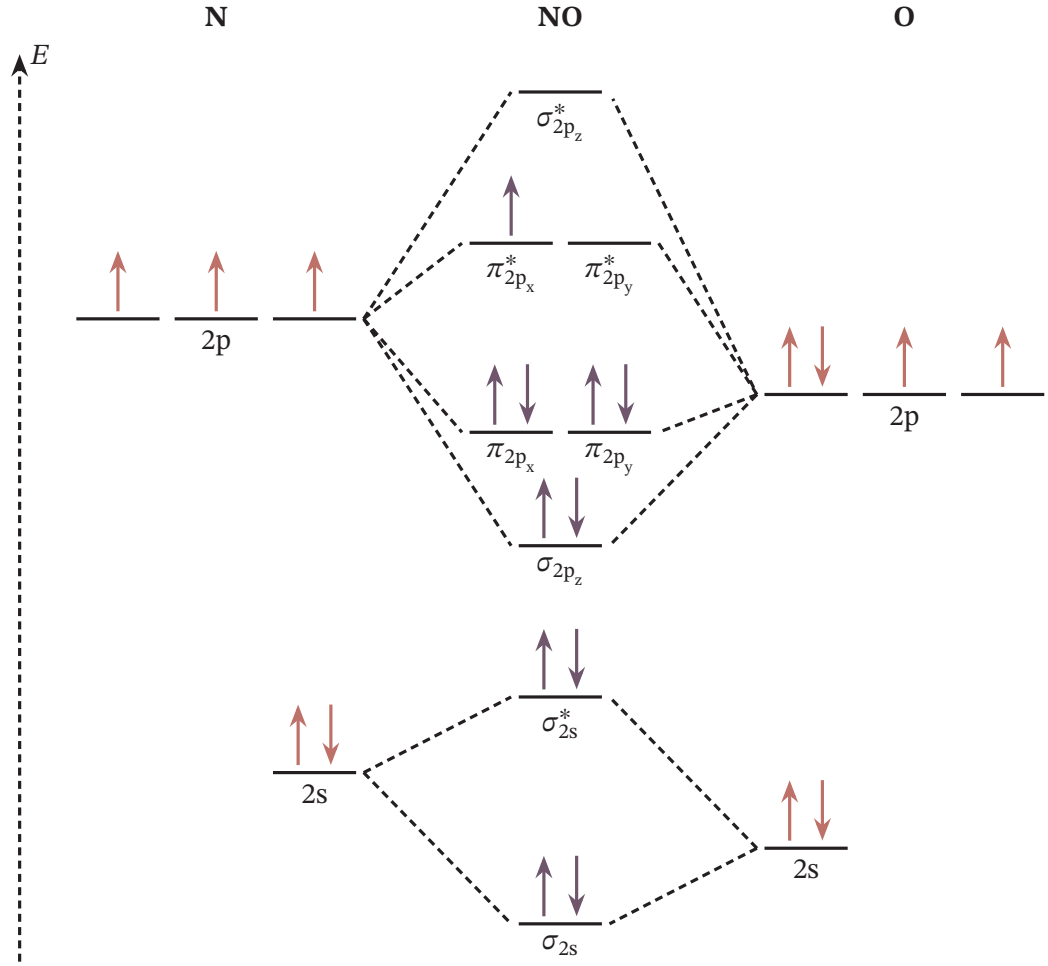

Figure 2.4: Molecular orbital diagram of NO in its ground state for all valence electrons. After [59].

a two-photon excitation scheme, e. g. [3, 4], and pulsed lasers systems are used. The wavelengths used in these experiments are 226 nm for the ground state transition $A\,^2\Sigma^+ \leftarrow X\,^2\Pi_{1/2}$, and 328 nm for $n(N^+) \leftarrow A\,^2\Sigma^+$. However, a cw system in the deep ultraviolet (UV) is challenging. While the ground state transition $A\,^2\Sigma^+ \leftarrow X\,^2\Pi$ is unavoidable, an additional step allows lifting the wavelengths into more accessible ranges. We chose the $H\,^2\Sigma^+$ as intermediate state, though the $H'\,^2\Pi$ is equally accessible. This decision was made based on a PhD thesis at the ETH Zurich [55]. At first, we'll look at the overall excitation scheme, afterward more details are given on the individual states.

2.2.1 Excitation scheme

This experiment employs a three-photon excitation scheme via the molecular transitions $A\,^2\Sigma^+ \leftarrow X\,^2\Pi_{3/2}$ at about 226 nm, $H\,^2\Sigma^+ \leftarrow A\,^2\Sigma^+$ at about 540 nm and $n(N^+) \leftarrow H\,^2\Sigma^+$ between 835 nm to 850 nm. Figure 2.5 shows the individual states involved in a level diagram. Additionally, some exemplary branches are marked. Ogi et al. [18] measured the $H\,^2\Sigma^+ \leftarrow A\,^2\Sigma^+$ transition. We use branches based on this work. With different excitation paths different Rydberg–N^+–series become accessible. As an example, a full excitation path can be written as

$$n(N^+) \leftarrow H\,^2\Sigma^+ \xleftarrow{R_{11}(5.5)} A\,^2\Sigma^+ \xleftarrow{P_{12}(6.5)} X\,^2\Pi_{3/2} \quad . \tag{2.29}$$

An excitation path has to stick to all introduced selection rules, e. g. parity tells which of the two Λ–doubled levels to choose in the $X\,^2\Pi_{3/2}$. Next we'll look at the individual states in more detail. The path given in equation (2.29) allows accessing the $N^+ = 4$ and $N^+ = 6$ series of NO Rydberg states. We will look at the accessibility of Rydberg states in section 2.3.

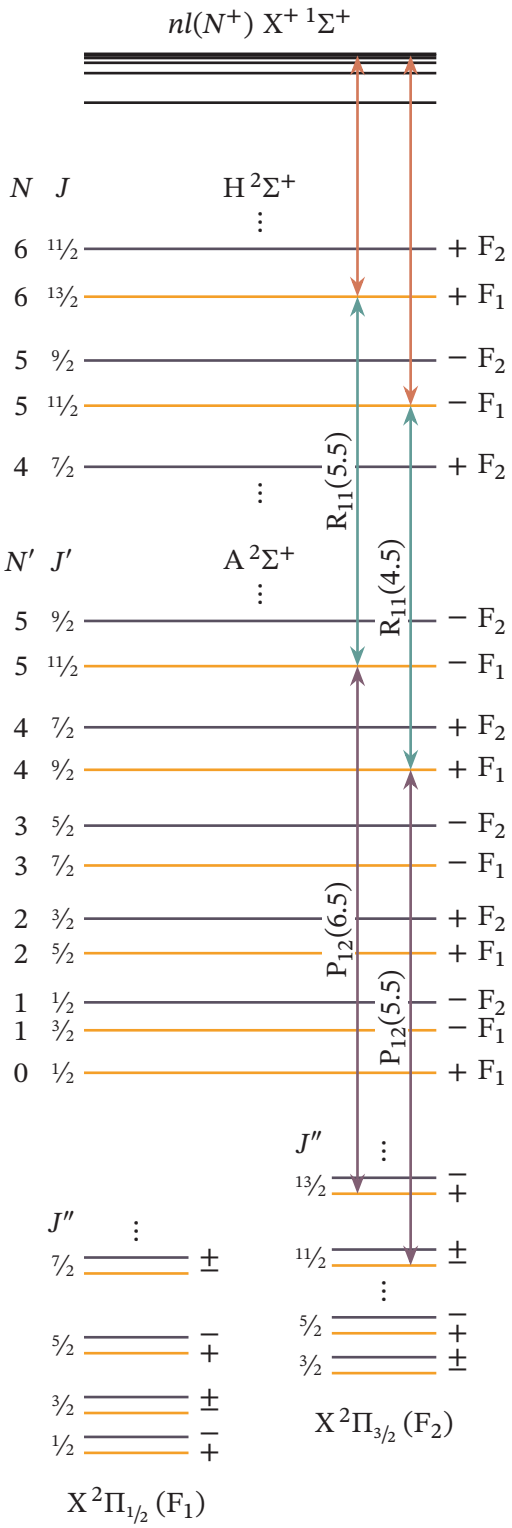

Figure 2.5: Detailed excitation of NO from the ground state $X\,^2\Pi$ to a Rydberg state $n(N^+)$ via two intermediate states $A\,^2\Sigma^+$ and $H\,^2\Sigma^+$. A + or − indicates parity. Alternatively, a level with a lighter color is of parity e, whereas a darker color denotes a parity f. To the Rydberg states no parity is assigned. The ground state is a Hund's case (a) for low angular momenta J, and a Hund's case (b) for higher angular momenta J, and can be labeled with the total angular momentum J''. As the ground state can be described with two Hund's cases, sometimes the rotational quantum number N'' is assigned to the levels as well [60]. The $A\,^2\Sigma^+$ and $H\,^2\Sigma^+$ are both a Hund's case (b) [55] and have quantum numbers N, N' and J, J'. We describe the Rydberg state $nl(N^+)$ $X^+\,^1\Sigma^+$ best by its principal quantum number n, its orbital angular momentum l and the rotational quantum number of the ionic core N^+. It is a Hund's case (d). Two excitation paths are shown as an example. Labeling of the branches is in accordance to subsection 2.1.6. The first transition is at 226 nm, the second transition at 540 nm and the final at around 830 nm to 850 nm. This level scheme is based on [18, 55, 60].

2.2.2 Ground state

The ground state of NO is a Π state labeled as $X\,^2\Pi$. For lower J the ground state behaves like a Hund's case (a), whereas for higher J it is more appropriate to use a Hund's case (b) for the description [4]. Since $\Lambda = 1$ and $S = 1/2$, we have in a Hund's case (a) two states due to spin-orbit coupling, $X\,^2\Pi_{1/2}$ and $X\,^2\Pi_{3/2}$ with $\Omega = 1/2$ and $\Omega = 3/2$ respectively. Both split by about $119.73(2)\,\mathrm{cm}^{-1}$ [61], and $X\,^2\Pi_{3/2}$ is energetically higher. Numerous resources on the molecular constants are available, an overview is given at [50]. We use the $X\,^2\Pi_{3/2}$ state for the excitation due to the available transitions in the $H\,^2\Sigma^+$ state [18]. This does not limit the available molecules, as the thermal energy at room temperature $T = 293\,\mathrm{K}$ is $E/hc = 3k_\mathrm{B}T/2hc \approx 305\,\mathrm{cm}^{-1}$, and thus well above the splitting. Additionally, the population of the rotational levels is given by the Boltzmann distribution

$$P(J) = hcB_\upsilon \frac{2J+1}{k_\mathrm{B}T} \exp\left[-hc\frac{B_\upsilon J(J+1)}{k_\mathrm{B}T}\right] \quad , \tag{2.30}$$

which is the probability $P(J)$ of finding a rotational state at total angular momentum J at temperature T according to Herzberg [62]. As $\upsilon = 0$ it follows $B_\upsilon = B_\mathrm{e} - \alpha/2$. For NO, the rotational constants of $X\,^2\Pi_{1/2}$ and $X\,^2\Pi_{3/2}$ only differ slightly [50, 63]. A plot is shown in figure 2.6. To the ground state no molecular orbital labeling is assigned [54]. The ground state shows Λ–doubling as indicated in figure 2.5 [4].

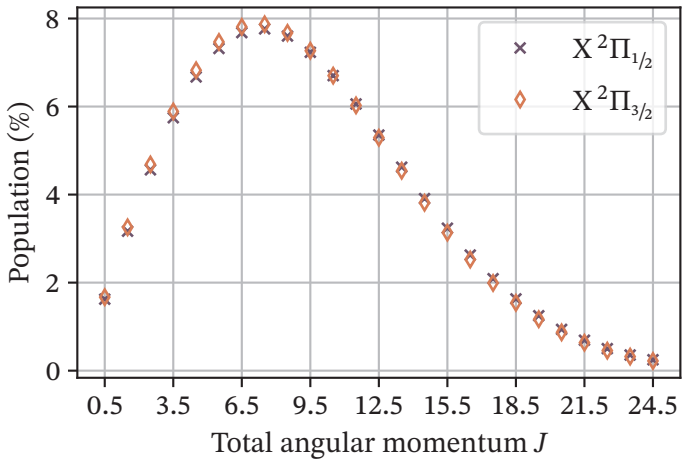

Figure 2.6: Population of the two ground states $X\,^2\Pi_{1/2}$ and $X\,^2\Pi_{3/2}$ of NO according to equation (2.30) at room temperature, $T = 293\,\mathrm{K}$. The constants used are $B_\mathrm{e} = 1.671\,95\,\mathrm{cm}^{-1}, \alpha = 0.0171\,\mathrm{cm}^{-1}$ for $X\,^2\Pi_{1/2}$, and $B_\mathrm{e} = 1.720\,16\,\mathrm{cm}^{-1}, \alpha = 0.0182\,\mathrm{cm}^{-1}$ for $X\,^2\Pi_{3/2}$. They are taken from [50]. The rotational state population differs only slightly between both states.

2.2.3 A state

The $A\,^2\Sigma^+$ state of NO is the first excitable state with same multiplicity after the ground state [50]. When using the molecular orbital notation $nl\lambda$, the $A\,^2\Sigma^+$ is a $3s\sigma$–state [54]. It has 94 % s–character and only 5 % d–character [47]. The $A\,^2\Sigma^+$–state can be described in a Hund's case (b). As explained in subsection 2.1.3 and figure 2.3b, a spin-rotation splitting due to $F_{1,2}(J) = N \pm 1/2$ arises, explaining two levels per J in figure 2.5.

The excitation from the X to A state is named the γ–band. Occasionally the vibrational quantum number of the upper v and lower state v' are added, i. e. this experiment uses the γ_{00} band [4, 64]. Similarly, excitations from X to the B or C state are performed on the β or δ–band respectively [64]. We resolved the hyperfine structure on selected transitions on the γ_{00}–band [16, 34].

2.2.4 H and H' state

The $H\,^2\Sigma^+$ and $H'\,^2\Pi$ are only about 12 cm^{-1} apart [65]. In molecular orbital notation, the $H\,^2\Sigma^+$ state is a $3d\sigma$ and the $H'\,^2\Pi$ is a $3d\pi$–state [18, 65, 66]. Both states have been investigated in literature [18, 55, 65–68], though it is somewhat hard to find literature on the $H\,^2\Sigma^+ \leftarrow A\,^2\Sigma^+$ transition. Ogi's paper [18] proved to be of great value for this project, as it was the only resource found which gives transition wavelengths for $H\,^2\Sigma^+ \leftarrow A\,^2\Sigma^+$. The transitions used in this thesis have the advantage, that there is significant population in the rotational levels of the ground state $X\,^2\Pi_{3/2}$ and a strong transition according to [18]. Nevertheless, Ogi also shows transitions to the $H'\,^2\Pi$–state which might be of interest in the future. Within this work the $H'\,^2\Pi$–state is not considered. Different branch choices allow accessing different Rydberg series. This will be seen in section 5.3.

The $H\,^2\Sigma^+$ is a Hund's case (b) [55]. It has 38 % s–character, yet 62 % d–character [47]. This makes it challenging when calculating the individual state properties. From an atomic point of view, an S to S transition would be forbidden. Due to the rich and complex structure of molecules, such simple statements are impossible.

2.3 Rydberg states in nitric oxide

2.3.1 Rydberg states in general

A molecular or atomic state is called a Rydberg state, if its principal quantum number n is particularly high. Of special interest are such states of particles, where only a single valence electron is involved. This makes their mathematical description similar to that of hydrogen [69, 70]. For hydrogen, the Rydberg formula reads

$$E_n = -hc\frac{R_\infty}{n^2}, \tag{2.31}$$

which allows calculating the energy E_n of a state by using the Planck constant h, the speed of light c and the Rydberg constant $R_\infty \approx 13.6\,\text{eV}$ [70]. For atomic or molecular species justifying the aforementioned condition, equation (2.31) has to be adjusted by introducing the quantum defect δ yielding

$$E_n = -hc\frac{R_\infty}{(n-\delta)^2} = -hc\frac{R_\infty}{\eta^2}, \tag{2.32}$$

where η is called effective principal quantum number. While for high-n-states of a Rydberg particle the similarities to hydrogenic wavefunctions are huge, especially for states of low n equation (2.32) accounts for the electron "seeing" a nucleus of different charge [70], i. e. different Coulomb potential.

By looking closer at equation (2.32) an important nature of Rydberg states becomes clear — the higher the principle quantum number n, the closer the states' energies are, making them almost degenerate. Additionally, they are easily ionized by collisions, since the outermost electron is then only loosely bound. This is highly important within in the scope of this thesis. This property yields a large dipole moment and makes Rydberg states very sensitive to electric fields. Consequently, the ionization threshold is the energy where ionization occurs, i. e. $n \to \infty$.

Other outstanding properties of Rydberg states are listed in table 2.2.

Table 2.2: Characteristic scaling of the properties of Rydberg states in dependence of the principal quantum number n. After [70, 71].

property	notation	scaling
orbital radius	$\langle r \rangle$	$\propto n^2$
binding energy	E_n	$\propto n^{-2}$
level spacing	$E_{n+1} - E_n$	$\propto n^{-3}$
radiative lifetime	τ_0	$\propto n^3$
polarizability	α	$\propto n^7$
dipole moment	$\boldsymbol{d}$	$\propto n^2$

2.3.2 Formal treatment

Since the main results of this thesis are achieved by exciting NO to a Rydberg state, we take a more formal look at the mathematical treatment of these states next. Our cooperation partners Stephen Hogan and Matthew Rayment give a great overview in [3], which in turn is based on several valuable resources [19, 72–74]. It has been discussed, among other things, within the scope of a Master's thesis at this project [75].

The idea is to use a combination out of a matrix–diagonalization approach, while adding corrections as calculated by multichannel quantum defect theory (MQDT). At first, we need the correct basis for the description of a Rydberg state. NO has a single free electron. Hence, we expect a hydrogen-like character for a Rydberg state. Predominantly a Rydberg state is a Hund's case (d) [19]. This is plausible, since in a Hund's case (d) properties of the electron ($\boldsymbol{L}$, $\boldsymbol{S}$) are decoupled from properties of the core ($\boldsymbol{N}^+$, vibration v). In Rydberg physics considering a single electron we typically use lower-case letters for the orbital angular momentum l, spin s and total angular momentum j [3]. Additionally, the principal quantum number n as in equation (2.32) completes the description. In an ideal Hund's case (d), we would have two independent basis sets, $|n, s = 1/2, l, j\rangle$ for the electron, and $|v^+, N^+, J^+\rangle$ for the ionic core [19].

However, several correctional terms arise, taking the finite probability of the electron being close to the core into account. As such, a Hund's case (d) is not sufficient for the full description. Quantum defects can be understood as phase shifts of the electron wave function, and can serve as characterization parameter [19]. In the case of NO, a Hund's case (b) is well-suited for these corrections [3, 72]. However, it might also be a Hund's case (a) for other molecules [19]. For being able to combine all descriptions a basis transformation is needed. We use the quantum number Λ in a Hund's case (b) for the quantum defects. However, since it is the goal to perform the overall

description in a Hund's case (d), we still add the orbital angular momentum l to the parameters to not lose track of what we are currently looking at. According to Greene and Jungen [72] for Rydberg states which converge to the $nl(N^+)$ $X^+\,{}^1\Sigma^+$–state of NO, we can write, while neglecting any spin interactions [3, 73]:

$$\left[H^{(N)}_{lN^+,l'N^{+\prime}}\right]^{(\mathrm{d})} = \sum_{\Lambda} A^{(Nl)}_{N^+\Lambda}\left[H^{\Lambda}_{ll'}\right]^{(\mathrm{b})} A^{(Nl')}_{N^{+\prime}\Lambda} \tag{2.33a}$$

$$A^{(Nl)}_{N^+\Lambda} = (-1)^{l+\Lambda-N^+}\begin{pmatrix} l & N & N^+ \\ -\Lambda & \Lambda & 0 \end{pmatrix}\sqrt{\frac{2\,(2N^+ + 1)}{1+\delta_{\Lambda,0}}} \tag{2.33b}$$

Equation (2.33b) gives the frame transformation from case (b) to (d), and (2.33a) shows its application. The Kronecker Delta is δ_{ij} and () is a Wigner–3j–symbol. Here and in the following a superscript like e. g. $X^{(\mathrm{b})}$ denotes, that variable X is considered in Hund's case (b) and so on. An additional superscript + is added, when the quantum number is referring to the ionic core. For example, l is the orbital angular momentum of the Rydberg electron, whereas $B^+_{v^+}$ is the rotational constant with vibrational quantum number v^+ of the ionic core.

In [3] the full Hamiltonian is constructed as was done by [19]. The field-free Hamiltonian of the Rydberg molecule will be called $H^{(\mathrm{d})}_0$. The Hamiltonian can be separated into three components, a diagonal one $H^{(\mathrm{d})}_{\mathrm{diag}}$, one which accounts for dipole interactions $H^{(\mathrm{d})}_{\mathrm{dip}}$ and another $H^{(\mathrm{d})}_{\mathrm{multi}}$, which accounts for any higher order interactions [3]:

$$H^{(\mathrm{d})}_0 = H^{(\mathrm{d})}_{\mathrm{diag}} + H^{(\mathrm{d})}_{\mathrm{dip}} + H^{(\mathrm{d})}_{\mathrm{multi}} \tag{2.34}$$

For $H^{(\mathrm{d})}_{\mathrm{diag}}$ and $H^{(\mathrm{d})}_{\mathrm{dip}}$ the basis is a Hund's case (d). $H^{(\mathrm{d})}_{\mathrm{multi}}$ considers the electron being close to the core, thus a Hund's case (b) must be used for the description and transformed with equation (2.33b). $H^{(\mathrm{d})}_{\mathrm{dip}}$ yields interactions between Hund's case (d) states with selection rules [3]

$$\Delta l = \pm 1 \quad \Delta N^+ = \pm 1 \quad \Delta N = 0 \quad \Delta M_N = 0 \quad , \tag{2.35}$$

as already introduced in table 2.1.

$H^{(\mathrm{d})}_{\mathrm{diag}}$ can be calculated the same way as the vibrating symmetric top, see subsection 2.1.2, while taking the additional offset by the Rydberg formula into account.

This is the case, as no perturbations of the eigenstates are present, thus

$$\langle n, l, N^+, N, M_N | H^{(\mathrm{d})}_{\mathrm{diag}} | n, l, N^+, N, M_N \rangle = hc\left[W_{v^+} + B^+_{v^+} N^+ (N^+ + 1) - D^+_{v^+} \left[N^+ (N^+ + 1)\right]^2 - \underbrace{\frac{R_{\mathrm{NO}}}{\left(n - \delta^{(\mathrm{d})}_{lN^+}\right)^2}}_{\left[\eta^{(\mathrm{d})}\right]^2} \right] \tag{2.36}$$

holds [3]. W_{v^+} is the absolute threshold energy. Equation (2.36) dominates the interaction and is the ideal description of a Hund's case (d) for Rydberg states. An exemplary plot of the equation is shown in figure 2.7.

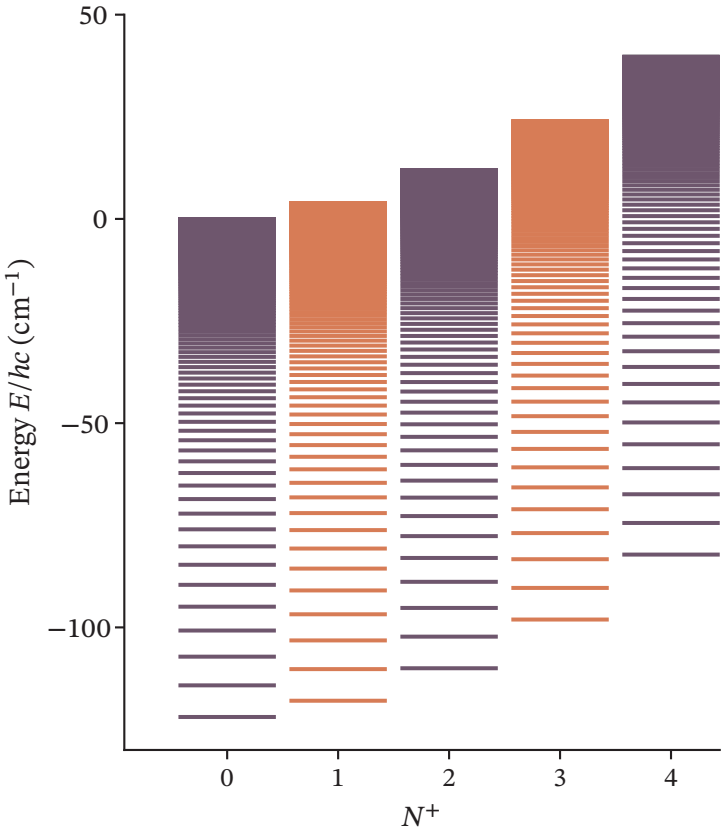

Figure 2.7: Plot of equation (2.36), with $B^+_{v^+} = 1.987\,825\,\mathrm{cm}^{-1}$, $D^+_{v^+} = 5.64 \cdot 10^{-6}\,\mathrm{cm}^{-1}$ and $R_{\mathrm{NO}} = 109\,735.31\,\mathrm{cm}^{-1}$ as given in [3] at different N^+. The quantum defect is not considered. In contrast to e. g. Rb, NO has several Rydberg series, which depend on the rotational quantum number N^+.

The $H^{(\mathrm{d})}_{\mathrm{dip}}$–Hamiltonian takes care of the static dipole interaction, i. e. it evaluates the dipole operator. According to [3] we have:

$$\left\langle n, l, N^+, N, M_N \middle| H^{(\mathrm{d})}_{\mathrm{dip}} \middle| n' l' N^{+\prime} N' M'_N \right\rangle = \frac{-e\mu_{\mathrm{NO}^+}}{4\pi\epsilon_0} \left\langle \eta^{(\mathrm{d})} l \middle| r^{-2} \middle| \eta^{(\mathrm{d})\prime} l' \right\rangle \left[f_{\mathrm{angular}} \left(n, l, N^+, N, M_N; n', l', N^{+\prime}, N', M'_N \right) \right] \tag{2.37}$$

We can separate the matrix element in equation (2.37) in a radial part and an angular part. The angular part is given by

$$\begin{aligned} f_{\mathrm{angular}} \left(n, l, N^+, N, M_N; n', l', N^{+\prime}, N', M'_N \right) = \\ (-1)^{l'+l+N'} \begin{Bmatrix} N' & N^+ & l \\ 1 & l' & N^{+\prime} \end{Bmatrix} \sqrt{(2N^+ + 1)(2N^{+\prime} + 1)} \begin{pmatrix} N^+ & 1 & N^{+\prime} \\ 0 & 0 & 0 \end{pmatrix} \\ \times \sqrt{(2l + 1)(2l' + 1)} \begin{pmatrix} l & 1 & l' \\ 0 & 0 & 0 \end{pmatrix} \delta_{N,N'} \delta_{M_N, M'_N} \quad , \end{aligned} \tag{2.38}$$

where {} is the Wigner–6j–symbol, e is the elementary charge, μ_{NO^+} is the electric dipole moment of the ionic core and ϵ_0 is the vacuum permittivity [3]. For the radial part an approximation by Gilbert and Child (they treat water (H_2O)) [76] is used in [3] and a direct result from MQDT given by

$$\left\langle \eta^{(\mathrm{d})} l \middle| r^{-2} \middle| \eta^{(\mathrm{d})\prime} l' \right\rangle = a_{\mathrm{NO}}^{-2} \left(\eta^{(\mathrm{d})} \eta^{(\mathrm{d})\prime} \right)^{-\frac{3}{2}} \left(\zeta_l + \zeta'_l + 1 \right)^{-1} \frac{\sin[\pi(\zeta_l - \zeta'_l)]}{\pi(\zeta_l - \zeta'_l)} \quad , \tag{2.39a}$$

$$\zeta_l \equiv l - \delta^{(\mathrm{d})}_{lN^+} \quad , \tag{2.39b}$$

where a_{NO} is the Bohr radius of NO. ζ_l is named the effective orbital angular momentum quantum number [75]

The $H^{(\mathrm{d})}_{\mathrm{multi}}$–Hamiltonian essentially takes additional corrections into account, and can be given best in a Hund's case (b) basis [62]. Here, N^+ is not of value anymore. The Born-Oppenheimer approximation, which holds in a case (d), cannot be used anymore, thus one sometimes refers to the Born-Oppenheimer region as soon as a Hund's case (b) is more appropriate [73]. The effect of the electron penetrating the core and leaving the region again is N^+–coupling [73]. To take this effect into account, the case (b) Hamiltonian is diagonal except for so-called sσ–dσ–mixing [73, 74]. sσ means $l = 0, \Lambda = 0$ and dσ means $l = 2, \Lambda = 0$. In general, one takes this mixing into account for low l, i. e. $l \leq 2$ [73]. The quantum defects are used as

Table 2.3: Quantum defects $\delta_{l\Lambda}^{(\mathrm{b})}$ of NO Rydberg states in Hund's case (b) reproduced from [74].

			Λ			
			σ	π	δ	φ
			0	1	2	3
l	s	0	0.210			
	p	1	0.7038	0.7410		
	d	2	0.05	−0.053	0.089	
	f	3	0.0182	0.0172	0.0128	0.0057

parameters [19]. The matrix element is [3]

$$\left\langle nlN^+NM_N|H_{\mathrm{multi}}^{(\mathrm{d})}|n'l'N^{+\prime}N'M_N'\right\rangle = -2hc\frac{R_{\mathrm{NO}}}{\eta^{3/2}\left(\eta^{3/2}\right)'}\left[\sum_{\Lambda}A_{N^+\Lambda}^{(Nl)}\left[H_{ll'}^{\Lambda}\right]^{(\mathrm{b})}A_{N^{+\prime}\Lambda}^{(Nl')}\right]\cdot\delta_{N,N'}\delta_{M_N,M_N'} \quad . \tag{2.40}$$

Finally, $[H_{ll'}^{\Lambda}]^{(\mathrm{b})}$ is given by [3, 73, 74]:

$$\left[H_{ll'}^{\Lambda}\right]^{(\mathrm{b})} = \begin{cases} \frac{1}{2}\left(\delta_{s\sigma}^{(\mathrm{b})}-\delta_{\mathrm{d}\sigma}^{(\mathrm{b})}\right)\sin\left(2\theta_{\mathrm{sd}}\right) & \text{if } l=0,2; l'=2,0; \Lambda=0 \\ \delta_{\mathrm{s}\sigma}^{(\mathrm{b})}\left[\cos\left(\theta_{\mathrm{sd}}\right)\right]^2+\delta_{\mathrm{d}\sigma}^{(\mathrm{b})}\left[\sin\left(\theta_{\mathrm{sd}}\right)\right]^2 & \text{if } l=l'=0; \Lambda=0 \\ \delta_{\mathrm{s}\sigma}^{(\mathrm{b})}\left[\sin\left(\theta_{\mathrm{sd}}\right)\right]^2+\delta_{\mathrm{d}\sigma}^{(\mathrm{b})}\left[\cos\left(\theta_{\mathrm{sd}}\right)\right]^2 & \text{if } l=l'=2; \Lambda=0 \\ \delta_{l\Lambda}^{(\mathrm{b})} & \text{else } (l=l') \end{cases} \tag{2.41}$$

Equation (2.41) is essentially a rotating matrix. The angle θ_{sd} is the so–called sσ–dσ mixing angle, and $\theta_{\mathrm{sd}} = -38.7°$ for NO [3, 77]. The necessary quantum defects $\delta_{l\Lambda}^{(\mathrm{b})}$ are given in [74] and listed in table 2.3. Since all quantum defects are less than 1, every line in l associated with any n and N^+ should appear after each other before n increases or decreases. The frame transformation for translating a $\delta^{(\mathrm{b})}$ to a $\delta^{(\mathrm{d})}$ is [3]

$$\delta_{l,(N^+,N)}^{(\mathrm{d})} = \sum_{\Lambda=0}^{l}\left(A_{N^+\Lambda}^{(Nl)}\right)^2\left[H_{ll'}^{\Lambda}\right]^{(\mathrm{b})} \quad . \tag{2.42}$$

The selection rules for the $H_{\mathrm{multi}}^{(\mathrm{d})}$–Hamiltonian are [3]

$$\Delta l = 0,\pm 2 \quad \Delta N^+ = \pm 2 \quad \Delta N = 0 \quad \Delta M_N = 0 \quad . \tag{2.43}$$

2.3.3 Accessible Rydberg states

In subsection 2.2.1 we took a look at the excitation scheme. Different rotational series N^+ of NO are accessible, which depend on the chosen branches of the first and second transition. Crucial is, that the H $^2\Sigma^+$–state has s– and d–character [47]. As the rotational quantum number N^+ does not change when exciting to a Rydberg state, it is reasonable to assign a "virtual" rotational quantum number to the H $^2\Sigma^+$–state, despite it being a bad quantum number for a Hund's case (b). For example, if $N' = 6$ for the H $^2\Sigma^+$–state, then $N^{+\prime} = 4, 6$, since $l' = 0, 2$. An exemplary excitation scheme is shown in figure 2.8. Here, the rotational quantum number N^+ is assigned to all states of the excitation scheme. For increasing principal quantum number n the wavefunction overlap with any given lower state decreases due to the increasing volume of the Rydberg state. This decreases the transition dipole moment, which yields lower signals in the measurement. This effect is the direct cause for the long lifetime of Rydberg states. Due to selection rules, refer to table 2.1, $\Delta l = \pm 1$. Thus, the l–character of Rydberg states should be either p or f, as $l' = 0, 2$. In principle $\Delta l = 0$ is allowed. However, if l does not change, something else has to, e. g. the magnetic moment has to couple. Such transitions are very weak and not expected. P–states dissociate way faster than f–states, meaning that the Rydberg states accessible to this experiment are mostly of f character [78].

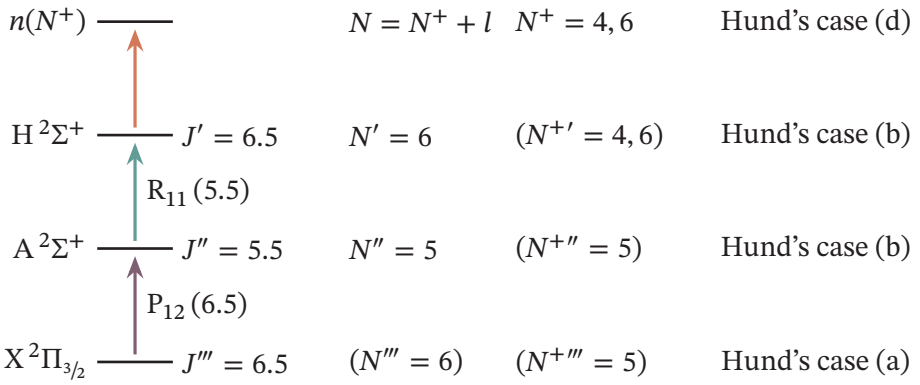

Figure 2.8: Exemplary excitation scheme to access the $N^+ = 4$ and $N^+ = 6$ series of NO. There is no change in N^+, when exciting to a Rydberg state. As the H $^2\Sigma^+$–state has both s– and d–character, a virtual N^+ of $N^+ = 4, 6$ can be assigned.

2.3.4 Notation of Rydberg states

For Rydberg states the principal quantum number n, and the rotational angular momentum N^+ of the ionic core can be assigned. Additionally, one may give the l–character by using the respective letters. The notation used in this work is

$$n(N^+) \quad \text{or} \quad nl(N^+) \quad \text{or} \quad nl(N^+)\ \mathrm{X}^+\,{}^1\Sigma^+ \quad . \tag{2.44}$$

The first variant is typically used, as both the nature of the ionic state $\mathrm{X}^+\,{}^1\Sigma^+$ and orbital angular momentum l are clear.

2.4 Constants for nitric oxide

An overview over all constants used in this work is given in the following table. We consider only transitions with $v = v' = 0$, i. e. $B_v = B_0 = B_e - \alpha_e \cdot (0 + 1/2)$.

	$\mathrm{X}\,{}^2\Pi_{3/2}$ [63] (cm^{-1})	$\mathrm{A}\,{}^2\Sigma^+$ [63] (cm^{-1})	$n(N^+)$ [3] (cm^{-1})
T_e	121.550 830 9[1]	43 906.191	
B_0, B_{0+}^+	1.696 069 1	1.995 586 0	1.987 825
D_0, D_{0+}^+	$5.4722 \cdot 10^{-6}$	$5.6563 \cdot 10^{-6}$	$5.64 \cdot 10^{-6}$
ω_e	1904.085	2374.372	
$\omega_e\chi_e$	14.0660	16.159	
γ		−0.002 68	
R_{NO}			109 735.31

[1] In [63] the spin–orbit constant A is 123.2469 cm^{-1}. Thus $T_e = A - B_0 = 121.550\,830\,9\ \mathrm{cm}^{-1}$.

3 Experimental setup and concepts

The experimental setup has four main components, the individual laser systems, the gas mixing unit (GMU), the frequency–stabilization setup and the glass cell. The glass cell is discussed in the next chapter. Any demand we have on the individual parts can be deduced from the goal of setting up a trace–gas sensor.

In terms of laser systems cw is an absolute necessity to keep the linewidth small. For the usability and compatibility to any optical component the mode profile has to be Gaussian. At the start of the project it wasn't assessable how good the literature values are. Typical pulsed experiments work at low temperatures (below 10 K) [4], and thus we will need other branches, and the possibility to optimize the excitation path. As such a rather large tunability of the laser systems was another demand. Another issue has been the lack of knowledge on the individual intensities required to drive any transition. Thus, we went for "as much power as possible". It turned out however, that already quite small intensities in the UV still yield sufficient measurement signals, as we will see. These demands left a titanium–sapphire laser (Ti:sa) system as the only option for the $A\,^2\Sigma^+ \leftarrow X\,^2\Pi_{3/2}$ transition, as we did not find any suitable diode–driven system which still allows for a large tunability in the UV.

The GMU has been set up by my colleague [16]. The demands were to either have stable pressure of either pure NO or diluted NO in a background gas. A stable pressure directly translates into a stable flow. When using a background gas, the GMU has to be capable of creating predefined and known concentrations of NO, such that values like the sensitivity of the sensor are calculable.

The necessity for a frequency–stabilization setup is a consequence of using cw systems. Due to their small linewidth, fluctuations in the environment may offset the laser system over time from the desired frequency. For this we compensate with a stabilization setup.

3.1 Laser systems and optical setup

To excite NO to a Rydberg state $n(N^+)$, three cw laser systems are used.

The first system is a frequency–quadrupled Ti:sa, which was bought from M Squared Lasers. It is used to drive the transition $A\,^2\Sigma^+ \leftarrow X\,^2\Pi_{3/2}$. Both the pump laser and the Ti:sa are sealed and can only be adjusted in terms of output power and wavelength. However, the incoupling of the Ti:sa is adjustable. With a maximum pump power of 18 W the Ti:sa yields approximately 4.5 W at a wavelength of 904 nm. The Ti:sa's wavelength is referred to as the fundamental wavelength of the UV system from now on.

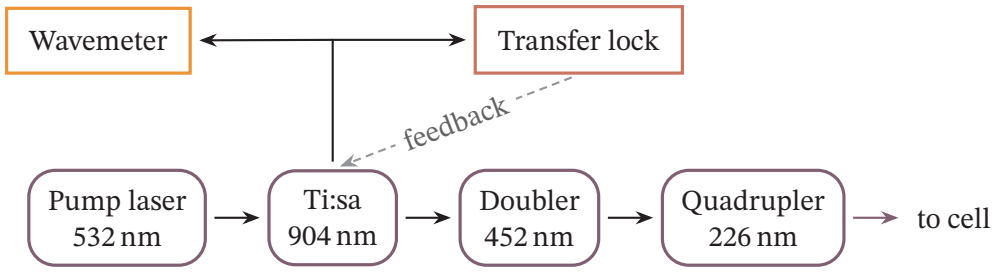

a) UV system for $A\,^2\Sigma^+ \leftarrow X\,^2\Pi_{3/2}$. The Ti:sa is pumped with 18 W and tuned between 904 nm and 908 nm and yields about 4.5 W. The doubler and quadrupler are bow-tie ring cavities. A BBO in the doubler yields an output power of about 1 W, whereas the quadrupler uses an LBO and yields typically at least 10 mW. The system was manufactured by M Squared Lasers.

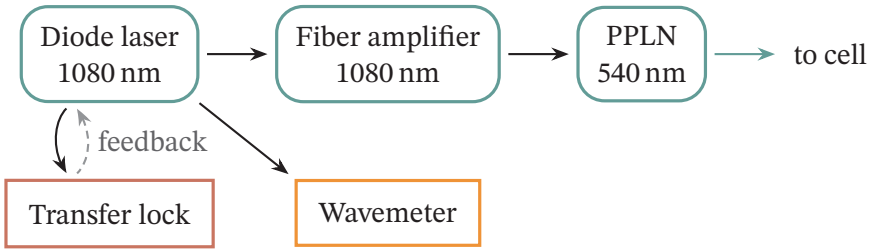

b) Green system for $H\,^2\Sigma^+ \leftarrow A\,^2\Sigma^+$. The diode laser is a Toptica DLPro, which is coupled into and amplified by a fiber amplifier by KEOPSYS, which yields 10 W maximum power. The light is frequency-doubled by a single-pass PPLN by HCPhotonics to about 650 mW.

Figure 3.1: Diagrams of the laser systems used to excite NO to a Rydberg state $n(N^+)$. We sent all respective fundamental beams to a wavemeter (HighFinesse WS-6). All fundamental beams are additionally sent to our locking setup, see section 3.3, though the Rydberg–Ti:sa system cannot be locked. This figure is divided over two pages.

This light is then sent into a bow tie-ring cavity (“doubler”), which uses a β barium borate crystal (BBO) to frequency double the light to a wavelength of 452 nm. Output powers reached are larger than 1 W. This light is again frequency–doubled by a second bow-tie ring cavity (“quadrupler”), which uses a lithium triborate crystal (LBO) and yields about 10 mW of UV power at 226 nm. Both cavities have to be optimized regularly by the experimentalist. A sketch can be found in figure 3.1a. The fundamental beam is split and sent to a wavemeter as well as to our locking setup. The laser’s wavelength is specified to be less than 200 kHz in linewidth in the UV. The fundamental wavelength of the UV system can be scanned within a range of about 25 GHz. Though the mode of the UV system should be Gaussian, measurements of the UV–beam’s dimensions changed quite considerably over time. Most likely, this can be attributed to degradation on the involved crystal as well as the overall laser system. Still, $1/e^2$–waists are given in their appropriate sections, though they should be considered as best efforts. It was not always clear if remnants of modes other than the 00–mode were measured. For any larger change of the fundamental wavelength an optimization of all cavity alignments is necessary.

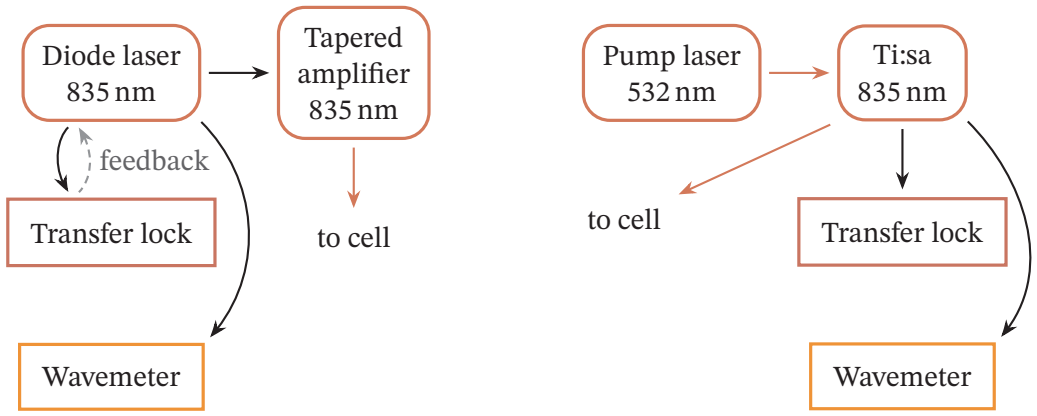

c) Red systems for $n(N^+) \leftarrow \mathrm{H}\,^2\Sigma^+$. On the left is the system belonging to the project. A diode laser (Toptica DLPro) is amplified by a TA (eagleyard) to about 350 mW. This system is only used for the characterization measurement shown in chapter 4, and currently not in use in favor of the system on the right, which is a Ti:sa system (M Squared Lasers), where about 250 mW is used at the cell.

Figure 3.1: Diagrams of the laser systems used to excite NO to a Rydberg state $n(N^+)$. We sent all respective fundamental beams to a wavemeter (HighFinesse WS-6). All fundamental beams are additionally sent to our locking setup, see section 3.3, though the Rydberg–Ti:sa system cannot be locked. This figure is divided over two pages.

The second system is a frequency–doubled diode laser running at 1080 nm (Toptica DLPro). This system is used to excite $H\,^2\Sigma^+ \leftarrow A\,^2\Sigma^+$. A sketch can be seen in figure 3.1b. For this system the fundamental beam refers to the beam emitted by the diode laser. The fundamental beam is both sent to a wavemeter and our locking setup, and additionally coupled into a fiber amplifier (Keopsys). The fiber amplifier allows a maximum power of 10 W, which is then coupled into a single–pass periodically–poled lithium niobate crystal (PPLN) (by HCPhotonics) used for frequency-doubling. We can achieve a reliable output of about 650 mW at 540 nm. The beam mode is Gaussian, and beam parameters are given in their corresponding experimental chapters. Since the linewidth of the fundamental laser is specified to be less than 50 kHz, we expect a linewidth of less than 100 kHz after doubling.

For the transition to a Rydberg state of NO, $n(N^+) \leftarrow H\,^2\Sigma^+$ at 835 nm[1], there were two options used. The setup built for this project originally is a Toptica DLPro diode laser amplified by a tapered amplifier (TA) to about 350 mW. The fundamental beam of the diode is sent to the locking setup and wavemeter. The diode system used has the disadvantage, that any tuning to another wavelength involves adjusting the diode's current and temperature such, that no mode–hop issues occur. This is tedious, when the necessity arises several times a day. Therefore, for the main experimental results of this thesis, another Ti:sa system was used. We were fortunate enough to have that option readily at the institute available. The linewidth should be on the order of 50 kHz. Again some light is sent to the wavemeter and locking setup. The system's mode is fully Gaussian, and it is without difficulty to give beam parameters. Filtering of the beam is done by a single-mode polarization-maintaining fiber. A sketch of both systems can be found in figure 3.1c.

For the power stabilization of the laser systems we use an acousto–optic modulator (AOM) for the 540 nm– and 835 nm beam. A simple sketch is shown in figure 3.2. An AOM generates higher-order modes due to diffraction. They exit the AOM under a different angle than the incoming beam. By adjusting the radio–frequency (RF)–amplitude modulation power of the AOM itself, it is possible to adjust the fraction of optical power diverted into higher modes. A pinhole only allows the zero mode to pass and a pickoff and photodiode provide feedback to a proportional–integral–derivative controller

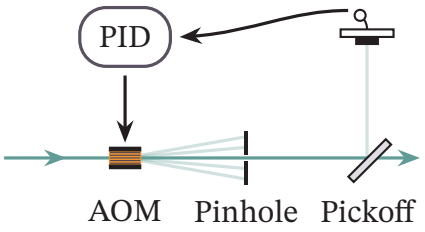

Figure 3.2: Sketch of a basic power stabilization setup. Details in the text.

[1]We tune this laser between 830 nm and 850 nm to access several Rydberg states. 835 nm is the "design"–wavelength used, thus the system is oftentimes just referred to by this wavelength.

(PID), which controls the amplitude modulation in turn. For the UV system an AOM is not possible, since no suitable devices are available to our knowledge. Instead, we replaced the AOM in figure 3.2 by a rotating $\lambda/2$–waveplate and a subsequent polarizing beam splitter cube. Other components remain the same. By adjusting the waveplate's angle, the power passing the cube in either direction can be adjusted. This is based on [79].

When all prerequisites are existing, the power–stabilized and frequency–stabilized (first transition, second transition) laser beams are then sent to our experimental cell. The UV beam passes the cell counter-propagating to the green and red laser beam, which is advantageous when considering the wavevector's mismatch, as will be seen in subsection 3.4.1. The green laser is the laser used for the second transition, $\mathrm{H}\,^2\Sigma^+ \leftarrow \mathrm{A}\,^2\Sigma^+$, since the transition wavelength $\approx 540\,\mathrm{nm}$ is in the visible green, and the red laser (or Rydberg laser, respectively) has its short–hand name as the Rydberg transition's wavelength is in the infrared (IR).

3.2 Gas mixing unit

Having the overall project goal of setting up a trace-gas sensor for NO in mind, the experiment needs gas mixtures of NO in a background gas. In future experiment this can be used to simulate different concentrations of NO in the exhaled breath. A good choice is N_2, as it doesn't react with NO and is the most abundant molecule in air. There are predefined mixtures of NO diluted in N_2 available ("test gases"), though flexibility is increased if we can mix arbitrary concentrations directly at the setup. The GMU has been extensively discussed in a previous work [16]. Thus, only a short overview will be given here.

A sketch of the setup can be seen in figure 3.3. The gas setup has three components: The GMU, the glass cell and the extraction by the pumps. A backing pump reduces the pressure to about 8 mbar, and a turbo pump reduces further to pressures on the order of $1 \cdot 10^{-5}$ mbar, when evacuating the setup. The goal was a possible dilution of NO by a factor of 10 000 [16]. Two gas inlets allow connecting an N_2 and an NO gas bottle. The GMU is realized with 6 mm–tubing. Instead of a bottle of pure NO, a pre-diluted bottle of NO in N_2 can be used, which allows reaching concentrations in the ppb–regime. Four mass–flow controllers (MFCs) can be used to adjust the gas flow through the experimental cell. We can adjust the amount of accessible MFCs by valves. The MFCs have a minimum and maximum flow rate of

- 0.1 sccm – 5 sccm,
- 2 sccm – 100 sccm,

- 40 sccm – 2 ksccm and
- 1 ksccm – 50 ksccm.

The unit sccm means “standard cubic centimeters per minute” and refers to the flow at standard conditions [16]. When operating the experiment, the first MFC is only accessible by NO, and the last one is only accessible by N_2. The resulting gas mixture is sent via pipes with end fittings of type Kleinflansch (KF)–10 to the cell. As can be seen in figure 3.3, the gas mixture may also bypass the cell leading directly to the pumps. To not waste gas, there is an additional bypass with thin pipes (6 mm–pipes) directly at the cell, so we can artificially reduce the flow. This is necessary, as the turbo pump can only be used at full force, yet pressures below 8 mbar are desirable. Otherwise, large flows would be necessary, reducing the gas in place considerably. If we use the cell’s bypass, we are able to maintain a constant flow and operate at gas pressures between $1 \cdot 10^{-3}$ mbar and 1.5 mbar by adjusting the two highlighted valves in figure 3.3. The pressure itself is the average value of two pressure gauges yielding pressures p_1 and p_2 directly before and after the cell. Any pressure calculated in this work is the average value of both pressure readouts. To justify, that we can simply take the average, it is necessary to look at the Knudsen number K. According to [81] we can define the number as:

$$K = \frac{\pi}{4}\frac{\overline{v} \cdot \mathcal{V}}{p \cdot d} \begin{cases} > 0.5 & \text{molecular flow} \\ < 0.01 & \text{viscous flow} \\ \text{else:} & \text{Knudsen flow} \end{cases} \tag{3.1}$$

Here, $\mathcal{V}$ is the viscosity and d is the flow cross-section. The mean velocity $\overline{v}$ of the molecules with mass m can be calculated with [82]

$$\overline{v} = \sqrt{\frac{8 k_B T}{m\pi}} \quad , \tag{3.2}$$

where k_B is the Boltzmann constant, and T is the temperature. As indicated in equation (3.1) different values allow distinguishing different flow types. In this work the gases NO and N_2 are used. Both have a viscosity $\mathcal{V} < 20\,\mu\text{Pa s}$ at $T = 300\,\text{K}$ [16]. The smallest cross-section in this experiment is 14 mm × 8.4 mm, and below a pressure of about 500 mbar we are in Knudsen flow ($T = 300\,\text{K}$). In a molecular flow we can treat the particles independently, and the approximation would be justified. In the case of Knudsen flow we have to take additional parameters into account. In any experiment we make sure, that both gauges show similar values. Any difference in pressure would indicate flow resistances. Based on experimental experience we are always able to make both pressure values p_1 and p_2 identical within the overall error. As such we are confident, that taking the average value is justified.

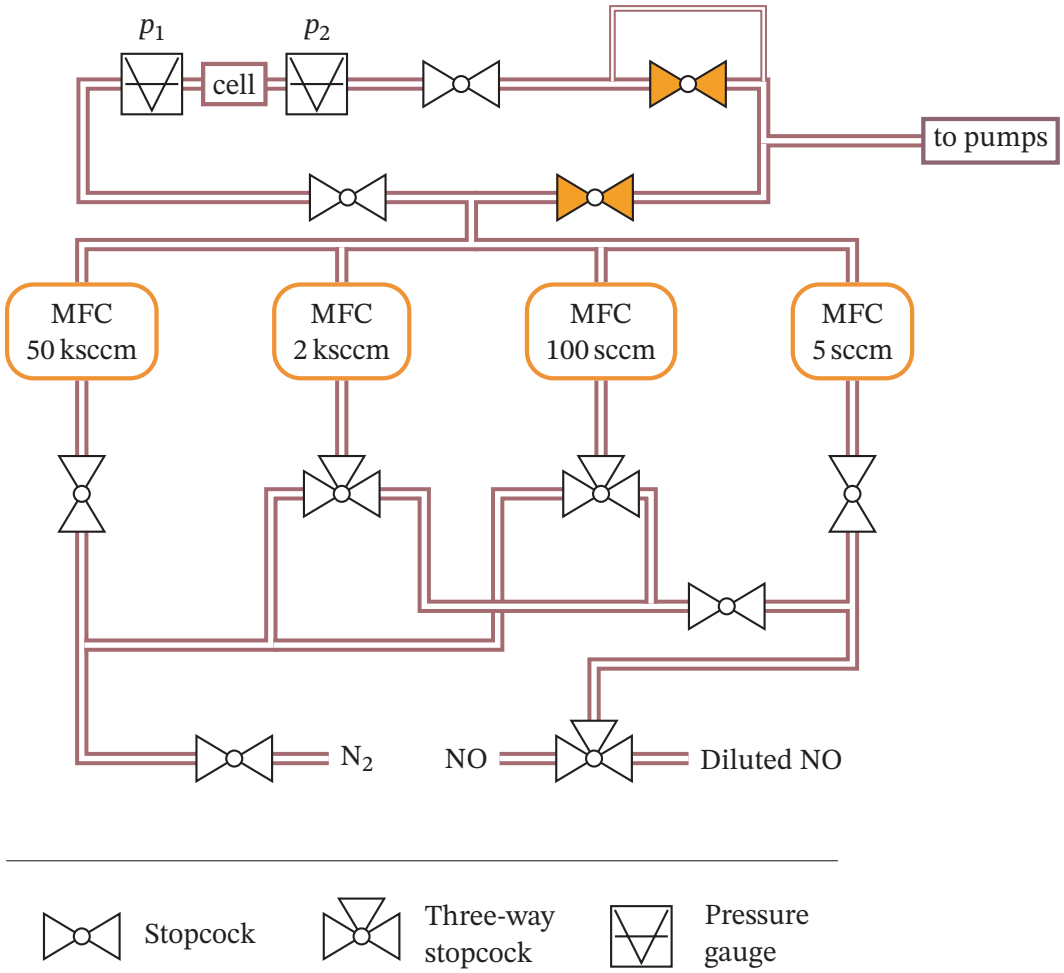

Figure 3.3: Sketch of the GMU. The setup allows connecting gas bottles of NO and N_2. Dilutions in the ppb–regime can be achieved by connecting a bottle of pre-diluted NO and pure N_2. The pumps are a backing pump in combination with a turbo pump. When evacuating, pressures on the order of $1 \cdot 10^{-5}$ mbar in the glass cell are typical. The pressures themselves are measured using two pressure gauges directly before and after the cell, p_1 and p_2. Pressures are regulated by MFCs, where four different controllers allow access to different flow ranges. Depending on the experiment performed, some of them may be completely off-line by closing the respective valves. After the cell (here on the right) a bypass, indicated by pipes of thinner radius, allows reducing the flow artificially. We then can reach higher pressures, while not wasting NO and keeping the volume in front of the turbo pump low. The two valves with a lighter color are explained in the text. A more in-depth description can be found in [16]. The symbols are taken from [80].

3.3 Frequency–stabilization setup

Lasers are subject to noise and environmental influences, and drift in frequency over time. To excite NO to a Rydberg state, the excitation lasers have to be tuned precisely to the wavelength of their respective transition. The second transition for example, $H\,^2\Sigma^+ \leftarrow A\,^2\Sigma^+$, has a full width at half maximum (FWHM) of only a few MHz in the experiment presented, as will be seen in subsection 4.3.1. The same holds true for the Rydberg transition. Thus, a frequency–stabilization setup had to be implemented. Such a setup oftentimes is also called a locking setup. Note that at this point of the project, the Rydberg transition is usually scanned, i. e. locking is not yet needed. Nevertheless, the locking setup provides a relative frequency reference, as will be seen. From now on, whenever referring to a cavity, a Fabry–Pérot interferometer (FPI) is meant. As we can only measure relative frequencies, any frequency calculated based on a transfer cavity is labeled as detuning of the respective transition. For example, $\Delta_{n(N^+)\leftarrow H}$ would be the detuning of the Rydberg transition.

The core of any locking setup is a stable frequency reference. The laser's frequency can then be tuned by giving active feedback to the system by using a PID. Such a reference may be an atomic or molecular resonance, an optical resonator or another laser, which is already stabilized. To use an atomic or molecular transition the exact transition frequency has to be known, as is for example the case for Rb. For NO it is possible to calculate the ground state transition, though the power in the UV is already low, thus we cannot spare any power for a stabilization setup. We therefore use the fundamental beams, see section 3.1. While there might be an atomic or molecular transition, which is at the frequency of our fundamental beams, the additional effort and inflexibility of such an approach lead to another solution.

Requirements on this locking setup were the ability to stabilize many different laser wavelengths, currently 7 as different projects are involved, keeping the linewidth on the order of only a few kHz and having great flexibility and scalability if future laser systems should be stabilized as well. In our case the solution uses a stabilized reference laser. This laser then serves as frequency reference to several transfer cavities, which in turn are a frequency reference to the actual lasers to be locked.

We stabilize our single reference laser running at 780 nm to an ultra-low expansion cavity (ULE). The ULE is actively temperature stabilized and evacuated. One may think of it as an absolute frequency–reference to our setup. The stabilized 780 nm–light serves as frequency-reference to stabilize the length of the self-built transfer cavities, which were developed in–house previously [83]. The length of the cavity is adjustable by a piezo glued to one of the mirrors. The mirrors of the transfer cavities are coated such, that it is optimal for the wavelength of the reference laser as

well as the wavelength of the laser to be locked. Finally, the beam of the laser to be locked can be stabilized to the transfer cavity.

There are several different ways of generating a so–called error signal for the PID. Requirements to the error signal is the ability to extract the information, if the laser is above or below the set frequency, as well as the amplitude of the deviation. When using a cavity the error signal is generated at the cavities' resonances. For all locks in the setup the Pound–Drever–Hall technique (PDH) is used [84, 85], which is a well-established procedure. An in-depth explanation of the technique is for example given in [86], and a review of different locking techniques featuring our setup is given in [87]. The PDH technique modulates the laser, and the error signal is generated by demodulating the signal. The advantage is, that one may choose the modulation at high frequencies shifting it away from technical noise, such as the frequency of the line voltage. In our case a modulation frequency of 15 MHz is used.

The principle for all locks used is the same. Each PDH lock monitors the reflected beam from a cavity. The optical setup is sketched in figure 3.4. In the setup this reflection is separated by using a polarizing beam splitter cube (PBSC), a quarter waveplate ($\lambda/4$) and a photodiode labeled with "Refl." for reflection. The reflection photodiode's output signal is sent to the input of a Red Pitaya STEMlab 125-14 (RP). Additionally, the transmission photodiode's signal labeled with "Trans." is sent to the RP's second input. The RP is a field–programmable gate array (FPGA) board featuring two inputs and two outputs. The software used to operate the RP is based on PyRPL [17]. It can provide us with an arbitrary signal generator (ASG), a module to generate the PDH error signal (IQ module) and implements a PI (no derivative part available). However, it is targeting only a single RP, and a single RP may only provide two PI modules. Yet, many of them are required for locking different laser systems and cavities. Thus, I wrote a software which essentially wraps several instances of PyRPL into a single unified user interface. While the PDH locking only needs the reflection signal, the transmission is used as a "lock watch", i. e. it enables us to monitor if the laser is still at the desired frequency or drifted that far away, that the respective PID was unable to account for it. We can also use the lock watch to monitor the lock of the transfer cavities as well as the stability of any power stabilization.

As mentioned, the PDH technique needs a modulated laser signal to generate the error signal. Every transfer lock is based on the same frequency modulation as the reference laser. Thus, the clock of the first RP is forwarded (by SATA cables) to all other involved RPs, yielding stable error signals. To make this work we adjusted the PyRPL FPGA code.

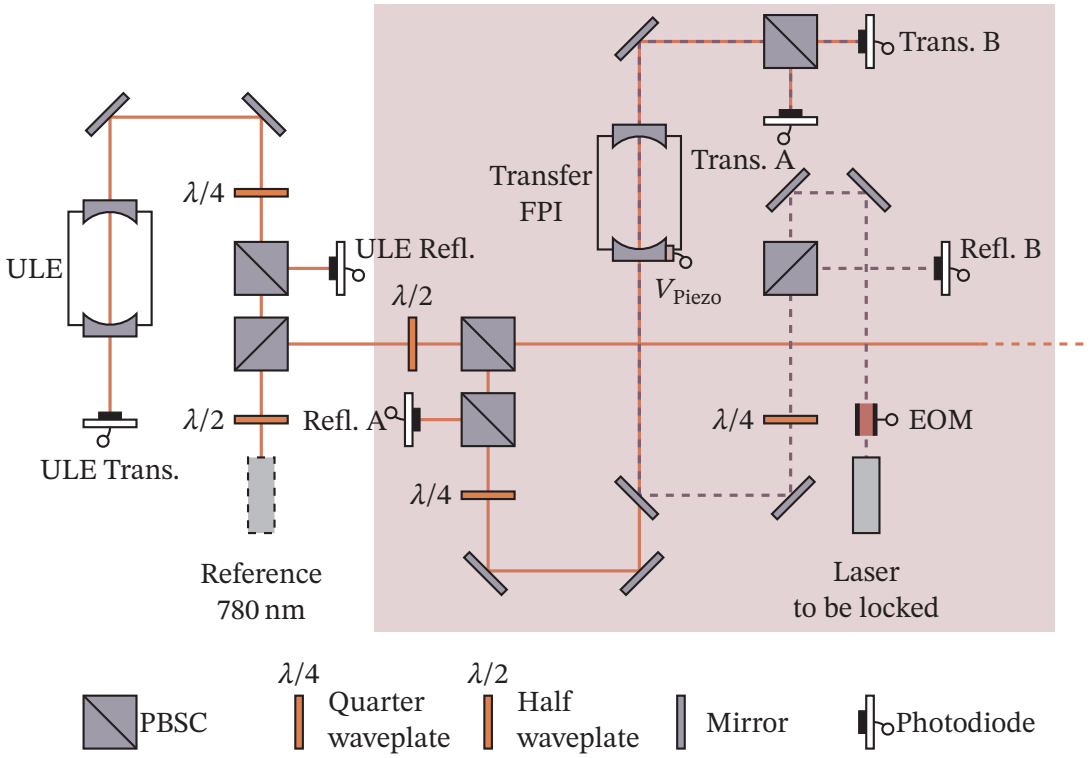

Figure 3.4: Sketch of the optical setup of the locking setup. The reference laser is a Toptica DLPro running at 780 nm and stabilized by using the PDH technique to an ULE. The feedback of the reflected light (ULE Refl.) is fed to a RP, which calculates the PDH error signal and additionally features the PID control to tune the laser. The then stabilized 780 nm is used to in turn stabilize the length of self-built transfer cavities by employing PDH again. The transfer cavities have mirrors where the coating is such, that it matches the reference beam and the laser to be stabilized. Finally, the laser to be locked can be stabilized on the transfer cavity by means of PDH. An EOM may give additional sidebands. The colored region can in principle be added as often as needed. More information can be found in the text and in [87].

In principle as many transfer locks as needed, can be added. This is the advantage of this approach. A transfer lock is depicted as the colored region in figure 3.4. Since the transition frequency is typically not overlapping with a resonance of the transfer cavity, electro-optic modulators (EOMs) are added to the laser beams of the transition lasers. An EOM allows adding sidebands to the laser's frequency, and hence to shift the error signal at the sideband's position to the desired position, since the sidebands can be tuned. The distance between the cavities resonances of the fundamental Gaussian mode is called free spectral range (FSR). This also means, that the maximum possible EOM frequency should be at least half of the FSR. To some up, these are the steps done every time to lock a single or multiple lasers:

1. Stabilize the reference laser to the ULE.
2. Stabilize all transfer cavities to the reference laser.
3. For each transition:
   a) Scan the transition laser over the molecular resonance.
   b) Tune the transition laser's EOM such, that its side band overlaps with the position of the molecular transition.
   c) Stabilize the transition laser to the transfer cavity.

An example for typical signals seen during the locking procedure is shown in figure 3.5.

3.3.1 Lock–error estimation

Within the scope of this work the first two transition lasers, i. e. the lasers for $A\,^2\Sigma^+ \leftarrow X\,^2\Pi_{3/2}$ and $H\,^2\Sigma^+ \leftarrow A\,^2\Sigma^+$, are usually locked. The lock error estimates, how exact we know the laser's frequency. In the introduced locking setup there are several contributions to the lock error, which are the stability of the reference laser lock, the stability of the transfer cavity lock and the stability of the actual laser lock. As the reference laser is used by several projects, it was thoroughly analyzed in [88]. The linewidth of the lock was determined to be $\Delta\omega_{\text{Reference}} = 2\pi \times 121\,\text{kHz}$. As the lock of the transfer cavity influences the lock of its respective experimental laser, these two have to be added together before calculating the overall error.

The lock error of the ground state transition was already calculated to be [16]

$$\begin{aligned}\frac{\Delta\omega_{\text{UV}}}{2\pi} &= \frac{4}{2\pi}\cdot\sqrt{\left(\Delta\omega_{\text{Transfer 904}} + \Delta\omega_{904}\right)^2 + \Delta\omega^2_{\text{reference}}} \\ &= 4\cdot\sqrt{(229.9\,\text{kHz} + 202.6\,\text{kHz})^2 + (121\,\text{kHz})^2} \approx 1.8\,\text{MHz} \quad ,\end{aligned} \tag{3.3}$$

and the factor of 4 accounts for the frequency–quadrupling.

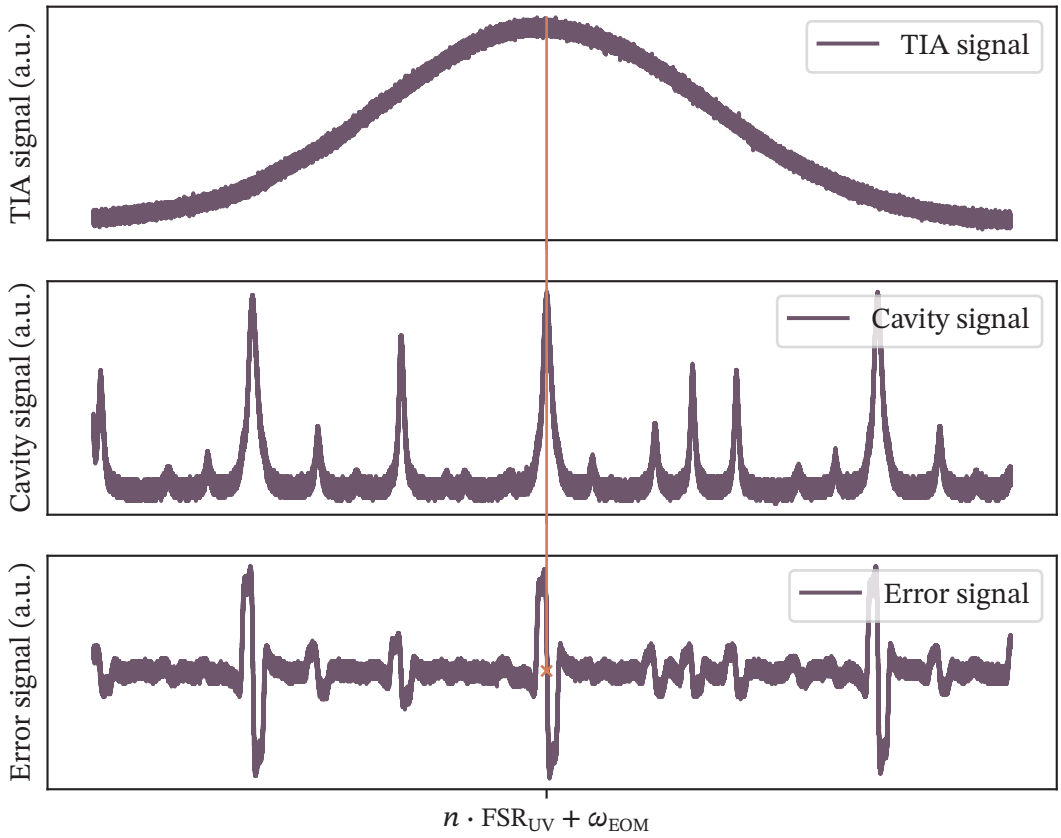

Figure 3.5: Example of the $A\,^2\Sigma^+ \leftarrow X\,^2\Pi_{3/2}$ signal (top plot) prior to locking. This is the signal as generated by the UV beam at ≈ 227 nm, and it is Doppler-broadened. The center plot shows the transfer cavity transmission signal, i. e. the signal of the fundamental beam, at $\approx 4 \cdot 227\,\mathrm{nm} = 908\,\mathrm{nm}$. Several peaks can be seen. The lowest ones in amplitude are remnants of other modes. The higher ones are either peaks corresponding to the FSR of the cavity, or peaks shifted by the frequency of the EOM ω_{EOM}. Setting the EOM frequency allows moving a peak below the maximum UV signal, which is the desired locking position and indicated by a vertical line. The lowest plot shows the generated PDH signal, where a steep slope is visible at the locking set point marked by a cross.

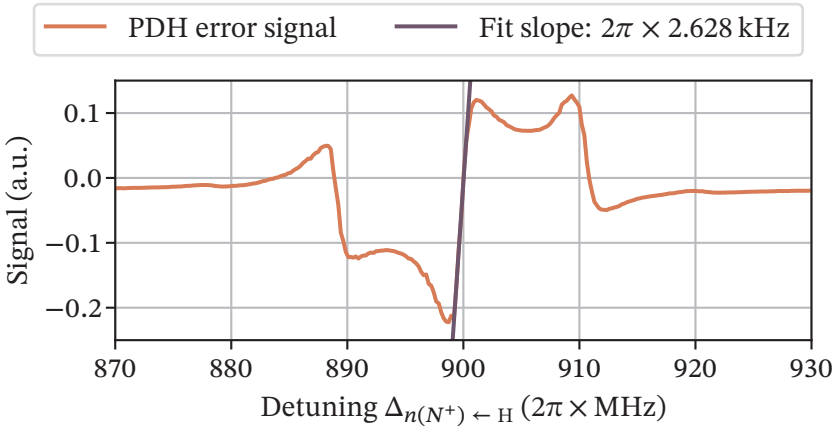

Figure 3.6: PDH example signal of the Rydberg laser's transfer cavity. The frequency axis has been calculated using the known FSR of the cavity. The fitted slope gives a scaling factor to the lock error.

In general, a lock error is estimated like follows. The slope of the error signal is fitted using a linear function. Its inversion yields a scaling factor in MHz V^{-1}, since either the known EOM frequency or known FSR of the respective cavity serves as a frequency reference. A plot is shown in figure 3.6. As soon as the laser is locked, the error signal becomes a noisy, yet flat line. The root–mean square of this line times the scaling factor yields the lock–error estimate. The following lock errors were calculated:

$$\Delta\omega_{\text{Reference}} = 2\pi \times 121\,\text{kHz} \tag{3.4a}$$
$$\Delta\omega_{\text{Transfer 904}} = 2\pi \times 229.9\,\text{kHz} \tag{3.4b}$$
$$\Delta\omega_{904} = 2\pi \times 202.6\,\text{kHz} \tag{3.4c}$$
$$\Delta\omega_{\text{UV}} = 2\pi \times 1.8\,\text{MHz} \tag{3.4d}$$
$$\Delta\omega_{\text{Transfer 1080}} = 2\pi \times 157.9\,\text{kHz} \tag{3.4e}$$
$$\Delta\omega_{1080} = 2\pi \times 668.5\,\text{kHz} \tag{3.4f}$$
$$\Delta\omega_{\text{Green}} = 2\pi \times 1.7\,\text{MHz} \tag{3.4g}$$
$$\Delta\omega_{\text{Transfer 835}} = 2\pi \times 104.5\,\text{kHz} \tag{3.4h}$$

For the frequency axis calculated by the cavity signal of the Rydberg laser's transfer cavity this yields an error estimate of

$$\frac{\Delta\omega_{\text{Rydberg reference}}}{2\pi} = \frac{1}{2\pi}\sqrt{(\Delta\omega_{\text{UV}})^2 + (\Delta\omega_{\text{Green}})^2 + (\Delta\omega_{\text{Transfer 835}})^2} \approx 2.5\,\text{MHz} \quad . \tag{3.5}$$

3.4 Concepts

3.4.1 Broadening

In this experiment absorption spectroscopy is performed, though the experimental signal is obtained by detecting the current generated by free charges. This is in contrast to any optical spectroscopy, where the experimental signal is acquired by using any optical sensor like a photodiode. Still broadening effects of the line play a role, and a very brief overview is given here based on standard text books in atomic physics [70, 82, 89].

Any excited state has a lifetime τ, which is inversely proportional to its natural linewidth $\Gamma = 1/\tau$. The Rabi frequency Ω gives the frequency of the population transfer when the transition is driven resonantly. The transition frequency shall be denoted by ω_0.

Two different types of broadening are distinguished, homogeneous and inhomogeneous broadening. Inhomogeneous broadening is the result of fluctuations different for each particle, whereas for homogeneous broadening the fluctuations are the same for all involved particles. Inhomogeneous broadening has typically a Gaussian lineshape. Homogeneous broadening is mostly described by a decay constant, which yields a Lorentzian lineshape. The natural lineshape is Lorentzian as well. The FWHM shall be denoted by γ.

Power or saturation broadening is the result of the reduced absorption when driving a transition resonantly above the saturation intensity. Within the linewidth γ the absorption stays the same. The saturation intensity I_{sat} gives the turning point, where significant broadening occurs. Power broadening is homogeneous, and the FWHM γ_{power} is given by [89]

$$\gamma_{\text{power}} = \Gamma\sqrt{1 + \frac{I}{I_{\text{sat}}}} \quad , \tag{3.6a}$$

$$I_{\text{sat}} = \frac{\pi hc}{3\lambda^3\tau} \quad . \tag{3.6b}$$

Here $\lambda = 2\pi c/\omega_0$ is the wavelength, h is the Planck constant and c is the speed of light.

Pressure or collisional broadening is a broadening resulting from collisions between particles, which reduces the lifetime. As such it depends on the collisional cross

section σ and the mean velocity $\overline{v}$. The homogeneous FWHM at a density N is given by [82]

$$\gamma_{\text{pressure}} = 2\pi \cdot N\sigma\overline{v} \quad , \tag{3.7a}$$

$$\overline{v} = \sqrt{\frac{8k_{\text{B}}T}{m\pi}} \quad , \tag{3.7b}$$

where k_{B} is the Boltzmann constant, m is the particle's mass and T is temperature.

The transit-time broadening is the result of a particle passing through a laser beam of diameter d within a time $t = d/\overline{v}$. The time t does not necessarily correspond to τ. The broadening is homogeneous and for a perpendicular beam with diameter d passed, the FWHM is given by [82]

$$\gamma_{\text{transit}} = \frac{4\overline{v}}{d\sqrt{2\log 2}} \quad . \tag{3.8}$$

The Doppler broadening is an inhomogeneous broadening effect having its origin in the movement of the particles. Due to the Doppler effect, the frequency of the laser beam ω_{L} shifts when considering it in the laboratory frame of the particle, $\omega = \omega_{\text{L}} \pm kv$ [89]. The wavevector k and the velocity v have sign $\pm$, which denotes the direction in relation to the laser beam. The equation is written for one dimension, i. e. the particle is moving towards the laser beam seeing a higher frequency or away seeing a lower one. By considering the Maxwell-Boltzmann distribution the FWHM can be calculated to [89]

$$\gamma_{\text{Doppler}} = \frac{\omega_0}{c}\sqrt{\frac{8\log(2)k_{\text{B}}T}{m}} \quad . \tag{3.9}$$

Note however, that I was unable to find any reliable value for the saturation intensity of the $\text{A}\,^2\Sigma^+$ state, the values in literature differ by orders of magnitude [90–92]. However, based on [34] there is confidence that we are unable to saturate the transition. Thus, no value for the power broadening can be given. The transit-time broadening depends on the beam diameter. A diameter of 200 µm is used exemplarily. For the Doppler broadening a temperature of $T = 293\,\text{K}$ is used. The mass of NO is 30 u. For

the Doppler and transit-time broadening calculation yields

$$\gamma_{\text{Doppler, A}\leftarrow\text{X}} \approx 2\pi \times 2.97\,\text{GHz} \quad , \tag{3.10a}$$

$$\gamma_{\text{Doppler, H}\leftarrow\text{A}} \approx 2\pi \times 1.24\,\text{GHz} \quad , \tag{3.10b}$$

$$\gamma_{\text{Doppler, } n(N^+)\leftarrow\text{H}} \approx 2\pi \times 0.80\,\text{GHz} \quad , \tag{3.10c}$$

$$\gamma_{\text{transit}} \approx 2\pi \times 7.7\,\text{MHz} \quad . \tag{3.10d}$$

The Doppler broadening of the second and final transition can be reduced by letting the beams counter propagate, as is the case in our setup. As long as the Doppler broadening is dominant in comparison to the natural linewidth Γ of the transition, an estimate of the expected linewidth can be given. In [34] the Doppler–free linewidth is less than $2\pi \times 15\,\text{MHz}$, and using the wavevector mismatch yields

$$\frac{\gamma_{\text{Rydberg}}}{2\pi} = \left[\frac{1/226\,\text{nm} - 1/540\,\text{nm}}{1/226\,\text{nm} - 1/540\,\text{nm} - 1/835\,\text{nm}}\right] \cdot 15\,\text{MHz} \quad \approx 8\,\text{MHz} \tag{3.11}$$

as a lower bound for the linewidth of the Rydberg transition.

For the collisional broadening the pressure has to be known. This will be extensively analyzed in section 5.4.

3.4.2 Line shapes

Depending on the dominant broadening effects a line may either be mainly Lorentzian or mainly Gaussian. A Lorentzian function is given by

$$f_{\text{Lorentz}}(x,\gamma) = \frac{C}{(x-x_0)^2 + \left(\frac{\gamma}{2}\right)^2} \quad , \quad C_{\text{area}} = \frac{\gamma}{2\pi} \quad , \quad C_{\text{amplitude}} = \left(\frac{\gamma}{2}\right)^2 \quad , \tag{3.12a}$$

$$\text{FWHM}_{\text{Lorentzian}}, \gamma_L = \gamma \quad , \tag{3.12b}$$

where x_0 is an offset from zero and the normalization can be chosen such, that the function is either normalized to its amplitude $C_{\text{amplitude}}$ or its area C_{area}. A Gaussian

function is given by

$$f_{\text{Gaussian}}(x,\sigma) = C\exp\left[-\frac{(x-x_0)^2}{2\sigma^2}\right] \quad , \quad C_{\text{area}} = \frac{1}{\sqrt{2\pi\sigma^2}} \quad , \quad C_{\text{amplitude}} = 1 \ , \tag{3.13a}$$

$$\text{FWHM}_{\text{Gaussian}}, \gamma_G = 2\sqrt{2\log(2)}\sigma \quad . \tag{3.13b}$$

σ is called the standard deviation. If inhomogeneous and homogeneous broadening are contributing equally, a Voigt profile should be chosen. It can only be evaluated numerically and is a convolution of the area–normalized Gaussian and Lorentzian profile given by [93]

$$f(x,x_0,\gamma_L,\sigma) = \int_{-\infty}^{\infty} f_{\text{Gaussian}}(x',\sigma) f_{\text{Lorentz}}(x-x_0-x',\gamma_L)\mathrm{d}x' \quad . \tag{3.14}$$

The FWHM is given, with an inaccuracy of 0.02 %, by [94]

$$\text{FWHM}_{\text{Voigt}}, \gamma_V \approx \frac{1}{2}\cdot\left[1.0692\frac{\gamma_L}{2} + \sqrt{0.86639\left(\frac{\gamma_L}{2}\right)^2 + 4\gamma_G^2}\right] \quad . \tag{3.15}$$

3.4.3 Intensity

In dependence of power P and waist w the mean intensity $\mathcal{I}$ of a Gaussian beam is [82]

$$\mathcal{I} = \frac{P}{\pi w^2} \quad . \tag{3.16}$$

Note especially that I do not use the peak intensity, which would be twice this value. Equation (3.16) will be used to calculate the intensities from the measured beam waist and power in this thesis.

4 A glass cell for electronic readout

In chapter 3 the GMU was introduced. However, we started with sealed cells at first, and expected the necessity of the GMU only as soon as gas mixtures are meant to be used.

The institute this project is located at has a long history on research done in Rb or Cs vapor cells, e. g. [14, 95–97]. Thus, it was natural to manufacture sealed cells first, i. e. quartz glass cells which were manufactured in-house, then evacuated, filled to a certain pressure of NO and sealed to be placed into the experiment. We were able to perform absorption spectroscopy on the $A\,^2\Sigma^+ \leftarrow X\,^2\Pi_{1/2}$ transition [53]. During the scope of a Master's thesis [98] it became clear, that the UV transition at 226 nm non-reversibly destroys the molecule. Consequently, the absorption signal became weaker over time, while the cell's color turned brown. This proved at least, that something else than NO was produced, most likely NO_2.

At a very early point through-flow cells were designed and produced [99]. The cells shown in this chapter were in through-flow from the start. A "game-changer" has been the idea to simply glue a printed circuit board (PCB) to the cell, since we proved that NO does not affect the vacuum epoxy we used, named *Torr Seal*. This is in contrast to the work done with Rb, were anodic bonding was used exclusively [11].

4.1 Cell types

The glass cells are manufactured in-house by the faculties' glassblower. The glass frame is made of borosilicate, which makes it easy to process. However, this type of glass shows basically no transmission in the deep UV [100], making it unsuitable for the UV laser. Therefore, we drill holes into the cell frame, and then glue patches of fused silica to the frame. The vacuum epoxy in use is *Torr seal*.

In this work, whenever referring to the old cell a cell with an electrode distance of $d = 20\,\mathrm{mm}$ is meant, and the circuit in version 1 is used. The new cell however has electrodes at a distance of 8.4 mm apart, and the circuit in version 2 is used. We will discuss both circuit versions in this chapter. Figure 4.1 shows a picture of the old cell, whereas in figure 4.2 a collage of different cell pictures of the new cell is shown.

The connectors to the vacuum setup are KF–10. Depending on the cell, the pipe has to be tapered off, in order to allow decreasing the distance between the electrodes. It doesn't matter which way round the cell is placed into the setup. In the following a close look at the readout electronics is given.

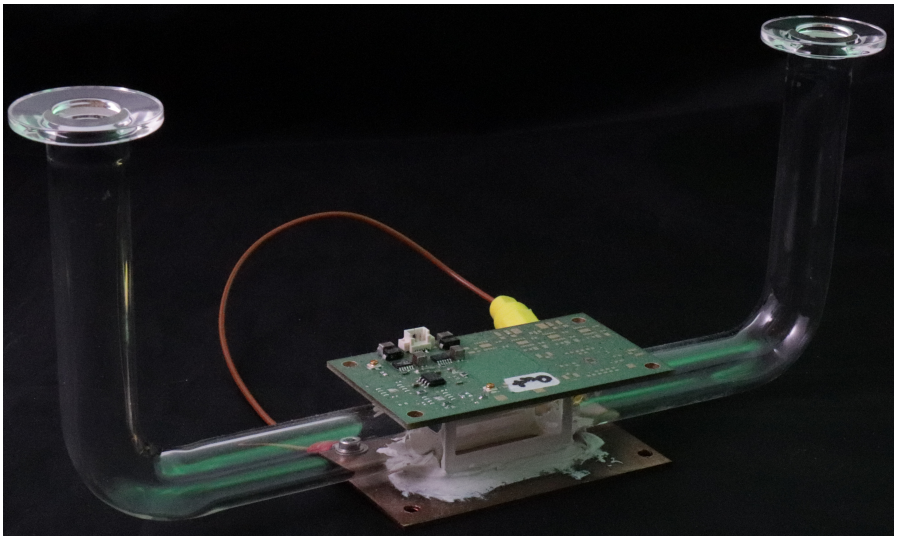

Figure 4.1: Photo of the old cell. The top–bottom (electrode) distance is 20 mm. The frame is made of borosilicate, but to front and back quartz windows are glued. The PCB on top has circuit v1, which will be introduced in subsection 4.2.5. The cable on the back connects the copper plate on the bottom.

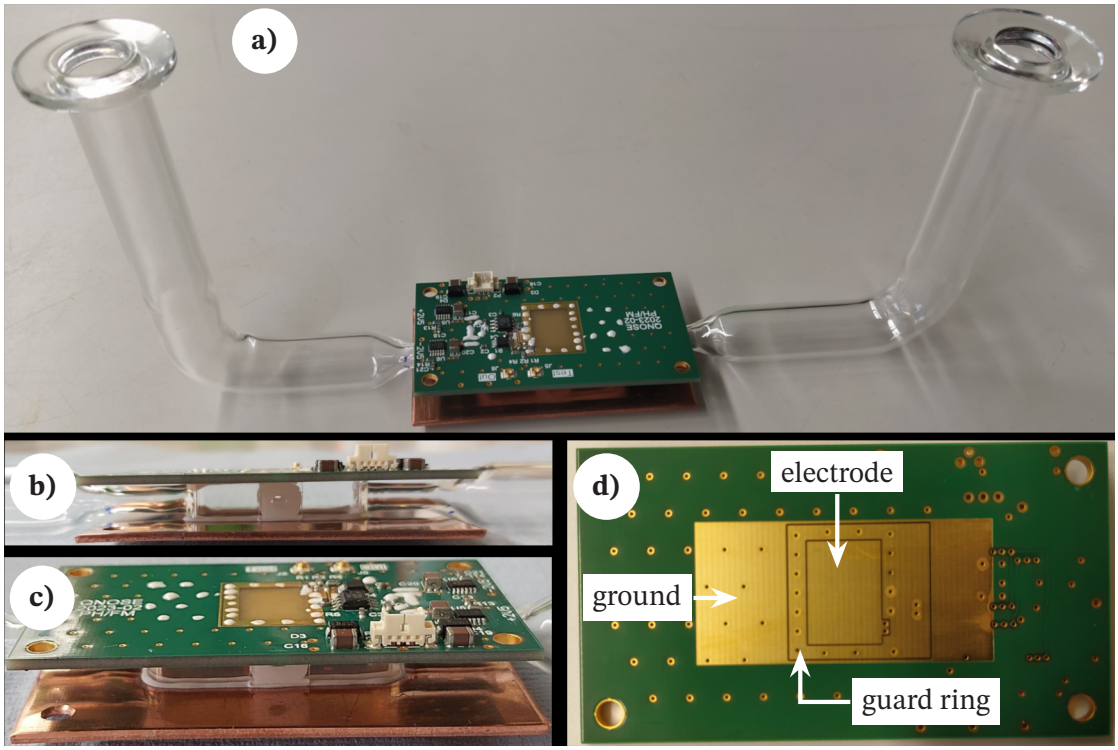

Figure 4.2: Several pictures of the so–called new or current cell. In **a)**, a picture of the complete cell is shown. The PCB is glued to the top, whereas a copper plate is glued to the bottom. The distance between top and bottom is 8.4 mm. In **b)** and **c)** we see magnified versions. Quartz windows are glued to the borosilicate frame to let the UV beam through. Image **d)** shows the bottom side of the PCB before glue was applied. The labeling and the circuit v2 will be explained in subsection 4.2.5.

4.2 Implementation of current sensing

To detect the targeted concentrations of nitric oxide, it is necessary to read out currents within the pA to nA range generated by the free charges within the cell, as was visualized in figure 1.1. The range is based on the experience gained during the proof–of–concept experiment [11] as well as on experimental results. The circuit design is done in cooperation with the IIS at the University of Stuttgart. Before we can discuss different possibilities, it is worth considering the fundamental limits first.

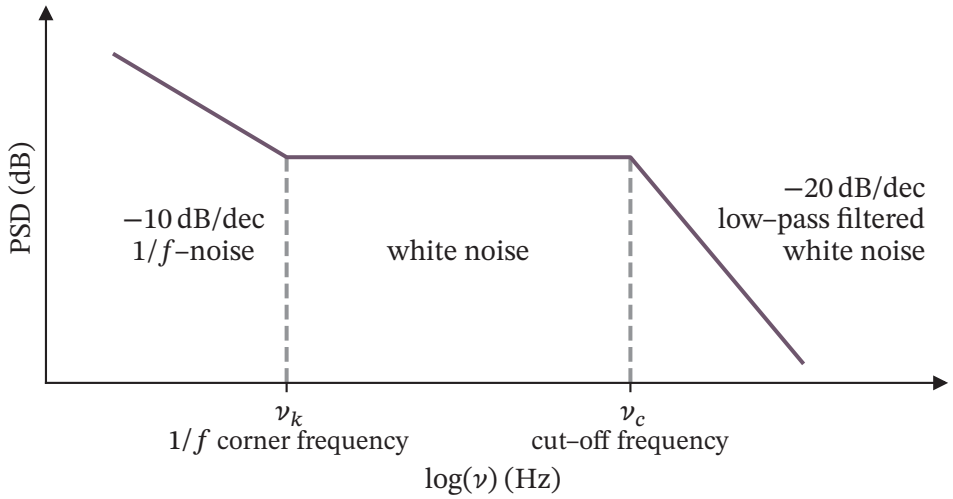

Figure 4.3: Typical noise behavior given by the PSD in dependence of the frequency. Graphic in accordance with [101].

4.2.1 Noise and errors

Any electronic network is subject to noise, and thus any frontend used to read out currents originating from a sensor as well. All contributions to the noise introduced here are stochastic. Brownian motion or the thermal excitation of charge carriers is temperature-dependent. Furthermore, the shot-noise $\sqrt{2qI}$ [102] is a fundamental limit and the result of the quantization of the electric charge. Note that in a physics context, sometimes the shot noise is only the noise of a single electron, yet in electronics usually the current is looked at, which combines the contribution of many electrons. The $1/f$ noise has its origin mostly in semiconductors, e. g. transistors, where the so-called flicker noise occurs due to irregularities in their structure, which is oftentimes found at the crossover between gate and semiconductor [101].

To quantify the noise behavior itself the power spectral density (PSD) is used. It essentially describes how much power can be found in any frequency band. A typical PSD shape can be seen in figure 4.3. For lower frequencies the $1/f$–noise dominates. At the $1/f$ corner frequency the noise turns mainly into white noise, which has a constant PSD. At the cut-off frequency this white noise becomes low–pass filtered [101]. Note that the low–pass itself is the result of the circuit, i. e. the limitation in bandwidth causes the slope, but the PSD would have stayed constant otherwise. The typical slopes are denoted in the figure.

The so called spurious–free dynamic range (SFDR) defines, in which range the measured power P_{out} is linearly dependent on the power send in P_{in}. Additionally, it

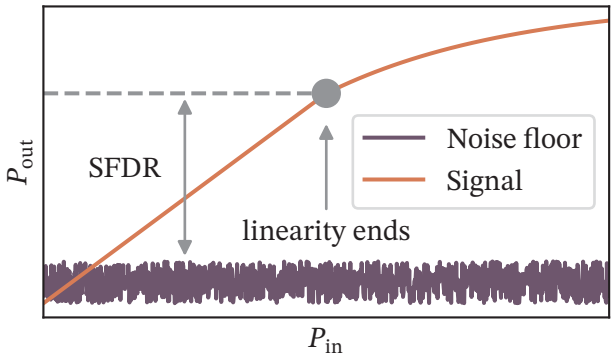

Figure 4.4: The SFDR is defined as the readout range, where the electronics perform linear and are above the intrinsic noise floor. Thus, the lower end is limited by noise, whereas the upper end is limited by distortion. Graphic as seen in [101].

has to be above the noise floor P_{noise}. Limitation occurs as soon as distortion kicks in and the behavior is not linear anymore. A sketch is shown in figure 4.4.

Another quantity is the limit of detection, which is the minimum level measurable as long as reproducibility is assured. The sensitivity represents how much the sensor's output changes compared to its input, and the dynamic range is the range between the limit of detection and maximum detectable peak.

4.2.2 Current frontends

From a naive point of view a simple resistor R should suffice for converting current into a voltage, as Ohm's law states $V = R \cdot I$, making the read-out voltage V directly proportional to current I. This project's currents are in the pA to nA–regime. To produce some meaningful voltage level reliably detectable by an oscilloscope, we would need a resistance in the at least MΩ–regime. This introduces a low-pass with a low corner frequency $\nu = 1/2\pi RC$ [102] due to the capacitive nature of the sensor. In turn, we end up with a very slow readout circuit. For a capacitive sensor, as is used in this experiment, the charge carriers passing the resistor change the potential at the electrodes. This means that a change in the sensed current would also change the voltage at the electrodes, yielding an unreliable readout. Thus, a simple resistor is not sufficient.

There are numerous possibilities on implementing a current sensor frontend. A general overview is given in [103], whereas [102, 104] are focusing more on TIAs.

An option presented in [103] is a current conveyer, which amplifies the input current to an output current. Advantages are their low input impedance, and they are

not that sensitive to parasitic input capacities in comparison to other solutions. The subsequent higher current decreases the demands on the following circuits, especially in terms of sensitivity. However, the main instruments used in the lab, i. e. all oscilloscopes and so on, work in the voltage domain. While a current conveyer could be used as preamplifier, and a subsequent circuit would convert from current to voltage, a circuit where this conversion is already built–in is the easier choice, since the output can be directly connected to an oscilloscope. As such a current conveyer proved not to be the most effective for the project.

Another option would have been a continuous–time current–mode ΔΣ–modulator [103–105]. Here, a comparator yields an implicit digitization. Thus, a ΔΣ–modulator gives a continuous bit stream, which needs subsequent digital processing. Additionally, a ΔΣ–modulator always evaluates the full frequency spectrum, while in this experiment the needed spectrum (e. g. the modulation frequency used for the lock-in amplifier) is known. Therefore, a ΔΣ–modulator would introduce unnecessary complexity, making it a bad choice for the experiment discussed in this work.

In this work a TIA is used to convert from current to voltage. It appeared to be the most sensible choice, as the output of the circuit is in the voltage range and the relationship between input current and output voltage is simply defined by the feedback resistance R_{FB} and Ohm's law, as long as operation in the design bandwidth is ensured [103, 106]. A TIA is a circuit based on an operational amplifier, which we will have a look at next.

4.2.3 Basics of operational amplifiers

While in the ideal world an OpAmp would have an infinite gain [107], this in reality obviously doesn't exist. In the scope of this work the internal workings of an OpAmp, i. e. the underlying circuit of the OpAmp itself, are not of importance, however, the implications are. This is what this section focuses on. In figure 4.5a an OpAmp in an open–loop configuration is shown. Here, no feedback network is connected, whereas a closed–loop configuration as shown in figure 4.5b has a feedback network implementing feedback factor β. The amplified signal for an open–loop configuration is [101]

$$V_{\mathrm{out}} = A(\omega)(V_- - V_+) \quad , \tag{4.1}$$

where $A(\omega)$ is the open-loop gain, and V_{out}, V_- and V_+ are the voltages as denoted in the figure. This means an OpAmp amplifies the difference of the input voltages. It is important to note, that the open–loop gain itself is frequency–dependent, as can be seen in figure 4.6. The reason an OpAmp is usually not used in an open-loop configuration boils down to the maximum voltage which can be amplified, the

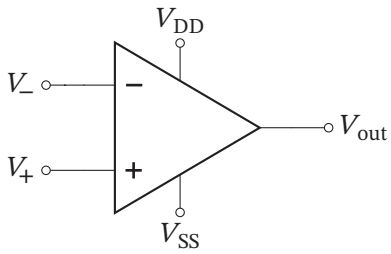

a) Schematic of an open–loop circuit.

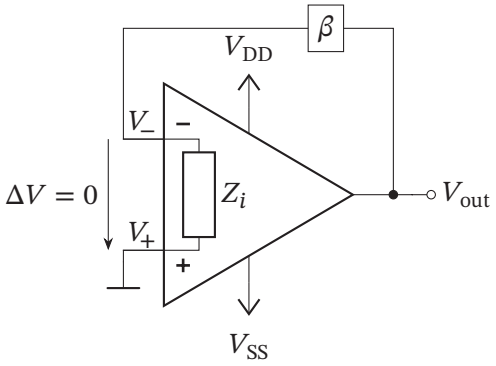

b) Schematic of a closed–loop circuit with negative feedback introducing feedback factor β, input impedance Z_i, input voltages V_- and V_+, as well as the output voltage V_{out}.

Figure 4.5: Circuits of OpAmps in open– and closed–loop configurations. Supply voltages are denoted by V_{DD} and V_{SS}. The graphics are based on [101, 106, 107].

limitation in bandwidth and fluctuations within the manufacturing process. Even a minimal offset would cause the OpAmp to output its maximum voltage. The maximum output voltage is limited by the supply voltages V_{DD} and V_{SS}. Since in the real world the open-loop amplification $A(\omega)$ is very high by design ($\gg 1 \cdot 10^5$) [107], the maximum input voltage might be as low as µV.

On the other hand, figure 4.5b shows an OpAmp in closed–loop configuration with negative feedback. If the input impedance Z_i is assumed to be infinite, circuit analysis yields for the back coupling [101, 107, 108]

$$\frac{V_{out}}{V_{in}} = \frac{A(\omega)}{1 + \beta A(\omega)} \overset{\beta A(\omega) \gg 1}{\approx} \frac{1}{\beta} \quad . \tag{4.2}$$

The magic lies in equation (4.2), which is called the transfer function and shows, that an (ideal) OpAmp amplifies the difference between the input voltages. While the frequency–dependent open–loop gain $A(\omega)$ might vary between several units of the same OpAmp, the feedback network introducing the feedback factor β can be well-defined by the user. The open–loop gain $A(\omega)$ is sometimes called forward gain as well, and $\beta A(\omega)$ may be denoted as loop gain. At the same time equation (4.2) also gives a figure on the error in amplification and offset introduced, since it largely depends on the assumption if $\beta A(\omega) \gg 1$. As such there is an error in the amplification. Furthermore, it is assumed that the input impedance Z_i is infinite. For the application as a TIA a high input impedance is especially important, to prevent leakage currents.

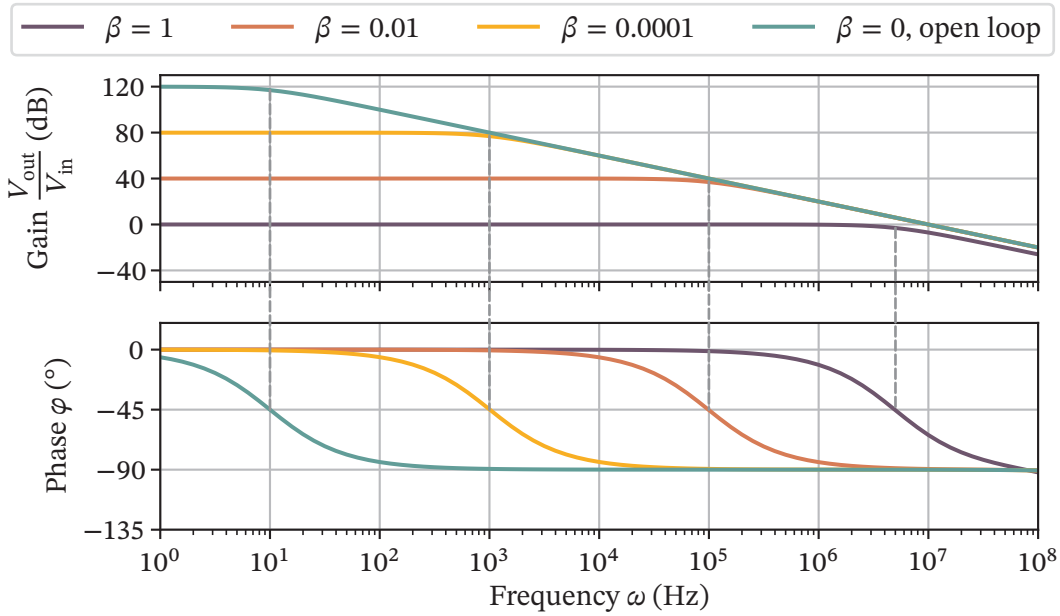

Figure 4.6: Exemplary simulated Bode plot for a generic operational amplifier (LTspice "Universal OpAmp 2" [109]), where the input voltage applied to the inverting input. The dashed lines are at the pole frequency of the respective feedback factor β.

If the assumptions are acceptable one may also talk of the virtual short concept, since $\Delta V = 0$ as indicated in figure 4.5b. The virtual short also defines the voltage drop over the capacitive sensor, thus there is a well-defined potential in contrast to the mere resistor previously introduced.

In figure 4.6 an exemplary Bode plot is given. All simulations are done using the software "LTspice" [109]. A Bode plot is a plot where the frequency response of the gain and the phase are plotted next to each other [107]. At first the slope of $A(\omega)$ is $0\,\mathrm{dB\,dec^{-1}}$. Overall the pole introduces a phase shift by 90°. At the pole frequency the phase is shifted by 45°, the amplitude decreases by 3 dB and the slope changes to $-20\,\mathrm{dB\,dec^{-1}}$. Further poles reduce by another $-20\,\mathrm{dB\,dec^{-1}}$ and 90° and so on [107]. On the other hand zeros have the reciprocal behavior. The system can be fully analyzed and understood by looking at poles and zeros as they define the overall performance of the system. The nominator and the denominator of the transfer function can be factorized such, that poles and zeros can be deduced directly [107].

In dependence of β the bandwidth can be adjusted. The bandwidth is the frequency range where the OpAmp operates in a well-defined manner. For larger values of β the bandwidth increases, and for a feedback factor $\beta = 1$ a maximum bandwidth can be achieved. This configuration is called a buffer configuration [110].

The gain–bandwidth product (GBW) is the multiplication of the gain and the bandwidth of the configuration, and also called the transit frequency [110]. If the phase shift is less than 180° at the transit frequency, the OpAmp can operate stable if used in negative feedback. For different β the GBW remains a constant of the system, if the system is defined by a single dominant pole [107]. A dominant pole means that the cut-off frequency is defined by a single pole [107].

As was seen in figure 4.6 the phase of the output signal shifts relative to the one of the input signal in dependence of the frequency as a result of poles in the transfer function. The difference itself is called phase margin, which is defined as the phase value at 0 dB–amplification subtracted from 180° phase [110]. If the phase shift at the transit frequency would be 180°, then the feedback would be positive, resulting in an instability of the circuit. Here the phase margin would be zero. Thus, the larger the phase margin, the better. Desirable is a phase margin over 60° [111].

In an actual application of an OpAmp it is not guaranteed, that the characteristic curves always look as shown in figure 4.6. An OpAmp which can be used while all the output is fed back into the input, i. e. with a feedback factor $\beta = 1$, is called unity-gain stable. Typically, off-the-shelf components are unity-gain stable, since this makes them usable for a large area of applications. When the OpAmp is self-designed however, unity-gain stability might not be needed, e. g. because β is always less than 1. On the other hand an OpAmp well-behaving at lower feedback factors might show peaking or ringing at other gains. Peaking means, that an undesired high amplification peak for higher frequencies occurs [101]. An example will be shown in subsection 4.2.4. Ringing can be seen in the time domain, here the output is stable only after a certain amount of time [101]. An OpAmp always has an input offset adding to the error as well.

Other important properties beside gain and offset of a non-ideal OpAmp are the common-mode rejection ratio (CMRR) and slew rate [110].

As shown in equations (4.1) and (4.2) an ideal OpAmp amplifies the difference of the input voltages, i. e. the so–called differential mode. However, a small additive amount of the input voltages named common mode is amplified as well, which is not desired. The equation can be adjusted to [108]

$$\frac{V_{\text{out}}}{V_{\text{in}}} = \frac{A(\omega)}{1 + \beta A(\omega)} \cdot \left(1 + \frac{1}{G}\right) \quad . \tag{4.3}$$

The ratio between both gains G is called CMRR, and should be as high as possible.

The slew rate describes how fast an OpAmp can adapt its output voltage in dependence of a change at the inputs [110].

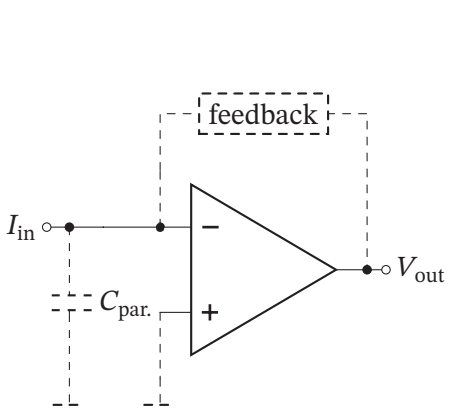

a) General circuit of a TIA. A parasitic capacitance $C_{par.}$ may alter the expected output. The feedback may be realized in several ways, e. g. resistive, capacitive, with a tee network or a pseudo-resistor [103, 106].

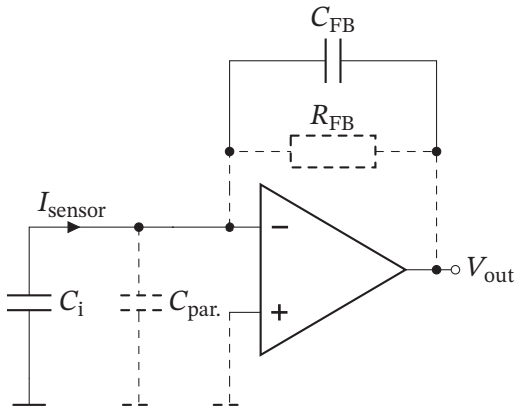

b) Implementation of a resistive TIA with feedback resistor R_{FB}. For stabilization purposes a feedback capacity C_{FB} may be added. The sensor's capacitance is C_i, whereas a parasitic capacitance is denoted by $C_{par.}$. I_{sensor} is the current to be measured.

Figure 4.7: General depiction of a TIA as well as an implementation of a resistive one.

4.2.4 Transimpedance amplifier

A TIA is the circuit of choice used in this thesis. In general a TIA is set up as shown in figure 4.7a. The inputs of the OpAmp are labeled as in_- and in_+. Several choices for the feedback's design exist. One might use pseudo-resistors [112], a tee network, a resistor or a capacitor [103]. We will take a brief look at the use of pseudo-resistors in section 4.4.

Resistive transimpedance amplifier

A resistive TIA is shown in figure 4.7b with a feedback resistor R_{FB}, an (optional) feedback capacitor C_{FB}, as well as the unavoidable parasitic capacitance C_{par}. The overall input capacitance is the parallel combination of C_{par} and the capacitance by the sensor at the input node in_- [103].

The feedback factor β is given by [106, 113]

$$\beta = \frac{1 + 2\pi\nu R_{FB} C_{FB}}{1 + 2\pi\nu R_{FB} (C_i + C_{FB})} \quad , \tag{4.4}$$

where C_i is the overall input capacitance, i. e. the sensor's capacitance as well as the parasitic capacitance. The circuit can be understood by coming back to the concept of the virtual short. As shown in figure 4.5 the OpAmp "tries" to satisfy $\Delta V = 0$. As the input impedance of the OpAmp is large, this can only be fulfilled as long as the output of the OpAmp drives a current through R_FB large enough to compensate for the sensor's current I_sensor [106]. At the same time, this decouples the current to be measured from the current provided at the TIA's output, which is then only limited by the maximum output voltage of the OpAmp. When designing the TIA, there is always a tradeoff between sensitivity and maximum input current. In general the higher the feedback resistance the higher the sensitivity.

Consider the feedback capacitance C_FB next. Visualize figure 4.7b in the direction of the feedback path, without the feedback capacitance C_FB and neglecting the parasitic capacitance. Here the feedback resistor R_FB and the capacitance C_i form a low-pass filter, thus shifting the phase of the output signal depending on the input frequency [106]. Any other capacitance, such as the input capacitance, would contribute as well. This at some point will be constructively, and if damping is not sufficient due to a badly chosen feedback capacitance that circuit starts oscillating. Phrased differently the input capacitance is responsible for an additional pole in the system, which reduces the bandwidth [113]. The resonance frequency or the pole of this circuit is at $\nu = 1/2\pi R_\mathrm{FB} C_i$ [72]. The feedback capacitor C_FB introduces a zero in the transfer function, which enhances the bandwidth [106] and increases the phase margin [113]. A resistive TIA appears to be a sensible choice for the current state of the experiment, as the input signals provided are either direct current (DC) or at very low frequencies. The input current can simply be calculated from the output current by using Ohm's law with the feedback resistor.

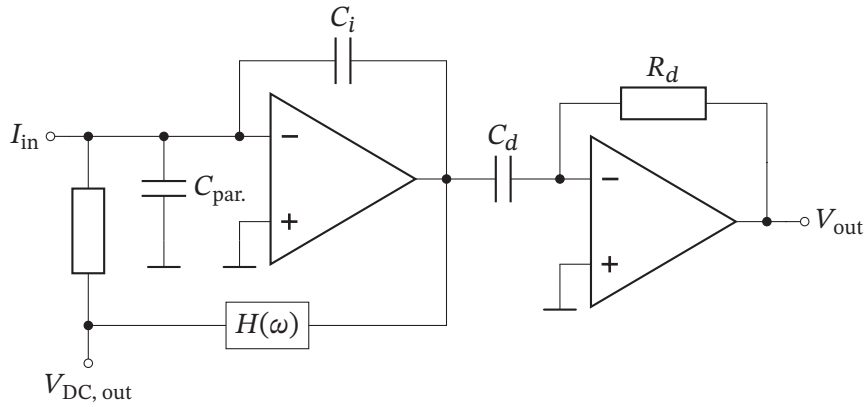

Figure 4.8: Capacitive TIA circuit as seen in [104]. The first OpAmp serves as an integrator, whereas the second differentiates again. The function $H(\omega)$ is a placeholder for a filter network.

Capacitive transimpedance amplifier

Following along [103] a resistive TIA becomes more and more difficult to realize the larger the feedback resistance becomes, especially when thinking about integrated circuits (ICs). This is mainly due to the material and area needed in that case when implementing in complementary metal–oxide–semiconductor (CMOS) structure. A larger area would not only increase the cost in manufacturing, but additionally introduce high parasitic capacities. Instead, a capacitive TIA can be used.

Taken from [104] a basic circuit can be seen in figure 4.8. It is based on an integrator (first OpAmp) and then differentiator (second OpAmp) structure. The differentiator ensures an overall linear behavior while not contributing much to the noise [103]. The transfer function can be written as [104]:

$$\frac{V_{\text{out}}}{I_{\text{in}}} = \frac{C_d}{C_i} R_d \tag{4.5}$$

The shown DC–feedback path compensates the charging of the capacitance, however, this also decreases the measurement time [103]. This structure has the advantage of providing more choices in shaping the overall response [104], while having low noise and high sensitivity [103]. However, saturation occurs for low-frequency and DC input, making it, at this point of the project, not the most suitable circuit.

4.2.5 Circuit realizations

Within this work several PCBs featuring different circuits were developed and used. All of them were developed and designed in cooperation with the IIS. Two of the designs proved to be most successful, and were used for the results shown in this work. These are introduced.

Version 1

The first version used, features a simple TIA circuit as shown in figure 4.9a. We use the ADA4817 as OpAmp. According to the datasheet [114] it features an open-loop gain of 65 dB, a low input capacitance of 1.3 pF, a 3 dB–bandwidth of 1050 GHz, and an input offset of about 2 mV. This makes it well-suited for the application. According to the simulated Bode plot in figure 4.9b the bandwidth of the circuit is low as long as the feedback capacity of $C_{\mathrm{FB}} = 18\,\mathrm{pF}$ is part of the circuit. During the time this circuit was used this was not problematic, since all involved measurement parameters were below this value. We will see throughout this work that the feedback capacity introduced an asymmetry in the measurement signal, and decreased the measurement time significantly. For comparison, the Bode plot shows the curve without feedback capacity as well. The bandwidth is then increased.

The PCB itself has two-layers. The bottom layer provides the electrode with dimensions of $w \times l = 10\,\mathrm{mm} \times 14\,\mathrm{mm}$ and points inside the measurement cell. The size of the electrode is discussed in section 4.3. A via connects the bottom electrode with the top layer. The top layer includes the TIA–circuit of figure 4.9a as well as voltage regulators generating the supply voltages (−5 V and 5 V) on the PCB itself to assure stable operation. The components used are LT3094 and LT3095. The PCB itself is then supplied with ±7 V externally via a three-pin MOLEX connector. The output signal is provided via an U.FL-connector. A picture of the PCB is shown in figure 4.10. The counterpart of the first cell is realized with the same PCB, however, only the electrode is connected. Unused signal space is covered by a ground plane.

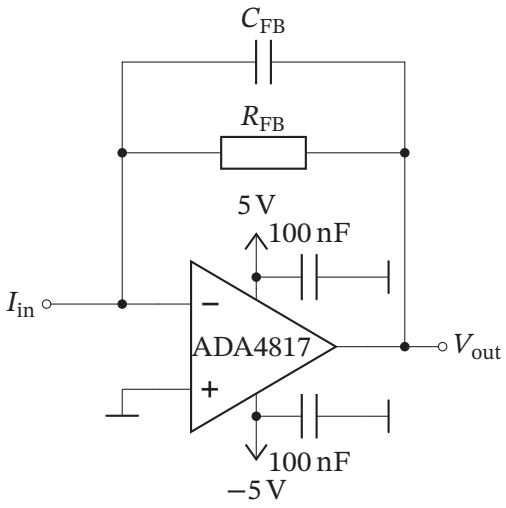

a) This circuit was at first used with a resistance of $R_{FB} = 470\,M\Omega$ and an additional capacitance of $C_{FB} = 18\,pF$. The capacitance was chosen within the lab such, that any possible oscillations in the circuit were suppressed.

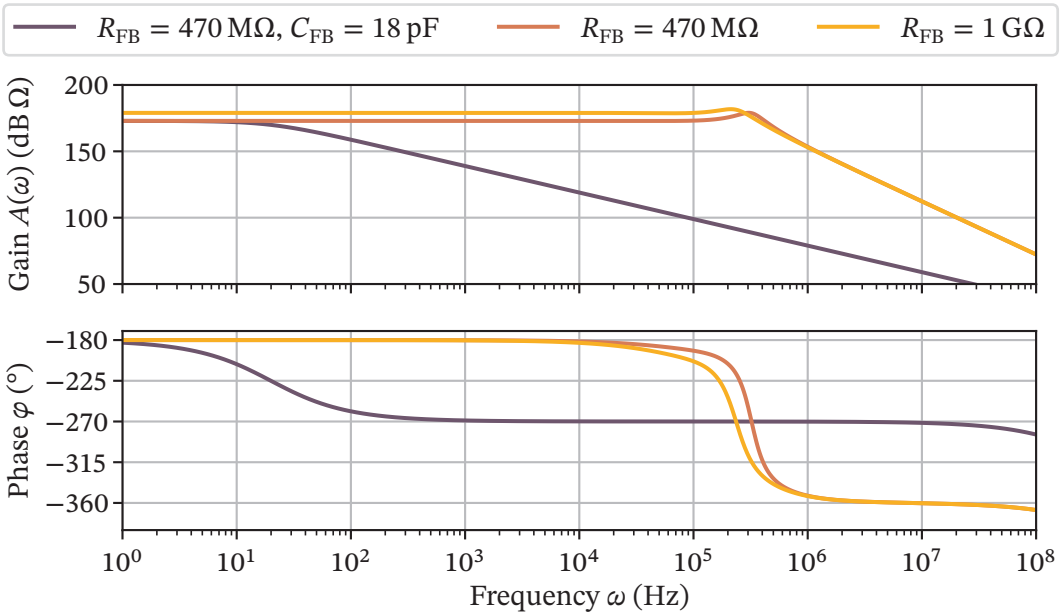

b) Bode plot of the circuit above simulated with LTSpice [109]. If the feedback capacitance C_{FB} is included, the bandwidth is highly limited. Without it, the circuit shows peaking for high frequencies. At a later point higher amplification was necessary, and thus the feedback resistance changed from 470 MΩ to 1 GΩ.

Figure 4.9: Electronic circuit and Bode plot of the first successful readout circuit. This circuit will be called *version 1* throughout this work.

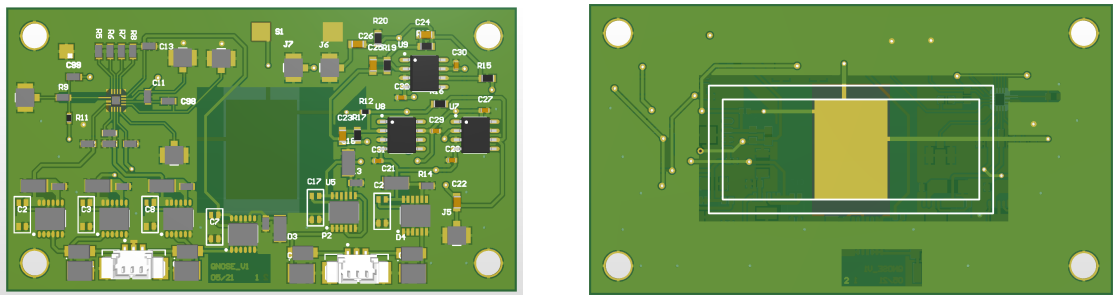

Figure 4.10: Pictures of the PCB of circuit version 1. The circuit design has been done in Altium Designer [115]. Note that the left half of the top plane is designated for another circuit, yet in this picture not assembled and also not used in this work. The right picture shows the bottom plane pointing into the cell. The white lines are the cell frame with 35 mm × 14 mm, and the electrode has dimensions of 10 mm × 14 mm.

Version 2

While the first circuit yielded valuable results as will be discussed in subsection 4.2.6, it also has a couple of issues especially when used to make high precision Stark measurements as will be presented in subsection 5.3.4, or pressure shift measurements as will be shown in subsection 5.4.5. Since the input capacity of the cell's electrodes is, when a plate capacitor is assumed, only on the order of several fF, an input capacitance of 1.3 pF of the OpAmp is comparably large. The larger the parasitic capacitance, the slower the measurement has to be performed, as the capacitance always needs to be charged first. For the Stark effect the inhomogeinity of the electric field is the largest problem, and the result of the quite small electrode of the previous PCB.

These issues were tackled in version 2. The idea is to enlarge the electrode on the bottom plane, while keeping the area connected to the TIA small. A large area connected to the TIA's input would otherwise behave like an antenna detecting noise of surrounding sources. The maximum area coverable by the electrode is the full cell frame, about $w \times l = 35\,\text{mm} \times 14\,\text{mm}$. This area was divided in three subareas. The most inner area is directly above the laser beam, and connected to the TIA's input node. It has dimensions of $w \times l = 10\,\text{mm} \times 14\,\text{mm}$. This means the detection region is the same as with the first circuit. This area is surrounded by a so-called guard ring, which is actively held on the same potential as the input by an additional OpAmp, thus reducing leakage current. The remaining area is the exposed ground plane, as the TIA's input node is a virtual ground. The electronics itself are again placed on the top plane, and the supply voltages are again generated by LT3095 and LT3094 voltage regulators on the PCB itself, externally a three-pin MOLEX connector is used, and the output voltage is sent to an U.FL connector. A picture of the PCB is shown in

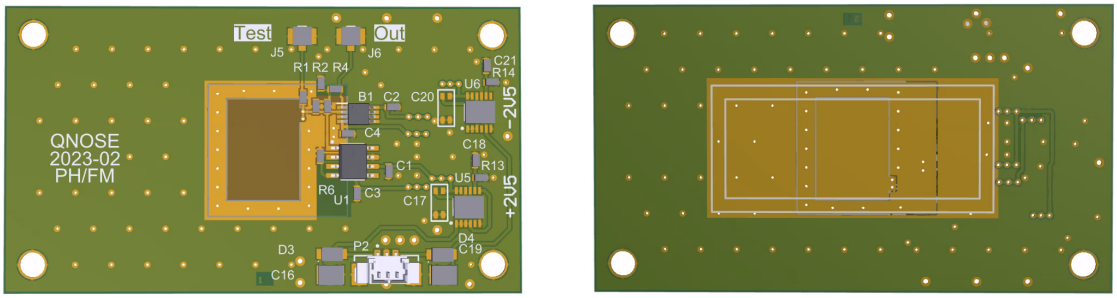

Figure 4.11: Picture of the PCB of circuit version 2 as designed in Altium Designer [115]. The white lines are the cell frame, which is identical to the one of version 1 with 35 mm × 14 mm in dimension. The bottom plane consists of an additional guard ring and exposed ground plane, thus enlarging the overall electrode area while keeping the area connected to the TIA small and at the same dimension as in version 1 in figure 4.10.

figure 4.11. The used electrical circuit is shown in figure 4.12a. The OpAmp LTC6269 serves as a TIA, whereas the OpAmp LMP7721 keeps the guard ring on the same potential as the TIA's input node. As such the LMP7721 is configured as a buffer decoupling the guard ring from the input tee network. A Bode plot of this circuit is shown in figure 4.12b. While the Bode plot shows peaking for high frequencies, they are not of relevance for the experiment covered in this work. The most important specification of the guard ring's OpAmp is its offset voltage, which is 150 µV [116], as any offset makes leakage currents possible again. The TIA–OpAmp LTC6269 has a very small input capacitance of only 450 fF, thus improving by a factor of more than two in comparison to the OpAmp used in the previous circuit. Additionally, the input voltage offset is about 200 µV. Finally, a GBW of 500 MHz is well above what we need [117]. For the amplification a tee network is used. This has the advantage that it significantly reduces the offset error [106]. As long as $R_1 \ll R_2 \ll R_3$ holds the needed resistances can be calculated as [106]

$$R_{\text{eff.}} = \left(1 + \frac{R_2}{R_3}\right) R_1 \quad , \tag{4.6}$$

where $R_{\text{eff.}}$ is the effective resistance.

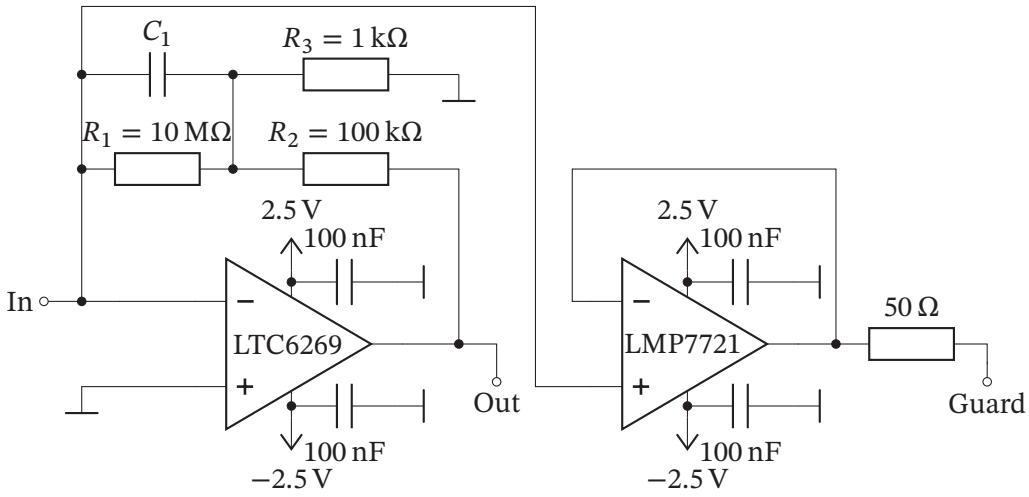

a) The OpAmp LTC6269 is responsible for the amplification, whereas the OpAmp LMP7721 keeps the guard ring on the same potential as the input node of the amplification OpAmp. The tee network provides a virtual feedback resistance of roughly 1 GΩ. The at this point not used capacitance C_1 could be used, if stability issues arise in future versions.

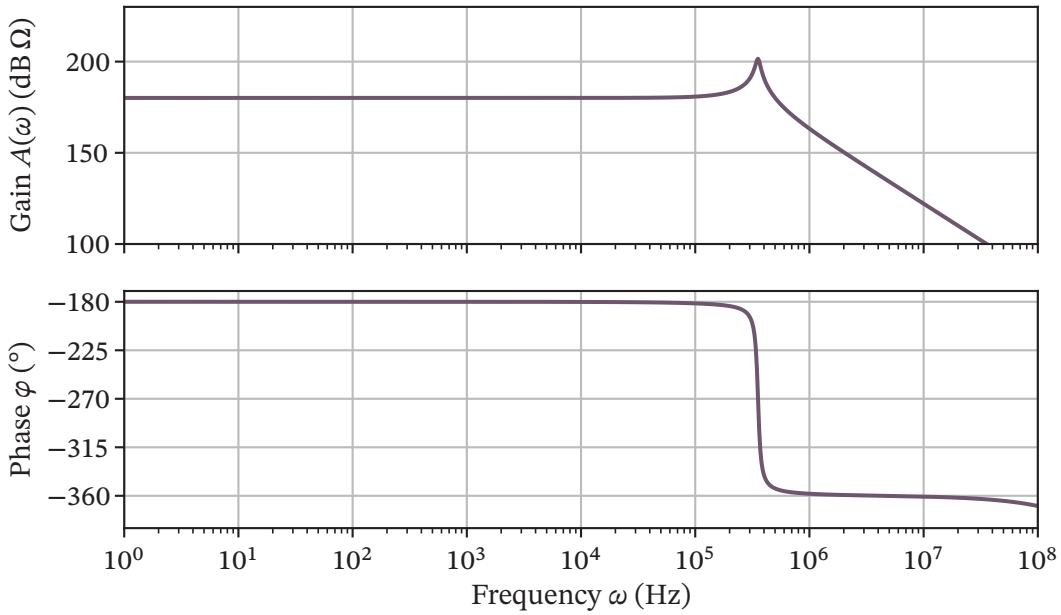

b) Bode plot of the most recent circuit, showing a high amplification and peaking only for very high frequencies, which are not of relevance anymore. The Bode plot was simulated with LTspice [109].

Figure 4.12: Electrical circuit and Bode plot of *version 2*. An additional guard ring improves the PCB.

4.2.6 The size of the electrode area

Let us consider the electrode area again. A suitable electrode size can be estimated by considering the travel distance $s_\perp$ of the charges perpendicular to the electric field. The velocity distribution $f(v)$ of all particles follows the Boltzmann statistic at temperature T [89],

$$f(v)\mathrm{d}v = \sqrt{\frac{m}{2\pi k_\mathrm{B} T}} \exp\left[-\frac{mv^2}{2k_\mathrm{B} T}\right] \quad , \tag{4.7}$$

where m is the particles' mass and k_B is the Boltzmann constant. As seen in section 3.4 the mean velocity $\bar{v}$ [82] for NO can be calculated to

$$\bar{v}_\mathrm{NO} = \sqrt{\frac{8k_\mathrm{B} T}{\pi \cdot m}} \approx 450\,\frac{\mathrm{m}}{\mathrm{s}} \quad , \tag{4.8}$$

where $m = 30\,\mathrm{u}$ and $T = 293\,\mathrm{K}$ were used. For a linear electric field $\boldsymbol{F}$ the force would be $e\boldsymbol{F}$ and simple relations from classical mechanics yield

$$s_\perp = v_\perp d\sqrt{\frac{m}{e \cdot V}} \quad , \tag{4.9}$$

where d is the electrode distance of an ideal plate capacitor and V is the applied voltage. If we use $v_\perp = \bar{v}$, $d = 20\,\mathrm{mm}$ equation (4.9) yields about 7.1 mm for ions. This means that we loose some of the free charges, and the result becomes worse when considering the tail of equation (4.7). At e. g. $v = 1000\,\mathrm{m\,s^{-1}}$ we have $s_\perp = 15.8\,\mathrm{mm}$. On the other hand a larger electrode would have increased noise due to an antenna–like behavior. The new cell, which will be used in chapter 5, has electrodes at $d = 8.4\,\mathrm{mm}$ apart. The same calculation then yields for $v = 1000\,\mathrm{m\,s^{-1}}$ $s_\perp = 6.6\,\mathrm{mm}$, i. e. considerably fewer particles are lost for detection.

4.3 Characteristics

The main variable experimental parameters are the electric field, the intensities of the laser beams and the gas pressure. These parameters were analyzed with a cell featuring circuit version 1, see subsection 4.2.5. All transitions necessary to excite NO to a Rydberg state can be detected electronically. This was shown in a Master's thesis, which also demonstrated, that we can detect the second and final transition solely electronically [98].

4.3.1 Measurement parameters

A cell with circuit version 1 with a resistance of $R_{\mathrm{TIA}} = 470\,\mathrm{M\Omega}$ including a feedback capacity of 18 pF was used. The electrodes were 2 cm apart. As gas, pure NO was used. The Rydberg transition was driven with the diode laser plus TA system, see figure 3.1c. For each transition the intensity of the laser beam, the electric field and the pressure were swept while keeping the other parameters constant. For the analyzation of the upper transitions the lower transition lasers were kept locked. The laser of the analyzed transition was scanned around the resonance. In total, we produced 9 datasets, where each dataset consists of several scans on the analyzed transition for each step in power, pressure or field. The full excitation path has been

$$n(N^+) \leftarrow \mathrm{H}\,{}^2\Sigma^+ \xleftarrow{\mathrm{R}_{11}(4.5)} \mathrm{A}\,{}^2\Sigma^+ \xleftarrow{\mathrm{P}_{12}(5.5)} \mathrm{X}\,{}^2\Pi_{3/2} \quad .$$

The Rydberg state has most likely been 42(5), though at this point of the project a proper understanding on the accessible Rydberg states was not established. In chapter 5 the different branches and wavelengths will be linked to accessible Rydberg states. Here, the exact Rydberg state itself is not of importance. All lasers involved in a measurement were stabilized in power. The signals recorded per measurement were the direct output of the TIA and the transfer-cavity's transmission signal of the scanned laser. The $1/e^2$–beam waists w of the individual lasers close to the cell were:

A ← X (226 nm):	$w_x \approx 1420\,\mu\mathrm{m}$	$w_y \approx 1700\,\mu\mathrm{m}$	$\overline{w} \approx 1560\,\mu\mathrm{m}$
H ← A (540 nm):	$w_x \approx 370\,\mu\mathrm{m}$	$w_y \approx 580\,\mu\mathrm{m}$	$\overline{w} \approx 475\,\mu\mathrm{m}$
$n(N^+)$ ← H (835 nm):	$w_x \approx 480\,\mu\mathrm{m}$	$w_y \approx 290\,\mu\mathrm{m}$	$\overline{w} \approx 385\,\mu\mathrm{m}$

We measured the waists with a Shack–Hartmann sensor. To calculate the intensities the mean value $\overline{w}$ and equation (3.16) are used. The intensities of all individual measurements are listed in table 4.1.

Table 4.1: Intensities of the laser beams for all measurements introduced in this section. The first column gives the scanned transition. The second column denotes which intensity belongs to which laser. The other columns correspond to the swept parameter. These are rounded values, and the used powermeter has an uncertainty of 7 % for the first, an uncertainty of 5 % for the second and an uncertainty of 3 % in the wavelength range of the final transition.

Scanned transition	Laser	Intensity sweep ($\mathrm{mW\,mm^{-2}}$)	Field sweep ($\mathrm{mW\,mm^{-2}}$)	Pressure sweep ($\mathrm{mW\,mm^{-2}}$)
A ← X	A ← X	—	2.0	2.4
H ← A	A ← X	2.4	2.2	2.4
	H ← A	—	1250	1280
$n(N^+)$ ← H	A ← X	1.8	2.2	1.8
	H ← A	1250	1250	1250
	$n(N^+)$ ← H	—	560	580

4.3.2 Evaluation

Each measurement is evaluated in the following way:

1. Every dataset consists of several single transitions.
2. For every single transition the traces are cut by eye to contain only the feature roughly at its center.
3. For each single scan the frequency axis is acquired by translating the cavity peak position in time to a frequency axis by using the known FSR of the respective cavity. To fit the positions a polynomial function of second order is used.
4. By dividing the voltage signal with R_{TIA} it is converted to a current.
5. We fit the transition signal.
   a) For the UV transition we use a Gaussian fit, as the broadening is mostly due to Doppler broadening (see subsection 3.4.2)
   b) For the second and third transition we use a Voigt function. The wavevector mismatch as introduced in subsection 3.4.2 justifies this.
   c) The fit function is adjusted such that it contains an exponential decay for asymmetry reasons, as will be discussed next.
6. Width and amplitude are extracted from the fit.
7. For an individual dataset all acquired widths and amplitudes are plotted against the swept parameters, i. e. pressure, field or intensity.

Asymmetric lineshapes

The transition signal shows an asymmetric lineshape for all transitions, and the asymmetry is especially dominant for the second transition. Exemplary single transition signals for the sweep of the electric field are shown in figure 4.13.

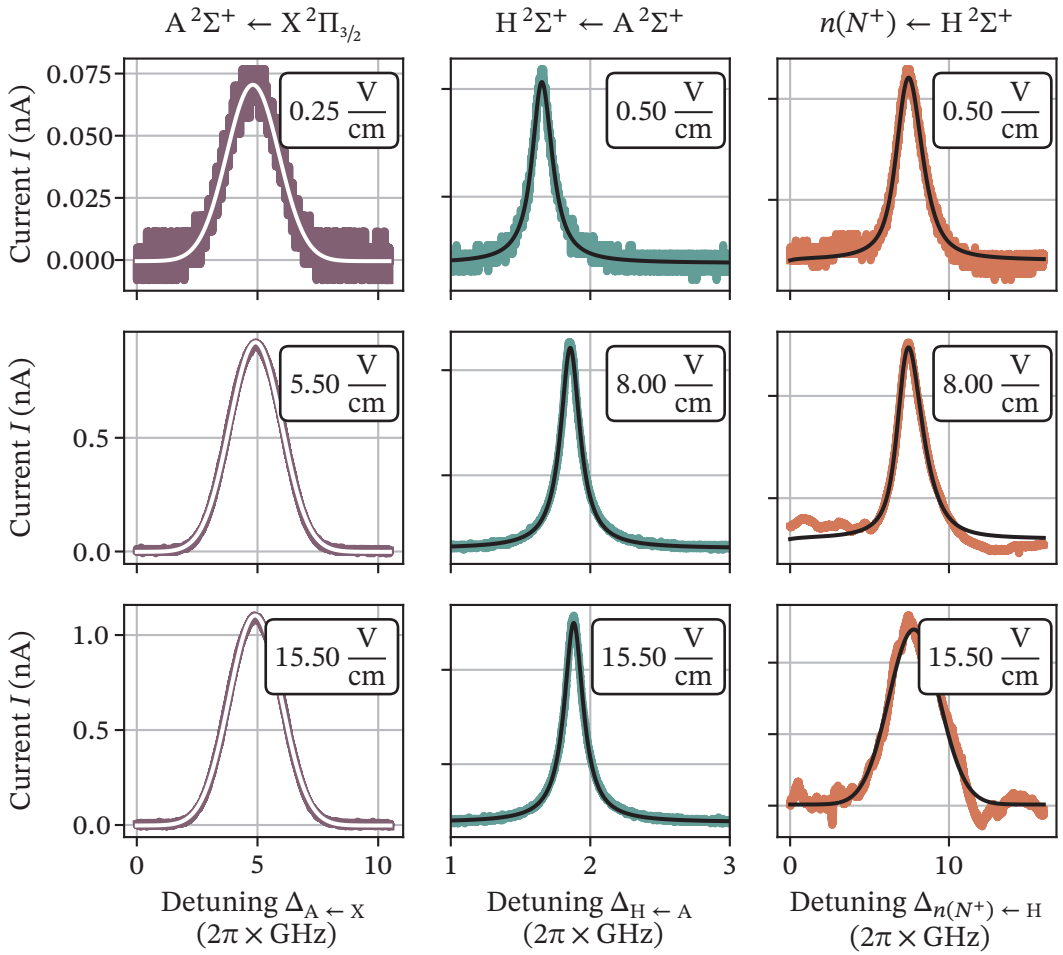

Figure 4.13: Exemplary individual measurement traces for the analyzation of all transitions being subject to different electric fields. For the H $^2\Sigma^+ \leftarrow$ A $^2\Sigma^+$ and $n(N^+) \leftarrow$ H $^2\Sigma^+$ transition the lower lasers were locked. Each subplot shows the fit additionally. The discussed asymmetry is especially visible for the H $^2\Sigma^+ \leftarrow$ A $^2\Sigma^+$ and $n(N^+) \leftarrow$ H $^2\Sigma^+$ transition.

For this reason the fit function was adjusted with a convolution of an exponential decay for half of the already cut dataset:

$$f_{\text{fit}}(\omega) = g(\omega) * h_{\text{Voigt, Gaussian}}(\omega) \tag{4.10a}$$

$$g(\omega) = \begin{cases} 0 & \text{if } \omega < \text{size of array} \\ \exp\left[-\omega/\kappa\right] & \text{else} \end{cases} \tag{4.10b}$$

The exponential decay has a decay parameter κ and is only motivated empirically. For the Gaussian and Voigt function $h(\omega)$ refer to subsection 3.4.2. We investigated the asymmetry of the line after the measurements were complete. No dependence on the scan direction of the laser was visible, suggesting that it is not an effect by the molecule. Instead, after excluding laser issues, any time constants present have to be taken into account. These are on the one hand the flight time of the ions, as well as the rise time of the circuit. The rise time of the used (old) circuit has been measured to be about 12.7 ms [75]. The flight time was analyzed as part of a Master's thesis [75] as well. Due to their mass NO^+ ions are slower than electrons. The acceleration a of the ions would be [75]

$$a = \frac{e \cdot V}{d \cdot m} \quad , \tag{4.11}$$

with e being the elementary charge, V the voltage, d the electrode distance and m the mass. With a voltage of $V = 10\,\text{V}$ applied, the flight time $t = \sqrt{2d/a} \approx 5\,\mu\text{s}$, which is negligible when compared to a measured rise- and fall time of about 12.7 ms.

As will be seen in section 5.3 and section 5.4 the asymmetry is much reduced till not visible if the newly designed cell (see figure 4.2) is used. This can be understood such, that any capacitance in the readout circuit always needs to be charged first. The newly designed circuit lacks any specifically introduced feedback capacitance.

It is plausible, that the $\text{H}\,^2\Sigma^+ \leftarrow \text{A}\,^2\Sigma^+$ and $n(N^+) \leftarrow \text{H}\,^2\Sigma^+$ scans show a more asymmetric lineshape than the $\text{A}\,^2\Sigma^+ \leftarrow \text{X}\,^2\Pi_{3/2}$ transition, as the narrower linewidth causes a steeper slope to follow, when scanning the same range. It has been confirmed experimentally, that the main cause is the feedback capacitance of 18 pF, as the same cell was briefly used with the capacitance removed. However, noise issues were significant, which led to the development of a new cell and circuit. A thorough discussion follows in chapter 5.

The experimental results shown here are still of great value, as they allow finding operational sweet spots for the overall project of a trace-gas sensor.

4.3.3 Results and discussion

This section gives results which are applicable for the new cell as well. A proper signal analysis in terms of signal–to–noise ratio (SNR) is given in section 5.3 for the new cell involving a lock–in amplifier, and is not discussed here.

Intensity sweep

In an intensity sweep the electric field and the pressure are set to a constant value. Each transition is scanned around its resonance, and a trace recorded. After a single iteration the intensity of the transition's laser is adjusted, and the process repeated. This is done for all three transitions.

The results are shown in figure 4.14. The UV transition appears to follow a quadratic relation in amplitude for small intensities, whereas it turns linear for higher intensities. While the reason cannot be nailed down, such a behavior usually indicates a quadratic scaling effect such as Penning–ionization or resonance–enhanced multiphoton ionization (REMPI). Both effects are likely, as we are detecting charges resulting from collisions of Rydberg molecules with other particles. In any case there has to be an effect on the width as well. The Doppler broadened linewidth is expected to be $\gamma_{\text{Doppler}} \approx 2\pi \times 3\,\text{GHz}$, as calculated in section 3.4. For a quadratic behavior the expected width has to be multiplied by $1/\sqrt{2}$, which gives $\gamma_{\text{Doppler, quadratic}} \approx 2\pi \times 2.1\,\text{GHz}$, which is slightly below the shown linewidth. The other two transitions both show a linear behavior in amplitude. A linear behavior is the expected behavior as long as saturation is not reached. Compare this with section 3.4. For all three transitions saturation is not visible. The widths of all transitions oscillate around a constant value. For the ground state transition the signals are hard to fit for low intensities due to a bad SNR. The Rydberg transition is broadened due to the high applied electric field, see figure 4.13 for comparison. This is due to the Stark effect, and will be better understood in section 5.3. In retrospective the high electric field was a non–optimal choice, though the signal was not understood as the resolution was not sufficient. Still, there is no broadening visible, confirming that we are unable to saturate any transition.

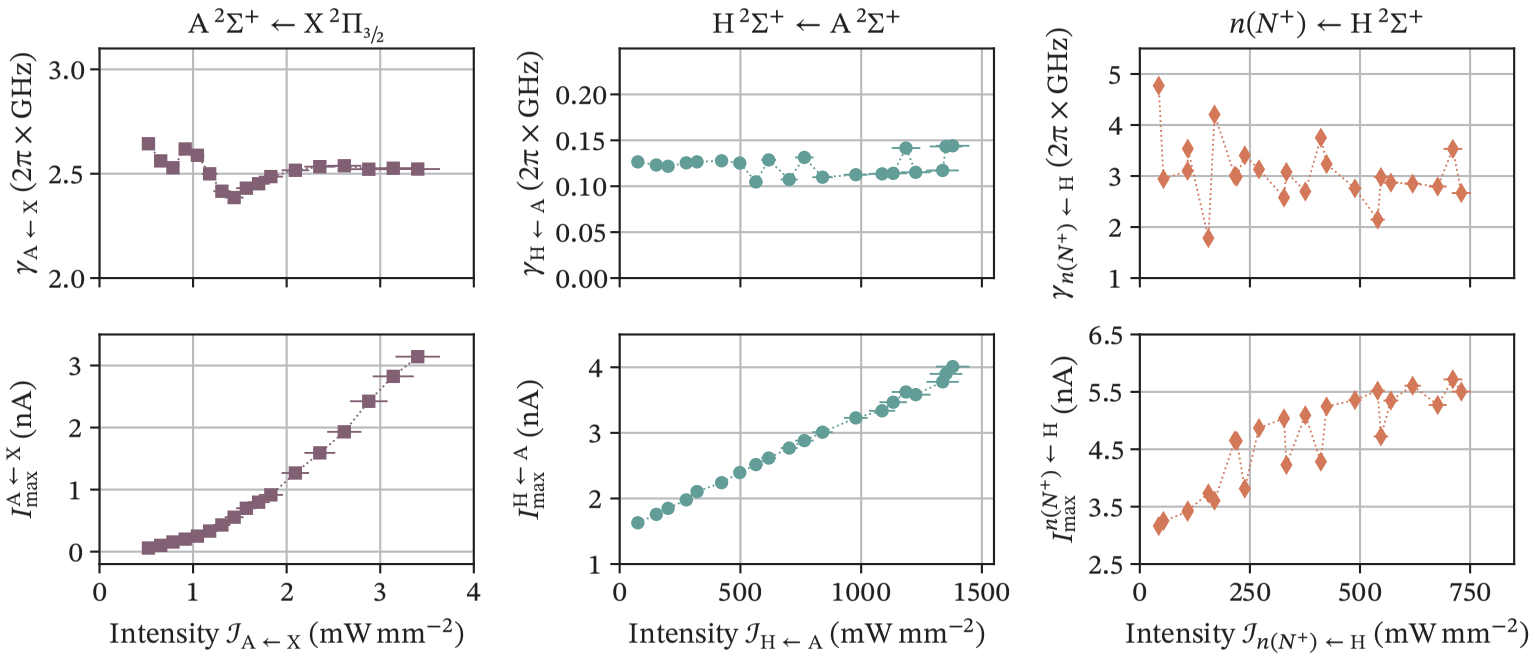

Figure 4.14: Plots of FWHM γ and amplitude I_{max} for all three transitions in dependence of a change in laser intensity. All other laser intensities are listed in table 4.1. The error bar indicates the uncertainty of the used power meter head. We obtain amplitude and width from an asymmetric fit, see equation (4.10). The intensities of the individual measurements are specified in table 4.1. The pressure, from left to right, was set to 2.10 mbar, 2.16 mbar and 2.12 mbar. The electric field was identical for all measurements and set to $16.1\,\mathrm{V\,cm^{-1}}$. The dotted lines are a guide to the eye.

Pressure sweep

For a pressure sweep, we used a constant electric field and constant laser intensities. The pressure was changed incrementally and each transition analyzed. A plot is shown in figure 4.15.

All three transitions show the same behavior for both amplitude and width. The width increases linearly with increasing pressure. This is expected due to collisional broadening, see section 3.4. The amplitude peaks at around 2 mbar and then decreases again. This we can attribute to the free charges not reaching the electrode anymore, as well as the decrease in efficiency due to the collisional broadening. The higher the pressure the less likely it becomes for the charge to reach the electrode, but instead colliding and possibly combining with another particle increases in probability. This ultimately leads to a decrease in amplitude. It clearly shows, that lower pressures are much preferred for the experiment and sensor. In general a pressure on the order of 50 μbar proved to be a good value in terms of SNR and signal quality.

Electric field sweep

For the sweep of the electric field the pressure and the intensities are all kept constant. A plot of the results for each individual transition is shown in figure 4.16. Considering the amplitudes first, the behavior of all three transitions is similar. In the beginning, the amplitude increases rapidly with increasing electric field. At some point there is saturation, and the amplitude is only increasing very slowly. This can be easily understood, since at some point there is nothing to ionize anymore. The width starts to greatly fluctuate for higher fields, especially for the Rydberg transition. This can be attributed to the Stark effect, as the single peak is actually made of individual transitions, which we were not able to resolve with the cell in use back then. In figure 4.13 the increase in field is shown for individual traces, and the baseline of the Rydberg transition starts to oscillate for higher fields. A proper analysis of the Stark effect in NO is given in section 5.3.

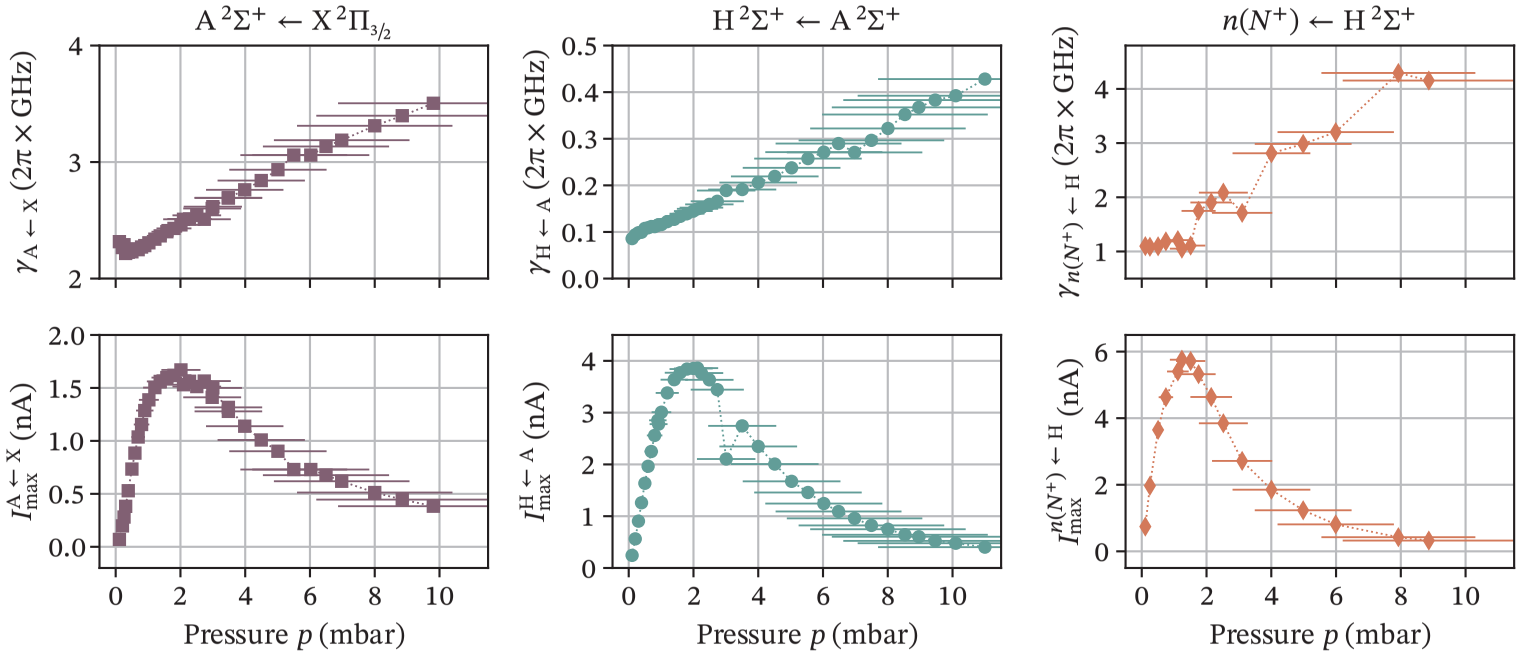

Figure 4.15: This plot shows amplitude I_{max} and FWHM γ for all three transitions, which were extracted from an asymmetric fit to the signal (equation (4.10)). The employed pressure gauges (Pfeiffer PKR 251) have an absolute pressure uncertainty of 30 %, which yields the error bars. Table 4.1 lists the intensities of the individual measurements. For all measurements a constant field of 16.1 V cm^{-1} was applied. The dotted lines are a guide to the eye.

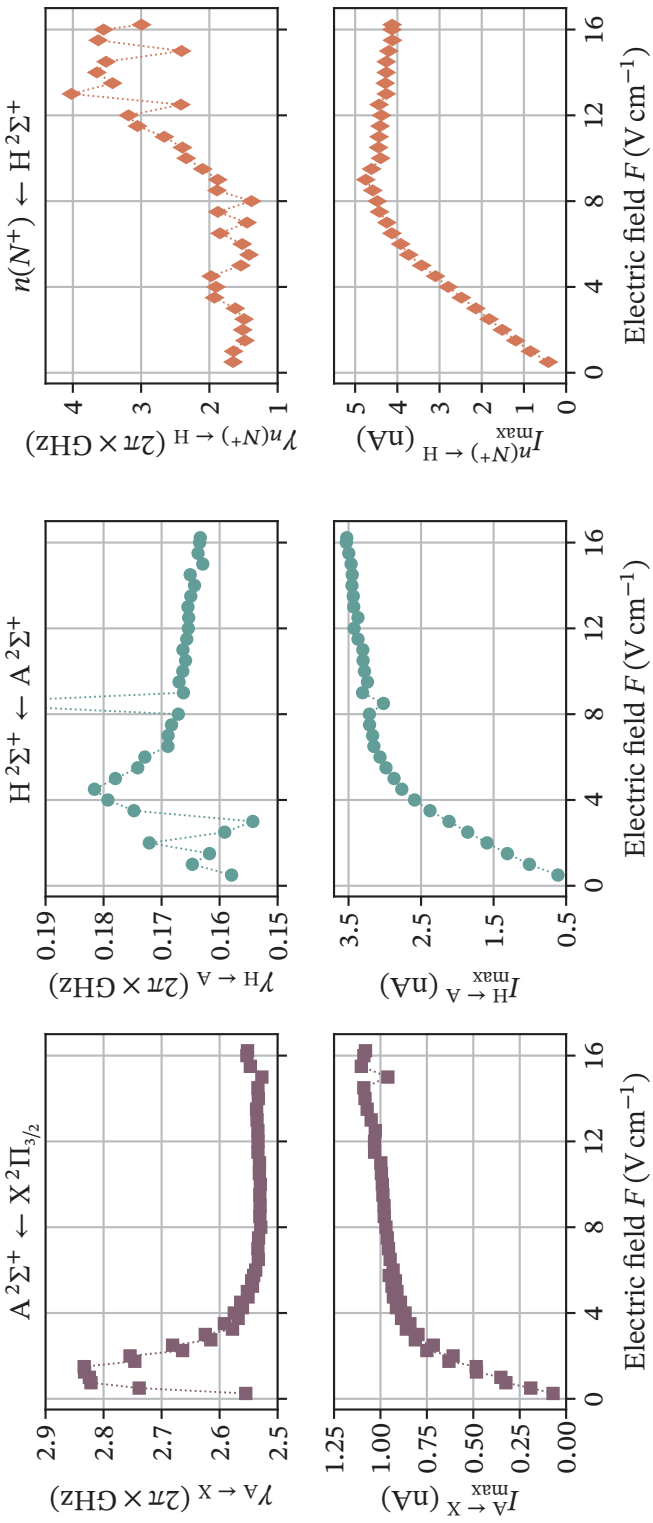

Figure 4.16: This graphic shows the dependence of the electric field on the amplitude $I_{\max}$ and FWHM γ of all three transitions. Amplitude and FWHM were obtained by using a Voigt fit, see equation (4.10). The intensities are listed in table 4.1. This plot has no error bars, as the voltage uncertainty is negligible when compared to the dot size. The constant pressures of the individual measurements are, from left to right, 2.09 mbar, 2.15 mbar and 2.16 mbar. The dotted lines are a guide to the eye.

Combined plot

In figure 4.17 a combined plot of all previously discussed results is shown, which should ease the comparison of the different behaviors. The experiment is not limited by saturation for any transition, i. e. the higher the power, the better the signal. Especially when tuning the $A\,^2\Sigma^+ \leftarrow X\,^2\Pi_{3/2}$ and $H\,^2\Sigma^+ \leftarrow A\,^2\Sigma^+$ lasers to their transition the electric field can be chosen high, as there are no side effects. For the Rydberg state however, the Stark effect has to be considered, which is extensively analyzed in section 5.3. Finally, it is wise to choose a low pressure to not be subject to pressure broadening, and additionally to detect a maximum amount of charges. A good value for the Rydberg transition proved to be on the order of 50 μbar.

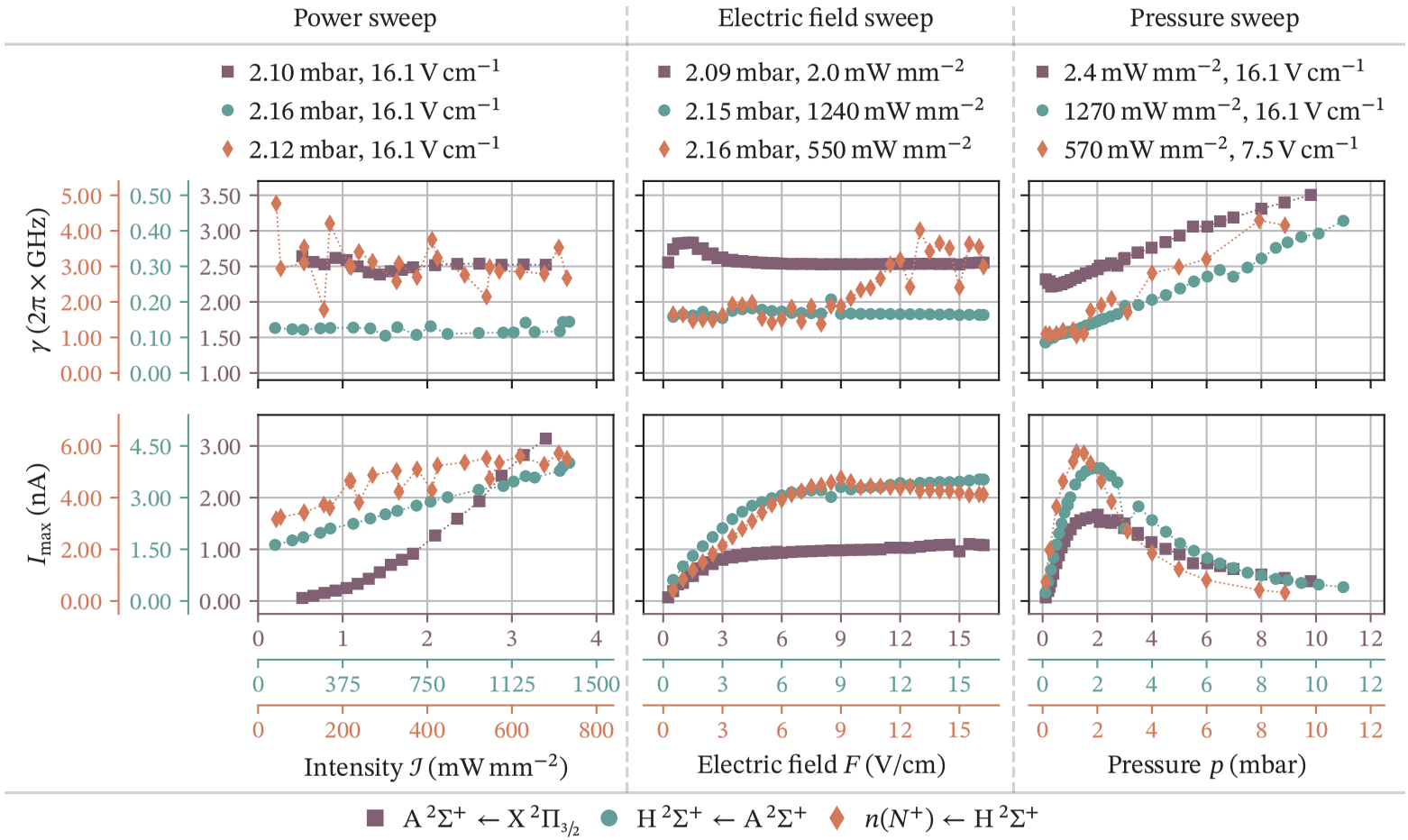

Figure 4.17: Combined plot of figures 4.14 to 4.16 to ease comparison of the behavior. For clarity this plots lacks the error bars of the individual plots. The colored axes correspond to the measurement of the same transition. The legend gives the parameters of the investigated transition. Table 4.1 lists the remaining intensities.

4.4 Future improvements

In this work all electronic components used are off–the–shelf components, though the PCB is self-designed. This has the obvious advantage of easy reproducibility and low manufacturing costs. However, while off–the–shelf products are oftentimes cheap yet still versatile, this comes with the disadvantage of not being able to optimize for the application at hand completely. For example, the old PCB with circuit version 1 showed the asymmetry as discussed, which can be attributed to the used feedback capacitance. On the other hand, this capacitance improved the stability of the bought OpAmp. While the new circuit (version 2) could improve on this, there is still the problem of stray capacities which reduce the overall measurement time. For the new cell the electrodes are $d = 0.84\,\mathrm{cm}$ apart and circuit version 2 is used. The upper electrode is $A = 35\,\mathrm{mm} \times 14\,\mathrm{mm}$ in area. If an ideal plate capacitor is used, the capacitance C_{cell} of the cell is [118]

$$C_{\mathrm{cell}} = \epsilon_0 \frac{A}{d} \approx 516\,\mathrm{fF} \quad . \tag{4.12}$$

This is on the same order as the input capacitance of the used OpAmp LTC6269, $C_{\mathrm{OpAmp}} = 450\,\mathrm{fF}$ [117]. However, the distance d between cells always varies a little bit, and as such the capacitance C_{cell}. The PCB and all electric components contribute with additional parasitic capacities as well. Finally, it is valid to argue that the current cell used in the project is optimized for electric fields, yet not for the introduced trace–gas sensing scheme, where a sensitivity and good SNR is of higher value than a homogeneous electric field.

As such a custom TIA appears to be the way to go for future cell designs. In [112] Denis Djekic presents "a 440 kΩ to 150 GΩ tunable TIA based on multi–element pseudo resistors (MEPRs)", which was developed at the IIS. Here, an application–specific integrated circuit (ASIC) was realized which can only be used as a TIA. This ASIC is realized via CMOS technology. A functionally equivalent circuit is shown in figure 4.18.

The design is made out of two sub–circuits, an alternating current (AC) loop and a DC loop. In the AC loop for low frequencies a typical TIA circuit is present, however, the capacitance C_{FB} dominates for higher frequencies making it behave like a capacitive TIA. Thus, for higher frequencies the signal is integrated, which is reverted using the second stage, an inverting amplifier or, for high frequencies, differentiator. By making sure that $R_1 = R_2$, the overall transimpedance remains R_{AC}. The DC loop separates DC components from the AC signal which are amplified by the transimpedance R_{DC}. According to [112] the noise especially for higher frequencies is reduced by minimizing the input capacities. Additionally, this TIA lacks any

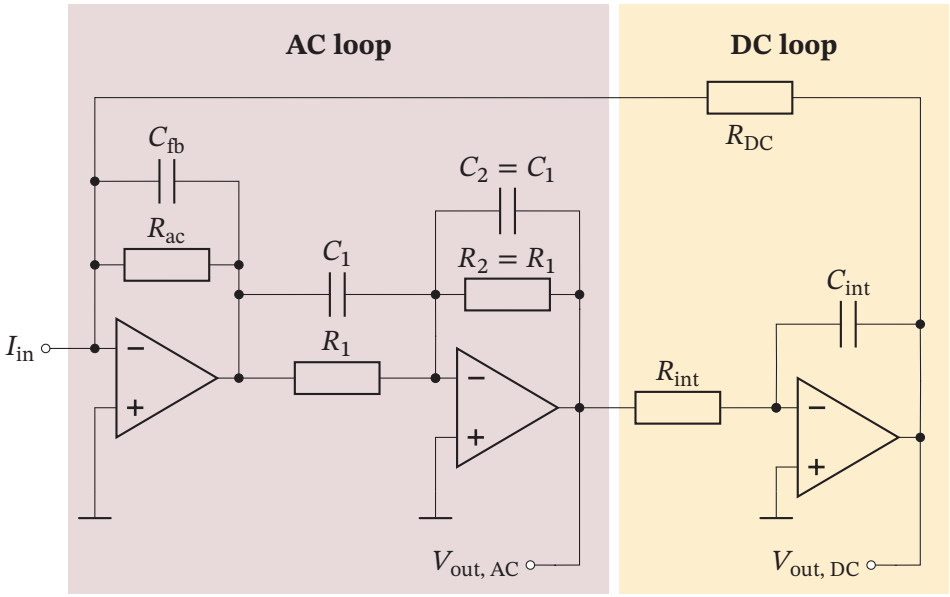

Figure 4.18: Functional equivalent circuit of a TIA as ASIC made by Denis Djekic at the IIS [112]. The AC loop amplifies AC components of the signal, while the DC loop separates DC components. The resistors are realized by MEPRs. More information can be found in the text.

electrostatic discharge (ESD) protection, which reduces the input capacitance further. This makes the signal processing faster and thus makes it advantageous for our application.

All resistors in figure 4.18 are realized by MEPRs, which are explained in detail in [33]. In short, the idea of a MEPR is to replace a conventional resistance by a circuit based on transistors. This makes them robust against variations in temperature but also in the manufacturing process. Additionally, MEPRs allow realizing high resistances. The parasitic capacities introduced by the MEPRs for higher frequencies are compensated by the capacities C_1, C_2 and C_{FB}, which dominate for higher frequencies [112].

The available TIA by the IIS allows focusing on cell geometry improvements rather than focusing on the selection of appropriate off–the–shelf OpAmps. As such its application is certainly promising. At this point a PCB is already fabricated and assembled, and as soon as a new glass cell is available, is ready to use.

5 Rydberg physics in nitric oxide

In this chapter the main results of this work are presented. At the start of the project, there was great uncertainty in terms of accessible Rydberg states $n(N^+)$ by our excitation scheme, and if we can assign the appropriate quantum numbers reliably. The first section shows an experimentally measured Rydberg spectrum over a large wavelength range. It allowed us to verify, that we can assign the principal quantum number n as well as the rotational quantum number of the ionic core N^+ in agreement with the theory.

The other two sections then investigate the Stark effect and collisional broadening and shift in Rydberg states of NO.

5.1 Rydberg spectrum

To gain some understanding on the Rydberg transition the goal was to acquire a Rydberg spectrum, i. e. tune the Rydberg transition laser over a large wavelength range. Accessible are predominantly f–states as introduced in subsection 2.3.3.

5.1.1 Measurement procedure

For the Rydberg transition the Ti:sa system was used, which is sketched in figure 3.1c. The excitation path is

$$n(N^+) \leftarrow \mathrm{H}\,^2\Sigma^+ \xleftarrow{\mathrm{R}_{11}(4.5)} \mathrm{A}\,^2\Sigma^+ \xleftarrow{\mathrm{P}_{12}(5.5)} \mathrm{X}\,^2\Pi_{3/2} \quad ,$$

thus allowing to excite states in the $N^+ = 3$ and $N^+ = 5$ series. The lower transition lasers were locked during the measurement. The important recorded signals are the TIA's output signal and the wavelength of the Rydberg transition according to the wavemeter. The Ti:sa can be scanned by around 30 GHz for a single measurement. For the next range the Ti:sa's parameters had to be adjusted. Over the targeted wavelength range it is impossible to have the same intensity throughout. Nevertheless,

the intensity stayed between 44.4 mW mm^{-2} to 66.5 mW mm^{-2} and was stabilized by an AOM during each single trace. The UV intensity has been around 2.5 mW mm^{-2}, and the green intensity has been around 423.4 mW mm^{-2}. The averaged $1/e^2$ waists of the beams, measured 10 cm before and after the cell, are

$$w_{\mathrm{A}\leftarrow\mathrm{X}} = 942\,\mu\mathrm{m} \quad , \tag{5.1a}$$

$$w_{\mathrm{H}\leftarrow\mathrm{A}} = 643\,\mu\mathrm{m} \quad , \tag{5.1b}$$

$$w_{n(N^+)\leftarrow\mathrm{H}} = 1198\,\mu\mathrm{m} \quad . \tag{5.1c}$$

During the experiment only collimated beams were used. The electrodes are 2 cm apart, the circuit is version 1, and the feedback capacity of 18 pF is in place. In steps the measurement procedure is:

1. Tune and lock the two lower lasers to their transition.
2. Stabilize the green laser in power. The UV power is that low that the power loss at the stabilization optics would be too high. Thus, it is not stabilized.
3. Record the wavelength of the scan center.
4. Scan the Rydberg laser over 30 GHz and record the signal.
5. Adjust the Rydberg laser's wavelength and repeat from step 3. If necessary, adjust the power stabilization parameters of the Rydberg laser.

5.1.2 Evaluation

The measurements are stitched together according to their associated wavelength. Since different measurements have different intensities in the lower transitions as well, the baseline is adjusted such that it is at zero for every measurement. The adjustment is necessary, as the direct TIA output was recorded, and no lock–in amplifier was used. A plot can be found in figure 5.1.

By considering the distance in frequency of individual peaks, which must follow $\propto n^{-2}$, it is possible by eye to differentiate the different Rydberg series, though no principle quantum numbers can be assigned yet. To assign a principle quantum number to a peak two adjacent peaks of the same series are taken, and their frequency difference $\Delta\nu_{\mathrm{peak}}$ calculated based on the wavelength. The Rydberg formula is given in equation (2.32) and the frequency difference of the NO Rydberg states of a single series would thus be

$$\Delta\nu_{\mathrm{theoretical}} = -cR_{\mathrm{NO}}\left[\frac{1}{\left(\eta^{(\mathrm{d})}+1\right)^2} - \frac{1}{\left(\eta^{(\mathrm{d})}\right)^2}\right] \quad , \tag{5.2}$$

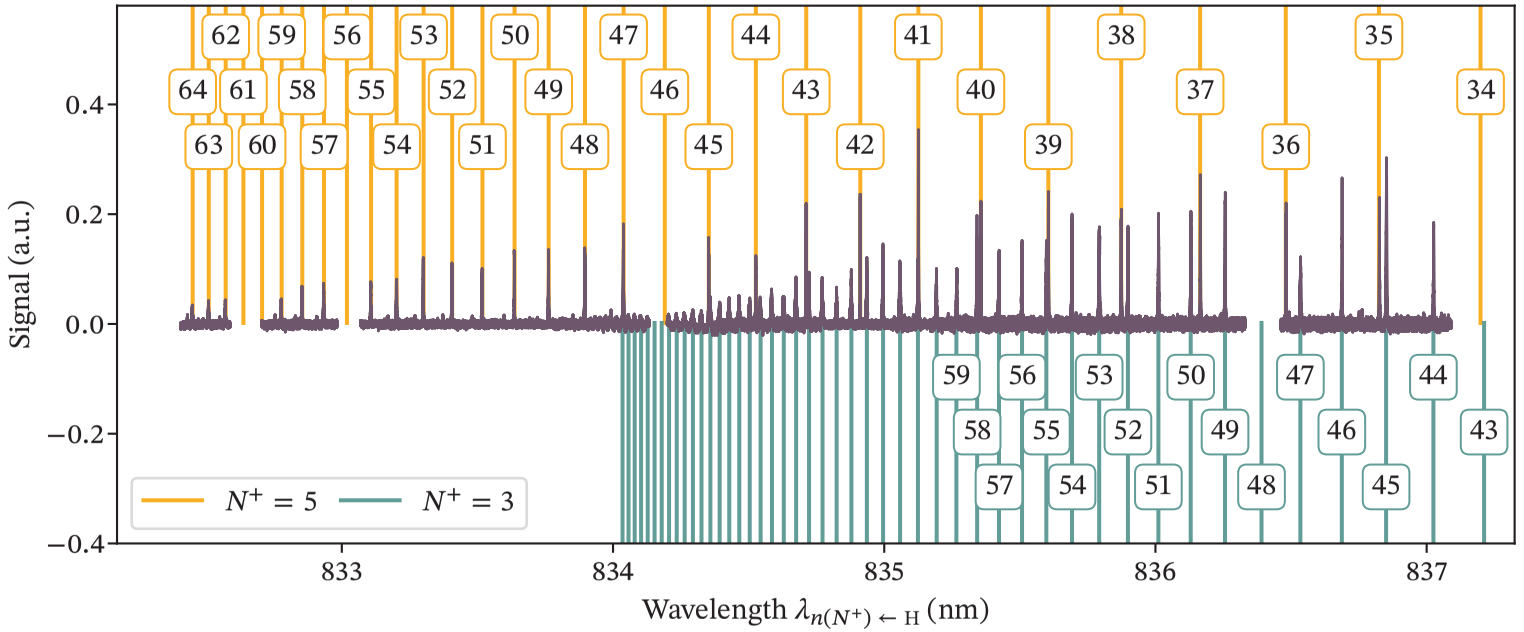

Figure 5.1: Measured Rydberg spectrum of the transition $n(N^+) \leftarrow \mathrm{H}\,^2\Sigma^+$ for the $N^+ = 3$ and $N^+ = 5$ series. Individual scans of the Rydberg transition are stitched together based on the monitoring of the wavemeter. The assignment of the principle quantum number is explained in the text and given in the squared boxes. The signal is in arbitrary units (a.u.), as the Ti:sa's intensity changes significantly over such a large wavelength range. Nevertheless, the amplitudes of the peaks give an indication on the transition strength and are plausible, as the amplitudes tend to increase for lower principle quantum numbers.

and is accurate enough to look at the frequency splitting of the Rydberg states. The Rydberg energy R_{NO} is given in [3] as $R_{\mathrm{NO}} = 109\,735.31\,\mathrm{cm}^{-1}$. As introduced in subsection 2.3.3 the excited Rydberg states should be f–states. The exactness of the frequency readout strongly depends on the linearity of the Ti:sa scan and the wavemeter's readout. To find the principal quantum number n, equation (5.2) has to be solved for n, and the peak difference $\Delta\nu_{\mathrm{peak}}$ is used. Since the quantum defect of f–states (table 2.3) is small, we can simply neglect its contribution.

For the $N^+ = 3$ series the found peak is 56(3), for the $N^+ = 5$ series the found peak is 41(5). These peaks were chosen, as they are easy to identify. The threshold frequency $\nu_{\mathrm{t}} = W_{v^+=0}/h$ of the series can be calculated as

$$\nu_{\mathrm{t}} = \nu_{\mathrm{peak}}(n) - \nu_{\mathrm{Rydberg}}(n) = \nu_{\mathrm{peak}}(n) + c\frac{R_{\mathrm{NO}}}{n^2} \overset{n\to\infty}{\approx} \begin{cases} 359\,863.59\,\mathrm{GHz} & N^+ = 3 \\ 360\,935.82\,\mathrm{GHz} & N^+ = 5 \end{cases} . \tag{5.3}$$

Here, the thresholds are still linked to the wavelengths in figure 5.1, i. e. this is not the absolute threshold but the threshold with respect to the lower transitions. This is visualized in figure 5.2. In equation (2.36) it was shown that the Rydberg series differ by an "offset" in dependence of the rotational quantum number of the ionic core N^+. By using the definition

$$f_{\nu_{\mathrm{t}}}(N^+) \equiv c \cdot \left\{ B^+_{v^+} N^+ (N^+ + 1) - D^+_{v^+} \left[N^+ (N^+ + 1) \right]^2 \right\} \tag{5.4}$$

it is possible to calculate the frequency difference between two series with the constants in section 2.4. The calculation yields

$$\left[f_{\nu_{\mathrm{t}}}(5) - f_{\nu_{\mathrm{t}}}(3) \right]_{\mathrm{theory}} \approx 1072.68\,\mathrm{GHz} \quad . \tag{5.5}$$

The difference for the experimentally determined threshold in equation (5.3) is

$$\left[\nu_{\mathrm{t}}(5) - \nu_{\mathrm{t}}(3) \right]_{\mathrm{experiment}} = 360\,935.82\,\mathrm{GHz} - 359\,863.59\,\mathrm{GHz} = 1072.23\,\mathrm{GHz} \quad , \tag{5.6}$$

which is in very good agreement with equation (5.5) and thus proves, that we are reliably able to label Rydberg states and understand the necessary intermediate transitions.

To determine the wavelength necessary to excite Rydberg states of other N^+–series, these thresholds can be used. The excitation scheme used in this section however only allows reaching of the $N^+ = 3$ and $N^+ = 5$ series. For other series the branches of the first and second excitation have to be changed. As sketched in figure 5.2, the only unknown components are the frequency of the new threshold $\nu_{\mathrm{t},\,2}$ (or the wavelength of the Rydberg transition $\lambda_{n(N^+)\leftarrow \mathrm{H},\,2}$, respectively). The UV transition

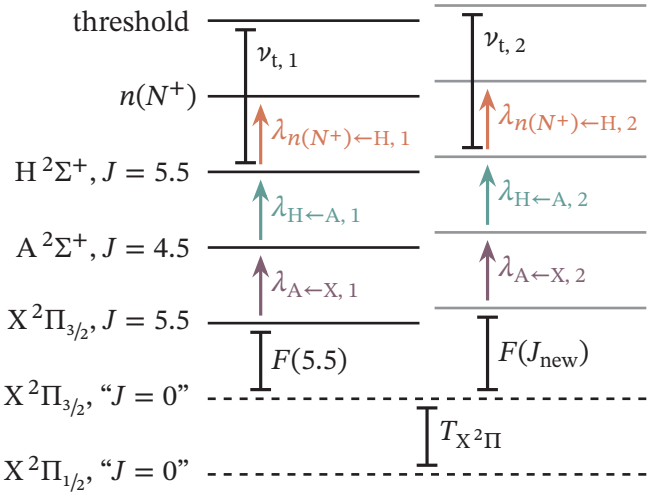

Figure 5.2: Sketch explaining how to calculate another threshold $\nu_{\mathrm{t},2}$ based on the thresholds deduced from $N^+ = 3, 5$. The wavelength $\lambda_{\mathrm{A}\leftarrow\mathrm{X},1}, \lambda_{\mathrm{H}\leftarrow\mathrm{A},1}$, and $\nu_{\mathrm{t},1}$ was calculated by using equation (5.2) and the known wavelength $\lambda_{n(N^+)\leftarrow\mathrm{H},1}$. The rotational energies $F(J)$ can be calculated with equation (2.17), and the wavelength $\lambda_{\mathrm{A}\leftarrow\mathrm{X},2}$ can be taken from PGOPHER [119]. The green wavelength $\lambda_{\mathrm{H}\leftarrow\mathrm{A},2}$ can be estimated with [18], and, after finding the peak, adjusted. Then only $\nu_{\mathrm{t},2}$ is unknown, and therefore the wavelength of all expected Rydberg lines can be calculated.

can be fully simulated, since the necessary constants of the ground state $\mathrm{X}\,^2\Pi$ and the excited state $\mathrm{A}\,^2\Sigma^+$ are known. For simulation the software PGOPHER [119] is used, and the constants are listed in section 2.4. For the $\mathrm{H}\,^2\Sigma^+ \leftarrow \mathrm{A}\,^2\Sigma^+$ transition measurements were performed by Ogi [18], giving a first estimate of the wavelength of the green laser $\lambda_{\mathrm{H}\leftarrow\mathrm{A},2}$. As soon as the new transitions are found the wavelengths can be given with higher precision. As an example, the threshold from equation (5.3) of $N^+ = 5$ is used. Then to calculate a threshold of another N^+–series, where a change of the branches is necessary, one has to calculate:

$$\nu_t\left(N^+_{\mathrm{new}}\right) = \nu_t(5) - f_{\nu_t}\left(N^+_{\mathrm{new}}\right) + f_{\nu_t}(5) - \left[-\frac{c}{\lambda_{\mathrm{H}\leftarrow\mathrm{A},1}} - \frac{c}{\lambda_{\mathrm{A}\leftarrow\mathrm{X},1}} - F(J=5.5) - T_{\mathrm{X}\,^2\Pi} + F(J_{\mathrm{new}}) + \frac{c}{\lambda_{\mathrm{H}\leftarrow\mathrm{A},2}} + \frac{c}{\lambda_{\mathrm{A}\leftarrow\mathrm{XUV},2}}\right] \tag{5.7}$$

The rotational splitting of the ground state $F(J)$ can be calculated as in equation (2.14). The splitting between $\mathrm{X}\,^2\Pi_{1/2}$ and $\mathrm{X}\,^2\Pi_{3/2}$ is denoted by $T_{\mathrm{X}\,^2\Pi}$, and is for example given in [50] and only needed, if the electronic configuration (i. e. Ω) of the ground state is changed.

5.2 Common principles

In section 5.3 Stark maps and in section 5.4 the shift of spectroscopic lines of NO Rydberg states will be presented. For these measurements basic parameters and evaluation methods were the same. These are introduced here.

5.2.1 Cell

The cell used has electrodes 0.84 cm apart, the enlarged electrode area and circuit version 2. This cell is named “new or current cell”. This cell is optimized for the application of a homogeneous electric field as we will see in section 5.3. Pictures can be found in figure 4.2. The only exception is measurement “A” in section 5.3, which is clearly indicated, as this measurement nicely shows the difference between old and new cell.

5.2.2 Transition wavelengths

As introduced in the previous section the knowledge of the ionization threshold allows calculating the Rydberg wavelengths $\lambda_{n(N^+)\leftarrow \mathrm{H}}$. The different wavelengths used to excite different N^+–series are given in table 5.1. Note that here the measured wavelengths are given, i. e. the readout of the wavemeter and not the calculated ones.

5.2.3 Lock–in amplifier

For all presented measurements a lock–in amplifier has been used. The model is “Stanford Research Systems SR830”. The modulated transition is the $\mathrm{H}\,^2\Sigma^+ \leftarrow \mathrm{A}\,^2\Sigma^+$, which is realized via an AOM on the respective laser. This has practical reasons as in principle the $n(N^+) \leftarrow \mathrm{H}\,^2\Sigma^+$–laser could be modulated as well. However, the Rydberg laser is the one scanned in all measurements, leading to higher demands on the circuit to both stabilize the laser in power and modulating the signal itself. The practicability of using a dual–lock–in technique as well as using a lock–in referenced by the modulation of the second or final transition has been analyzed in the scope of a Bachelor’s thesis [120], and the main insights are briefly summarized here.

Things to consider are the rise time τ_{TIA} of the TIA, the integration time of the lock–in amplifier, the scan time of the Rydberg laser, and the modulation frequency. Note

Table 5.1: Wavelengths and branches used to access different N^+ Rydberg series. These are the measured wavelengths after locking the laser. Note, that we only measure the fundamental wavelength of the respective laser. The wavelength the laser was tuned to before knowing the exact wavelength has been simulated with PGOPHER [119] for $A\,^2\Sigma^+ \leftarrow X\,^2\Pi_{3/2}$ with constants taken from [63] and extracted from [18] for $H\,^2\Sigma^+ \leftarrow A\,^2\Sigma^+$. The wavemeter is a HighFinesse WS-6, which has an accuracy of 600 MHz and yields the denoted uncertainties. The wavelengths given are the wavemeter's readout.

	$A\,^2\Sigma^+ \leftarrow X\,^2\Pi_{3/2}$		$H\,^2\Sigma^+ \leftarrow A\,^2\Sigma^+$	
N^+	branch	fundamental wavelength	branch	fundamental wavelength
0, 2	$P_{12}(2.5)$	907.6578(16) nm	$R_{11}(1.5)$	1080.7160(23) nm
1, 3	$P_{12}(3.5)$	907.7422(16) nm	$R_{11}(2.5)$	1080.7778(23) nm
2, 4	$P_{12}(4.5)$	907.8153(16) nm	$R_{11}(3.5)$	1080.8464(23) nm
3, 5	$P_{12}(5.5)$	907.8780(16) nm	$R_{11}(4.5)$	1080.9168(23) nm
4, 6	$P_{12}(6.5)$	907.9291(16) nm	$R_{11}(5.5)$	1080.9871(23) nm

	$A\,^2\Sigma^+ \leftarrow X\,^2\Pi_{3/2}$		$H\,^2\Sigma^+ \leftarrow A\,^2\Sigma^+$	
N^+	branch	wavelength	branch	wavelength
0, 2	$P_{12}(2.5)$	226.9145(4) nm	$R_{11}(1.5)$	540.3580(12) nm
1, 3	$P_{12}(3.5)$	226.9356(4) nm	$R_{11}(2.5)$	540.3889(12) nm
2, 4	$P_{12}(4.5)$	226.9538(4) nm	$R_{11}(3.5)$	540.4232(12) nm
3, 5	$P_{12}(5.5)$	226.9695(4) nm	$R_{11}(4.5)$	540.4584(12) nm
4, 6	$P_{12}(6.5)$	226.9823(4) nm	$R_{11}(5.5)$	540.4936(12) nm

that the rise time of circuit version 1 was already analyzed in section 4.3, which was 12.7 ms. The rise and fall time τ_{TIA} can be measured by applying a constant input current at the TIA's input node. In our setup this means lock some or all lasers to a transition, and then quickly block and unblock one of them. Out of practicability the first two lasers were used. During a block of the green laser the voltage output of the TIA dropped and after unblocking it increased again. At least to obtain an estimation the output voltage of the TIA may be approximated as a low–pass filter in first order, i. e. [110]

$$V(t) = V_0\left(1 - \exp\left[\frac{-t}{\tau}\right]\right) \quad , \tag{5.8}$$

with time constant τ. The voltage V_0 is the maximum voltage reachable, i. e. the voltage after the rise/ fall time τ passed. The averaged rise and fall time of the TIA is $\tau_{\mathrm{TIA}} \approx 121\,\mu\mathrm{s}$ [120], where the rise time is defined as the time range where the signal increases from 10 % to 90 % of its maximum value. This is significantly better than the value of the old circuit of 12.7 ms, and makes the use of a lock–in amplifier feasible. By using equation (5.8) it is possible to give an estimate on the possible modulation

frequency. The time t_{99}, where $V(t) = 99\,\% \cdot V_0$ is reached, is $t_{99} \approx 5\tau$. Thus, for charging and discharging an estimated upper bound of the possible modulation frequency is $\nu = 1/10\tau_{\mathrm{TIA}} \approx 826\,\mathrm{Hz}$.

The Rydberg laser itself is scanned with scan time t_{scan} on the Rydberg transition. In figure 5.3 typical individual traces are shown. The second transition has a FWHM of around $\gamma_{\mathrm{H}\leftarrow\mathrm{A}} = 2\pi \times 70\,\mathrm{MHz}$, which is taken as a lower bound. Based on experience good results can be achieved by scanning up to $2\pi \times 30\,\mathrm{GHz}$ in about 20 s. We then observe no broadening due to any post processing with the lock–in amplifier. The integration time of the laser is then $t_{\mathrm{Laser}} = 19\,\mathrm{s} \cdot 70\,\mathrm{MHz}/15\,\mathrm{GHz} \approx 89\,\mathrm{ms}$. This means the lock–in amplifiers rise time t_r must not exceed this to leave the width of

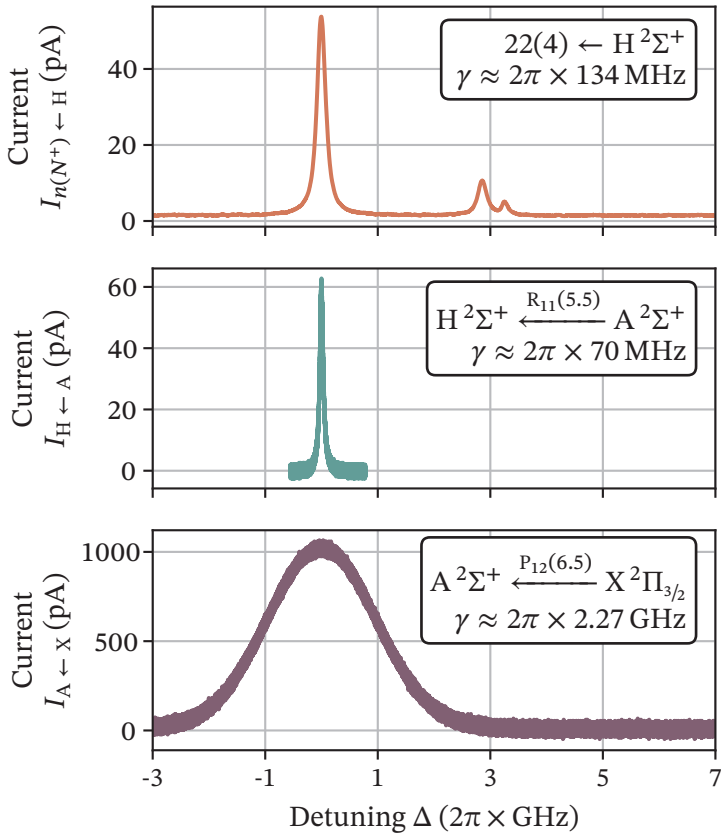

Figure 5.3: Exemplary single traces of all transitions, when exciting to a Rydberg state of NO. For the two lower transitions the pressure is set to ≈ 1.10 mbar and the applied field for these transitions is $\approx 12\,\mathrm{V\,cm^{-1}}$. For the Rydberg transition the pressure is ≈ 31 µbar, and the field is $\approx -0.5\,\mathrm{V\,cm^{-1}}$. A lock–in amplifier referenced by the modulation of the second transition has been in place for the signal of the second and the Rydberg transition. To extract the FWHM the UV transition is fitted using a Gaussian and the other two using a Lorentzian, see subsection 3.4.2.

the peak untouched. A lock–in amplifier can be modeled as low–pass filter of order o. The rise time t_r with time constant τ is [108]

$$t_r = \frac{2\pi}{3} \cdot \tau \cdot \sqrt{o} \quad . \tag{5.9}$$

The lock–in amplifier allows setting order and time constant of the filter. Based on equation (5.9) a constant τ of 30 ms and order 1 yields $t_r = 62.8$ ms, and the same constant but order 3 yields 108.8 ms [120]. There is a very small increase in width of the peak visible when using a $\tau = 30$ ms experimentally, though the gain in SNR justifies the use nevertheless.

The use of $\tau = 30$ ms has been further justified in [120] by looking at the SNR of the signal. We define our SNR like

$$\mathrm{SNR} = \frac{(A - B)}{p/2} = \frac{2\,(A - B)}{p} \quad , \tag{5.10}$$

where A is the maximum signal height, B is the averaged base of the signal and p is the peak–to–peak noise defined as the lower and upper bound of the noise outside the feature region. A plot explaining the variables is shown in figure 5.4. At a field of approximately 11.9 V cm^{-1}, the SNR was analyzed at different time constants τ of the lock–in amplifier. NO was excited to 22(4) and the pressure was in the low µbar–range ensuring negligible collisional broadening. The high field makes the high–l–fan visible (see section 5.3), which was zoomed onto. Modulation was performed with a single lock–in amplifier, for one measurement set on the H $^2\Sigma^+ \leftarrow$ A $^2\Sigma^+$ transition laser, and for the other on the Rydberg transition.

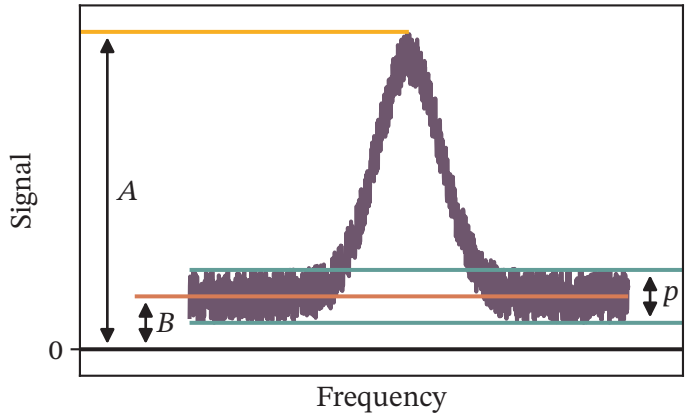

Figure 5.4: Plot explaining the variables in equation (5.10) to calculate the SNR of a signal.

The measurement results are shown in figure 5.5. It turns out, that the SNR is slightly better when modulating the Rydberg and not the second transition. However, the improvement is small and considering the higher effort of modulating and stabilizing the scanned transition, the lock–in amplifier was only used on the second transition for all measurements presented in this chapter. In [120] the effect of two lock–in amplifiers, one on the $H\,^2\Sigma^+ \leftarrow A\,^2\Sigma^+$ and one on the $n(N^+) \leftarrow H\,^2\Sigma^+$ transition, was analyzed as well. However, acceptable results were only achieved when setting the second modulation frequency to about 80 Hz. To not alter the signal, this means that the scan time and thus the measurement time increases significantly by a factor of about 3. Acquiring useful data is almost impossible at this speed, since the locks of the locking setup are likely to drop within that range. Thus, only a single lock–in was used during the measurements. Additionally, this took into account that the improvement in SNR by using two lock–in amplifiers was small.

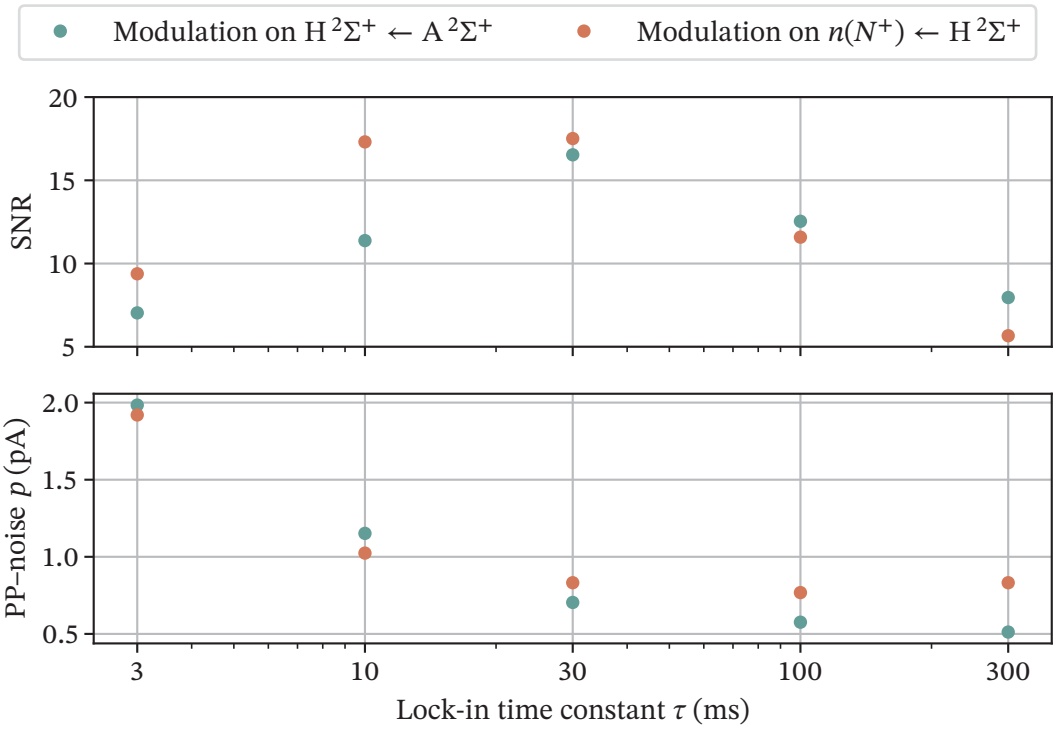

Figure 5.5: Comparison of the SNR when modulating the $H\,^2\Sigma^+ \leftarrow A\,^2\Sigma^+$ or $n(N^+) \leftarrow H\,^2\Sigma^+$ transition and using a lock-in for the readout. The modulation is realized by an AOM. The state used for all measurements is 22(4) and the field is set to $\approx 11.9\,\mathrm{V}$, making the high–l–fan prominently visible. Despite the slight improvement in SNR when modulating the Rydberg transition, we used the lock–in amplifier for all measurements on the $H\,^2\Sigma^+ \leftarrow A\,^2\Sigma^+$, since the AOM of the Rydberg transition then only has to stabilize the scanned laser. This analysis is the result of a Bachelor's thesis [120].

5.2.4 Common data acquisition and evaluation steps

The way the data for the Stark effect and pressure shift measurements is gained is almost identical, only differing in the varied parameter. On $H\,^2\Sigma^+ \leftarrow A\,^2\Sigma^+$ we use a lock–in amplifier, the modulation of the laser is realized via an AOM. The sensitivity is adjusted when necessary, the time constant is 30 ms. The modulation frequency is 475 Hz and the low–pass filter slope is $-18\,\mathrm{dB\,oct^{-1}}$. The Rydberg transition laser is stabilized in power via another AOM. Due to a lack of power in the UV this transition is not stabilized. The general measurement procedure is:

1. Choose a Rydberg state $n(N^+)$.
2. Stabilize the reference laser and all transfer cavities of the locking setup (figure 3.4).
3. Find the transition and lock the lower two lasers to their branch (table 5.1).
4. Scan the Rydberg laser over a detuning of $\Delta_{n(N^+)\leftarrow H} \approx 2\pi \times 13\,\mathrm{GHz}$ (pressure shift) or $\Delta_{n(N^+)\leftarrow H} \approx 2\pi \times 30\,\mathrm{GHz}$ (Stark effect). In the case of the pressure shift it is zoomed in on the high–l–manifold.
5. Record the lock–in amplifier's output signal as well as the transfer cavity's transmission signal of the Rydberg laser.
6. Change the electric field (Stark effect) or pressure by one step size and repeat from 4.

Parameters like the associated wavelengths (ranges) and the lock–in amplifier settings are kept constant and saved alongside the data. The only exception is the sensitivity of the lock–in amplifier. The measurement routine is automated after step 4 is reached. Thus, both measurement types share the first evaluation steps, which are explained here. The differences are then explained in their appropriate sections, where also the individual parameters are given.

A measured dataset always consists of several individual measurement steps. All signals are voltage signals in dependence of time t. Every trace has 2.5 million measurement points. The common evaluation steps are:

1. Convert from time to frequency by using the cavity signal and the known FSR of the transfer cavity.
   a) The peak positions are found via an algorithm. To account for a change in the peak relative heights we use the following approach.
      i. The full time axis is divided into three sections. Three proved to be most useful.
      ii. A simple peak finding algorithm is used in each division, where the expected peak height and spacing is given as parameters. The resulting positions are added to an overall array.

iii. We fit the height of the found peaks with a polynomial function with a maximum order of seven. Then we normalize the cavity signal with the fit results.
iv. The peak finding algorithm is used on the normalized cavity signal.
v. If a previous cavity evaluation is already available, the number of peaks is compared. If they do not match, it is assumed that we missed a peak, and we scale the position array accordingly. A failure of this step would be visually striking in any evaluation, since the FSR of the cavity is about 900 MHz, i. e. well above any results extracted.

b) The peak distance is the FSR. To account for the non-linearity of the scan, we fit the distance against the position in time using a third order polynomial function.
c) If a single trace was evaluated previously, the current peak positions are compared to the previous ones. An offset added to the polynomial adjusts for any drift in the cavity signal, such that the peaks overlay.
d) The overall frequency axis is cut such, that it contains the data of the current trace and all previous data. This means that the overall frequency range shrinks by small amounts during the evaluation, i. e. the outer parts of the signal are cut.

2. Convert the output voltage of the lock–in amplifier using the known sensitivity to the TIA's output voltage.
3. Convert the TIA's voltage via the known feedback resistance $R_{\mathrm{FB}} = 1\,\mathrm{G\Omega}$ to a current.
4. To smooth the data, a Savitzky-Golay-Filter with a polynomial order of three is used. The window length is adjusted such, that a following reduction to about 10 000 points per trace does not change the quality. The reduction of points has the advantage that subsequent fits to the data converge on more reasonable time scales.
5. Convert the voltage V applied to the electrode to a field F by assuming an ideal plate capacitor with distance d, $F = V/d$.
6. Repeat steps 1 to 5 for all single traces of the dataset.

After evaluating the data there is a common frequency axis and all individual TIA output traces available per dataset. The data is then further processed individually.

5.3 The Stark effect in Rydberg states

5.3.1 Stark Hamiltonian

The Stark effect describes a splitting in the energy levels of atoms or molecules under the influence of an electric field. In subsection 2.3.2 the formal treatment of the calculation of Rydberg states was introduced. It is based on a two-fold approach, using matrix diagonalization and corrections by MQDT.

Molecular Rydberg states are Hund's case (d) states, i. e. $N = N^+ + l$, and each rotational level has $2l + 1$ components, refer to subsection 2.1.3. Working with Rydberg states with only a single Rydberg electron the lower case letter l is used for the orbital angular momentum.

According to subsection 2.3.2 the overall Hamiltonian without any externally applied field is

$$H_0^{(\mathrm{d})} = H_{\mathrm{diag}}^{(\mathrm{d})} + H_{\mathrm{dip}}^{(\mathrm{d})} + H_{\mathrm{multi}}^{(\mathrm{d})} \quad . \tag{5.11}$$

This Hamiltonian can be adjusted such, that it includes effects of an externally applied electric field. Let the field $\boldsymbol{F}$ be applied along the z–axis, i. e.

$$H_{\mathrm{Stark}}^{(\mathrm{d})} = -\boldsymbol{d}\boldsymbol{F} = -ezF_z \quad , \quad \boldsymbol{F} = (0, 0, F_z)^{\mathrm{T}} \quad , \tag{5.12}$$

where $\boldsymbol{d}$ is the electric dipole operator, e is the elementary charge, and z is the z–coordinate. The additional Hamiltonian to equation (5.11) can be written as [3]

$$\begin{aligned}\left\langle \eta^{(\mathrm{d})}, l, N^+, N, M_N \middle| H_{\mathrm{Stark}}^{(\mathrm{d})} \middle| \eta^{(\mathrm{d})\prime}, l', N^{+\prime}, N', M_N' \right\rangle = eF_z\,(-1)^{N-M_N+N'+N^++l+1} \\ \times\sqrt{(2N+1)\,(2N'+1)} \begin{pmatrix} N & 1 & N' \\ -M_N & 0 & M_N' \end{pmatrix} \begin{Bmatrix} l & N & N^+ \\ N' & l' & 1 \end{Bmatrix} \chi\left(\eta^{(\mathrm{d})}, l, \eta^{(\mathrm{d})\prime}, l', r\right) \delta_{N^+,N^{+\prime}} \quad ,\end{aligned} \tag{5.13}$$

where the integral $\chi\left(\eta^{(\mathrm{d})}, l, \eta^{(\mathrm{d})\prime}, l', r\right)$ is given by

$$\chi\left(\eta^{(\mathrm{d})}, l, \eta^{(\mathrm{d})\prime}, l', r\right) = \begin{cases} -\sqrt{l+1}\left\langle \eta^{(\mathrm{d})} l \middle| r \middle| \eta^{(\mathrm{d})\prime} l+1 \right\rangle & \text{if } l' = l+1 \\ \sqrt{l}\left\langle \eta^{(\mathrm{d})} l \middle| r \middle| \eta^{(\mathrm{d})\prime} l-1 \right\rangle & \text{if } l' = l-1 \\ 0 & \text{if } l' = l \end{cases} \quad . \tag{5.14}$$

The Stark Hamiltonian in equation (5.13) results in an off-diagonal coupling of states within the same N^+–series, i. e. [3]

$$\Delta l = \pm 1, \quad \Delta N^+ = 0, \quad \Delta N = 0, \pm 1 \text{ (not } 0 \leftarrow 0), \quad \Delta M_N = 0 \quad . \tag{5.15}$$

5.3.2 Linear and quadratic Stark effect

The strength of the induced dipole moment when applying an electric field F depends on the polarizability α, which scales $\propto n^7$ for Rydberg states, see table 2.2. This makes Rydberg states especially attractive for Stark effect measurements. Two different types of the Stark effect are distinguished, the linear and the quadratic Stark effect. Both are "included" in equation (5.13).

For non-degenerate states there is the quadratic Stark effect, i. e. their energy shifts in a quadratic way with linearly increasing field. For degenerate states the linear Stark effect is observed. Descriptively this can be explained by the (non–)existence of a permanent electric dipole moment in the individual state. A non-degenerate state may not have a permanent electric dipole moment, however, the external electric field changes the Rydberg electron's probability of presence, thus inducing a dipole moment. Degenerate states have a permanent dipole, and the splitting is linear. The linear region of the Stark effect is typically called "high–l–manifold", as the resulting lines can be described by superpositions in l.

For a strong electric field a formerly quadratically behaving state, might approach a linearly split state and the quadratic Stark effect may turn into a linear one. This is sketched in figure 5.6.

Note that the linear Stark effect mixes states of orbital angular momentum quantum number l, i. e. l is not a good quantum number anymore. The linear region is oftentimes named as "high–l–manifold". In addition, when considering NO, the quantum number N may change, since l may change, but the projection m_N remains a good quantum number.

For the linear Stark effect in NO the splitting in energy between two neighboring states can be calculated as [121]

$$\Delta E = e a_0 \cdot 3nF \quad , \tag{5.16}$$

linking the splitting directly to the principal quantum number n of a particular state. Here, a_0 is the Bohr radius.

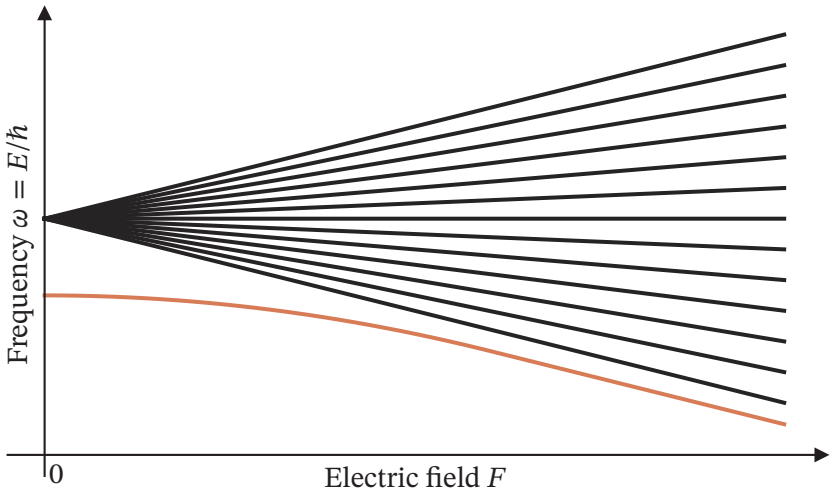

Figure 5.6: Sketch of a typical state splitting due to the Stark effect. The dark-colored states are degenerate, and split up linearly with increasing field due to the linear Stark effect. The states are superpositions in l, and this part is typically called "high–l–manifold". The red-colored state is non-degenerate, and is subject to the quadratic Stark effect with increasing electric field. At some point it reaches an energetic level, where it becomes degenerate with a neighbouring state and behaves according to the linear Stark effect thereafter.

5.3.3 Evaluation

The measurement data is acquired as described in subsection 5.2.4. The pressure is typically in the range of 30 µbar to 70 µbar, as introduced in subsection 4.3.3. The electric field is changed from $\approx -11.9\,\mathrm{V\,cm^{-1}}$ to $11.9\,\mathrm{V\,cm^{-1}}$, a typical step size is $0.24\,\mathrm{V\,cm^{-1}}$.

After the common evaluation as in subsection 5.2.4 the single traces can be immediately plotted denoted by their field associated. A Stark map is a plot in the style of figure 5.6. In the experimental Stark map, three variables are visualized, the detuning $\Delta_{n(N^+)\leftarrow\mathrm{H}}$, the electric field F and the current I. Individual traces are stacked "vertically" next to each other. The third dimension is introduced with a color map while the plot itself is two-dimensional. Usually the color map would linearly translate the current to a color in the map. However, in the evaluation the mapping is adjusted visually such that it enhances features of the measurement. This is realized by replacing the linear mapping function with a cubic spline, which interpolates points adjusted visually. This makes the color gradient of all color bars highly non-linear. Thus, any ticks on the color bars given should be seen as guide to what currents are measured in a particular measurement.

It is interesting to look at the position of a particular line in the high–l–manifold with changing field. This allows to determine the zero–field position and as such also the linearity of the electric field in the cell. On top the frequency splitting between the high–l–manifold's zero position and any lower state may be used to determine the quantum defect of a particular substate. As such a fit routine to determine the zero–field position of any state on the Stark map is required. Any measured data set contains about 100 to 150 steps of the electric field F. Hence, it is not feasible to fit every single trace individually, but instead an iterative approach is used.

At first, the fit routine for the high–l–manifold is described. If only positive or negative fields were measured, the dataset stays as is, if negative and positive fields were measured, the dataset will be sliced such, that one half only consists of positive and the other only of negative fields. As is sketched in figure 5.6 the high–l–manifold consists of a centered line which is not affected by the Stark effect. This line is crucial for the fitting procedure. The lines are most prominently visible for high fields. Thus, the algorithm starts from high fields and works its way to zero field. The fit uses a single Lorentzian function per line, see equation (3.12a). The procedure is as follows:

1. A plot of the measurement trace at highest field is shown to the user. The initial position values are determined by clicking on the desired peaks for fitting. The centered non-shifting line is selected by the user as well and denoted with frequency $\omega_{\text{centered peak}}$.
2. Apart from the user selected positions the algorithm has some default initial parameters for the fit of the first lines. The peak positions at the current field step are fitted using a Lorentzian and the positions extracted. The fit result is given to the next iteration.
3. Due to the first step, the algorithm knows how many peaks are to the left (lower frequency) and to the right (higher frequency) of the centered line. When looking at figure 5.6 in the direction of decreasing field, peaks with lower frequency shift to higher frequencies and vice versa.
4. The following steps are iterated for each peak in each trace after the first one.
   a) Load the next trace with the electric field changed by one step.
   b) Adjust the search range for the next peak to either higher or lower frequencies based on the position relative to the centered line.
   c) Use the previous fit result as start parameters for the current trace and peak. If no previous parameters are available go back up to three steps in the history of fit results before considering the signal lost and not fitting the currently viewed peak/ position anymore.
   d) Adjust the initial position parameter ω_0 (see equation (3.12a)) by weight-

ing:

$$\omega_m \equiv \delta_p + \omega_{\text{centered peak}} \tag{5.17a}$$

$$a \equiv 1 - \left| \frac{\omega_{0,\text{ previous}} - \omega_m}{\delta_p / b} \right| \tag{5.17b}$$

$$a = \begin{cases} a & \text{if: } 0 \leq a \leq 1 \\ 1 & \text{if: } a > 1 \\ 0 & \text{if: } a < 0 \end{cases} \tag{5.17c}$$

$$\omega_{0,\text{ initial}} = a\omega_{0,\text{previous}} + (1-a)\,\omega_m \quad . \tag{5.17d}$$

In all equations fit results of the previous step are used to determine a new initial position parameter $\omega_{0,\text{ initial}}$. In the first equation (5.17a) δ_p is the distance to the centered line. In the second and third step, equations (5.17b) and (5.17c), a parameter a between 0 and 1 is determined. The variable b can be adjusted to "damp" the value. In this evaluation $b = 3$. In the last step a new initial value $\omega_{0,\text{ initial}}$ is determined.

e) Fit the line using a Lorentzian using the weighted position $\omega_{0,\text{ initial}}$ and all other parameters from the previous fit as start parameters.

Next we look at the fit routine for states below the high–l–manifold, i. e. states which initially behave in a quadratic way as depicted in figure 5.6. Here the routine is a little simpler, and works its way from lower to higher fields. If the Stark map was recorded for fields below and above zero, only "one side" is fitted. Based on experience the fit works best between fields of $-1\,\text{V}\,\text{cm}^{-1}$ to $-3\,\text{V}\,\text{cm}^{-1}$, and as such only this region is fitted. The routine works as follows:

1. Treat a single trace.
   a) Determine the frequency position of the maximum in a single trace as initial parameter for the position of the Lorentzian fit. Use the maximum as initial parameter for the amplitude, and the minimum of the trace as initial parameter for the offset.
   b) Perform the fit and cache the optimized parameters.
   c) Subtract the fit from the current single trace, and repeat step 1 and 2. As such the lowest peak of the overall trace is fitted.
   d) Stop fitting the current trace as soon as the signal is lower than 7 % of the original signal, and continue with the next single trace.
2. Sort the found parameters and assign them to a peak by comparing consecutive positions.
3. Determine how many consecutive positions were found.
4. For any peak, where the fit was successful often enough, fit the positions with

a quadratic behavior as

$$f(x) = a \cdot (x - b)^2 + c \quad ,$$

where a, b and c are fit parameters. By using this fit function the zero field position is given by c.

This routine does not prevent that parts of the high–l–manifold are fitted as well. However, by post selection, these fits can simply be discarded.

5.3.4 Results

The measurement parameters of all discussed Stark measurements are given in table 5.2. The measurement of the Stark effect was at first primarily used to determine the performance of the cell in the setup. As such it is educative to look at a measurement done with the old cell and old circuit and compare it with the currently employed cell. The cell named old cell here is the cell used in subsection 4.3.1. It has an electrode spacing of 2 cm and features circuit version 1 including the feedback capacitance of 18 pF. The electrode area of the old cell is $w \times l = 10\,\text{mm} \times 14\,\text{mm}$ and a copper plate is glued to the bottom. The new cell has circuit version 2, an electrode spacing of 0.84 cm and a PCB electrode area of in total $w \times l = 35\,\text{mm} \times 14\,\text{mm}$ realized with a guard ring. For more information refer to chapter 4.

Table 5.2: Experimental parameters used in the measurements presented in this section. The letters A to D are referred to in the text. The abbreviations are "int." for intensity and "br." for branch. The intensities are rounded, and have an error of 7 %, 5 % and 3 % from the lowest to highest transition due to the used powermeter head. The pressure has an uncertainty of 30 %.

	A, figure 5.7a	B, figure 5.7b	C, figure 5.13	D, figure 5.13
State	42(5)	22(3)	42(2) & 35(4)	32(2)
circuit version	1	2	2	2
electrode spacing	2 cm	0.84 cm	0.84 cm	0.84 cm
TIA resistor	470 MΩ	1 GΩ	1 GΩ	1 GΩ
pressure	114 µbar	59 µbar	57 µbar	55 µbar
lock–in used	no	yes	yes	yes
int. A ← X	2.0 mW mm^{-2}	1.1 mW mm^{-2}	1.1 mW mm^{-2}	0.9 mW mm^{-2}
int. H ← A	752 mW mm^{-2}	477 mW mm^{-2}	447 mW mm^{-2}	447 mW mm^{-2}
int. $n(N^+)$ ← H	580 mW mm^{-2}	47 mW mm^{-2}	62 mW mm^{-2}	47 mW mm^{-2}
br. A ← X	$P_{12}(5.5)$	$P_{12}(5.5)$	$P_{12}(4.5)$	$P_{12}(4.5)$
br. H ← A	$R_{11}(4.5)$	$R_{11}(4.5)$	$R_{11}(3.5)$	$R_{11}(3.5)$

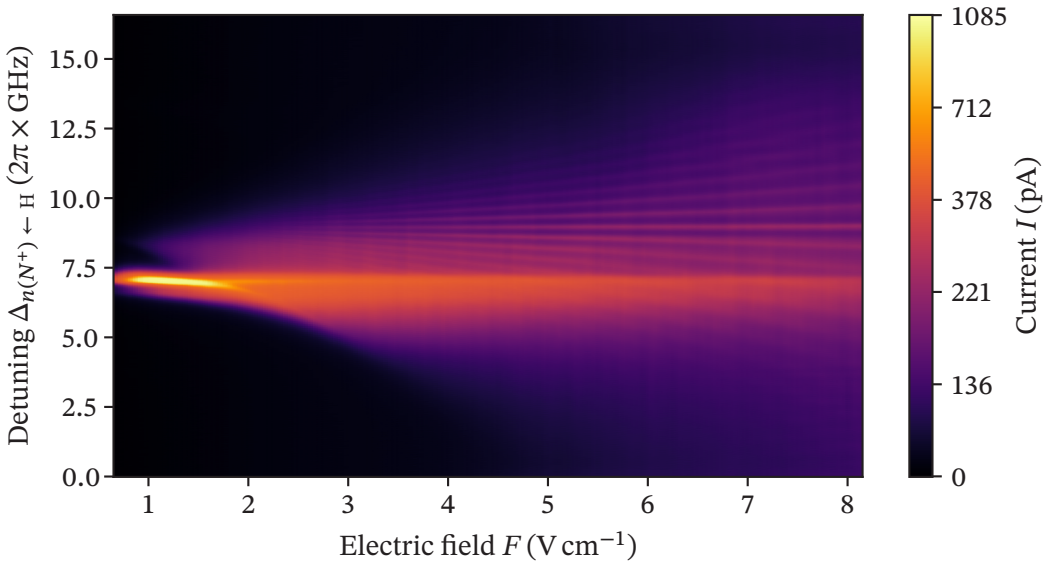

a) Stark map of 42(5) measured with the old cell. Parameters were A in table 5.2.

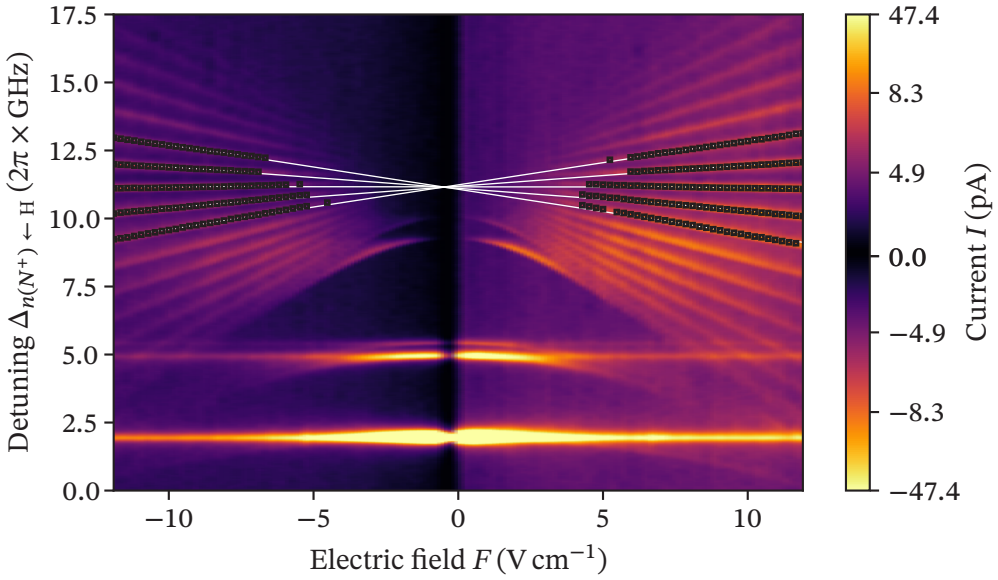

b) Stark map of 22(3) using the most recent cell and circuit. The black squares are the positions found using the algorithm described in subsection 5.3.3. The white lines are a linear fit to the found positions. However, we will see in subsection 5.3.5 that a linear fit is not appropriate. Still, the zero–field position of the field of $F_{\mathrm{zero}} \approx -0.5\,\mathrm{V\,cm^{-1}}$ can be extracted, due to the symmetry of the measurement. It is a constant to all Stark maps fitted, which where measured with the new cell. Parameters were "B" in table 5.2.

Figure 5.7: Stark maps measured with old and new cell.

Comparison between current and old cell

In figure 5.7a a Stark map of 42(5) using the old cell is shown. Here the field was only varied in positive direction. For comparison in figure 5.7b a Stark map of 22(3) using the most recent cell is shown. This map additionally has the positions of some peaks in the high–l–manifold fitted using a linear function. This is sufficient to extract the typical zero field position of about $0.5\,\mathrm{V\,cm^{-1}}$, yet we will see in subsection 5.3.5, that a linear fit is not appropriate to describe the splitting. The peak positions were found using the algorithm described in subsection 5.3.3. When comparing both maps, both appear to have a somewhat similar quality and show the Stark splitting nicely. Problems arise when going into detail. The frequency difference of two lines at a certain field F and principle quantum number n can be calculated according to equation (5.16). One may define the ratio between the measured field F_{measured} and the expected field F_{expected}, which depends on the splitting in frequency $\Delta\nu = \Delta E/h$ and the principal quantum number n in accordance with equation (5.16), as:

$$\mathcal{F}_{\mathrm{ratio}} = \frac{F_{\mathrm{expected}}}{F_{\mathrm{measured}}} = \frac{h\Delta\nu/\left(3nea_0\right)}{F_{\mathrm{measured}}} \tag{5.18}$$

The field F is calculated based on the assumption of an ideal plate capacitor. The energy difference ΔE can be translated to a frequency difference $\Delta\nu$, which in turn can be extracted from the measurement by fitting the positions of some peaks in the high–l–fan as introduced in subsection 5.3.3. The ratio should obviously be constant

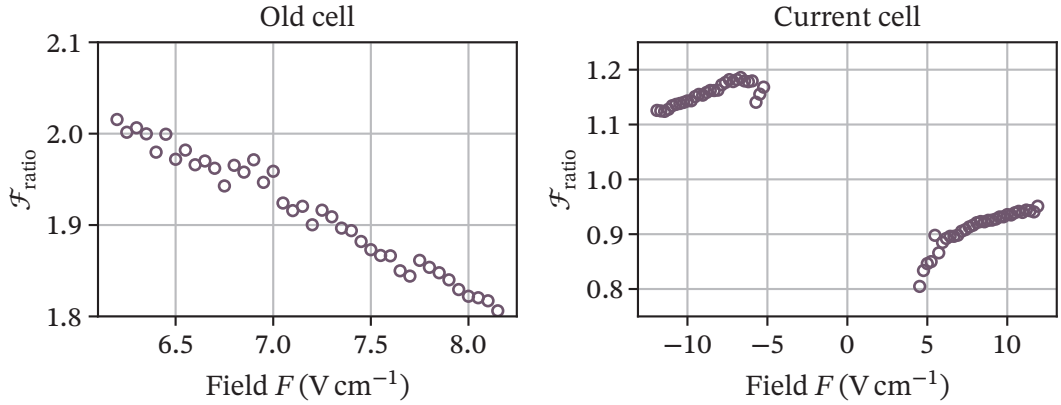

Figure 5.8: Plot of the ratio equation (5.18) for different electric fields for the measurements of 42(5) with the old cell shown in figure 5.7a, and for 22(3) for the new cell shown in figure 5.7b. For both measurement the position of the centered line and the two neighbouring ones were fitted. The plot shows the averaged ratio per field. A ratio of 1 is desired, a higher ratio means, that the molecules experience a field smaller than expected.

and ideally equal to unity in all cases. Further the state chosen should not matter. The state 22(3) for the new cell was simply chosen as fitting is easier, since the high–l–fan has a higher offset to other lines. For the old cell only the measurement of 42(5) is available. A plot of equation (5.18) is shown in figure 5.8. For the old cell the ratio is about 2. This means that on average the actual field experienced by the molecules is by a factor of 2 smaller than the field targeted. For the new cell featuring a larger electrode however, the ratio is closer to 1, though some interesting effects can be seen for low fields.

That the ratio can be attributed to nonlinearities in the electric field inside the measurement cell has been analyzed within a Bachelor's thesis based on simulations in COMSOL [122]. For the simulation the cell was built within COMSOL while taking care of all crucial dimensions. The PCB of the respective cell was imported. The simulated field distribution is shown in figure 5.9. As can be seen, when comparing the field within the cell to that of an equivalent ideal plate capacitor the current cell outperforms the old one by far. The old cell is more than 12 % off and shows steeper field slopes close to the cell walls. The inhomogeneity is large. The offset explains the bad ratio of 2 as seen in figure 5.8 at least in parts. The strong slope apart from the cell's center means, that molecules close to the wall may experience a different electric field than those close to the cell center. As a result the lines broaden and additionally show an asymmetry.

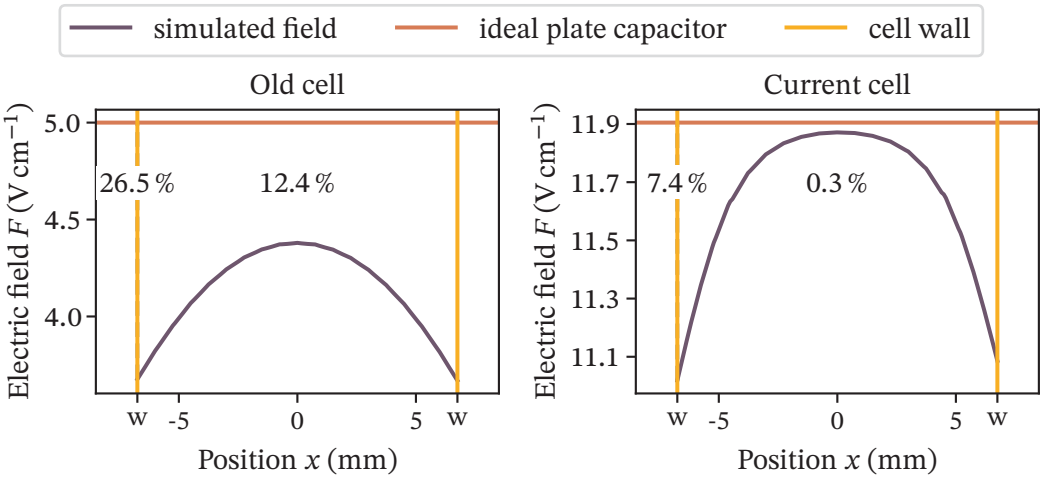

Figure 5.9: Electric field simulation of the old and new cell with COMSOL in the direction of the laser beam without considering molecules, i. e. the cell's interior is a vacuum. Within the cell the old version does not even come close to the field of an ideal plate capacitor, and the slope of the overall curve is steep. For the new cell the field is only 0.3 % shy of the field of an ideal plate capacitor, and shows still acceptable behavior outside the cell. These simulations are the results of a Bachelor's thesis [122].

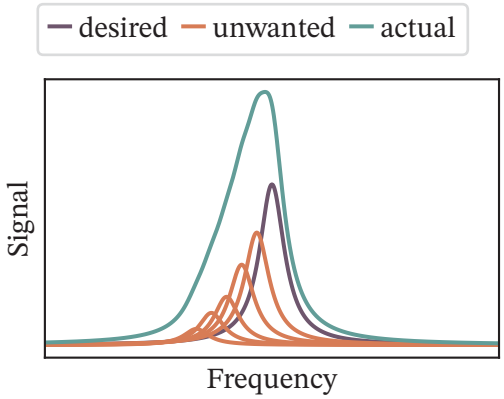

Figure 5.10: Asymmetric and broadened feature due to an inhomogeneous electric field. The unwanted features are shifted due to the Stark effect of a different field than the one expected. The plot shows a situation, where the inhomogeneity is still small when compared to the overall field. As such the amplitude of the unwanted features is small as well.

This is visualized in figure 5.10. Different electric fields cause lines to appear at different positions. This is different to the asymmetric behavior introduced in section 4.3, as it is caused directly by the molecule. This can be and was confirmed by scanning the Rydberg laser in the other direction and checking if the signal is mirrored to the previous one. Still, for the old cell, the asymmetric and slower behavior due to the bad rise time as a result of the high capacitance plays a role. This can be especially seen when comparing single traces, as is done in figure 5.11. The old cell shows a high and broad base for almost the complete measurement, whereas the new cell's features are way more distinct at high fields. This can be mainly attributed to the feedback capacitance used in the old cell. This and the inhomogeneous electric fields were the key reasons, which lead to the development of a complete new circuit and cell.

Still the current cell does not show a ratio of 1 in figure 5.8. The most likely reason for this are charges sticking to the cell walls. When assuming a constant amount of charges on the cell walls the effect should be smaller in high fields, which is the behavior visible in figure 5.8, since the ratio appears to approach 1 for higher fields. In high fields the effect of the charges becomes more and more negligible, especially as it is expected, that higher fields may remove charges at the glass partly. This was confirmed in [122] by adjusting the simulation such, that charges are generated at the cell walls. A plot of the then resulting field is shown in figure 5.12. For different surface charges the results always show the same behavior. It is important that the rapid increase of the field at the cell walls is a result of the simplifications made during the simulation, and thus must be ignored. While the field in the center is as expected, it decreases in amplitude close to the walls. As such the peak still shows a slight asymmetry, as sketched in figure 5.10. Still, in comparison to the old cell, the behavior is much improved, as the slope is not as steep, and in the cell center only 0.3 % shy of the field of an ideal plate capacitor.

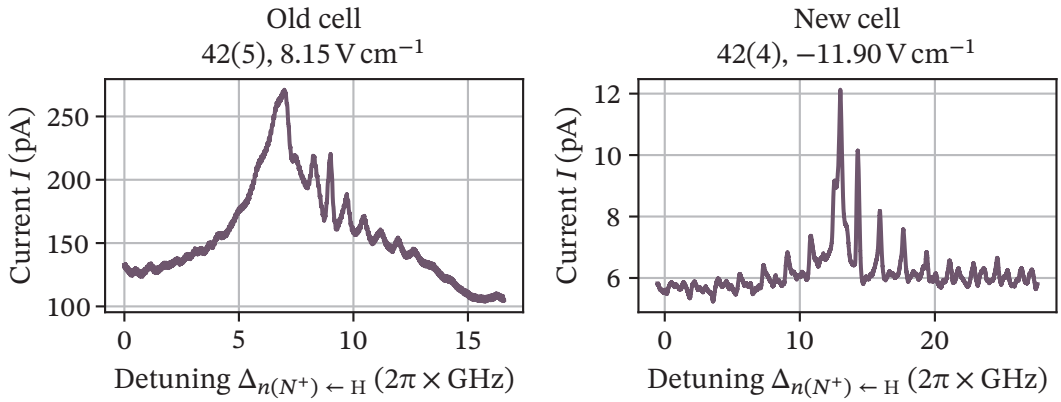

Figure 5.11: Comparison of a single trace measured in the old and new cell at high field. The old cell's measurement shows a very broad baseline below the single features. This can be attributed to the high feedback capacitance and the associated high rise time of the circuit. In contrast, the features in the new cell are far more distinct.

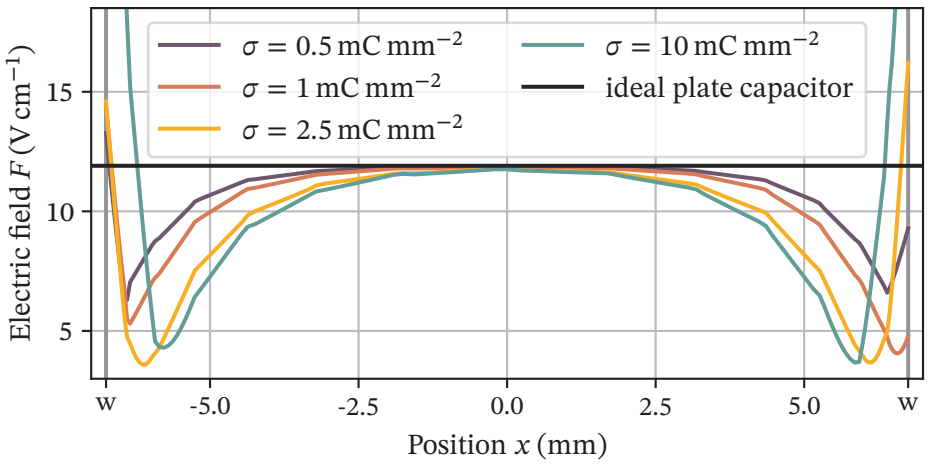

Figure 5.12: Electric field of the new cell along the laser beam, when considering a constant amount of charges at the cell walls. The cell walls are at the positions labeled with "w". The plot is shown for different surface charges σ, while the electric field applied is always 11.9 V cm^{-1}. Note that the steep increase of the field at the cell walls is a result of the simplifications made during the simulation, and not the actual field behavior. Only the behavior to the lowest point of the electric field is reliable. This plot is based on the results of a Bachelor's thesis [122].

To show the full capabilities of the new cell, figure 5.13 shows two exemplary Stark maps. On top, a couple of selected single traces at different fields F of 32(2) are shown in figure 5.14. The measurement of 32(2) shows great resolution in the high–l–manifold as well in the low fields, where the quadratic onset is visible. The upper plot shows a plot for two states which are close to each other, 42(2) and 35(4). Here the lines start to cross each other at high fields, which can be resolved. While this is not absolutely certain, at least equation (2.40) couples different N^+, i. e. avoided crossings may occur. The high resolution is only possible, since the line width of the Rydberg transition is in the MHz–regime, as shown in figure 5.3, and the much reduced rise time of about 120 μs of the new circuit.

However, as was already the case for the previous maps, there is always a line unaffected by the electric fields and states nearby which is basically at a constant detuning $\Delta_{n(N^+)\leftarrow\mathrm{H}}$ for all considered fields. At this point these lines are not fully understood, but they certainly don't make sense from a molecular point of view. Most likely there is still some residual field inside the cell, thus for some molecules there is no Stark effect. On the other hand the amount of affected molecules should be small.

Still, the resolution shown here is to the knowledge of this project's team unmatched, as research on NO is basically only done using pulsed laser systems, e. g. [3, 4]. As such the ability to resolve the Stark effect at low fields will be of great value for testing and refining the theory.

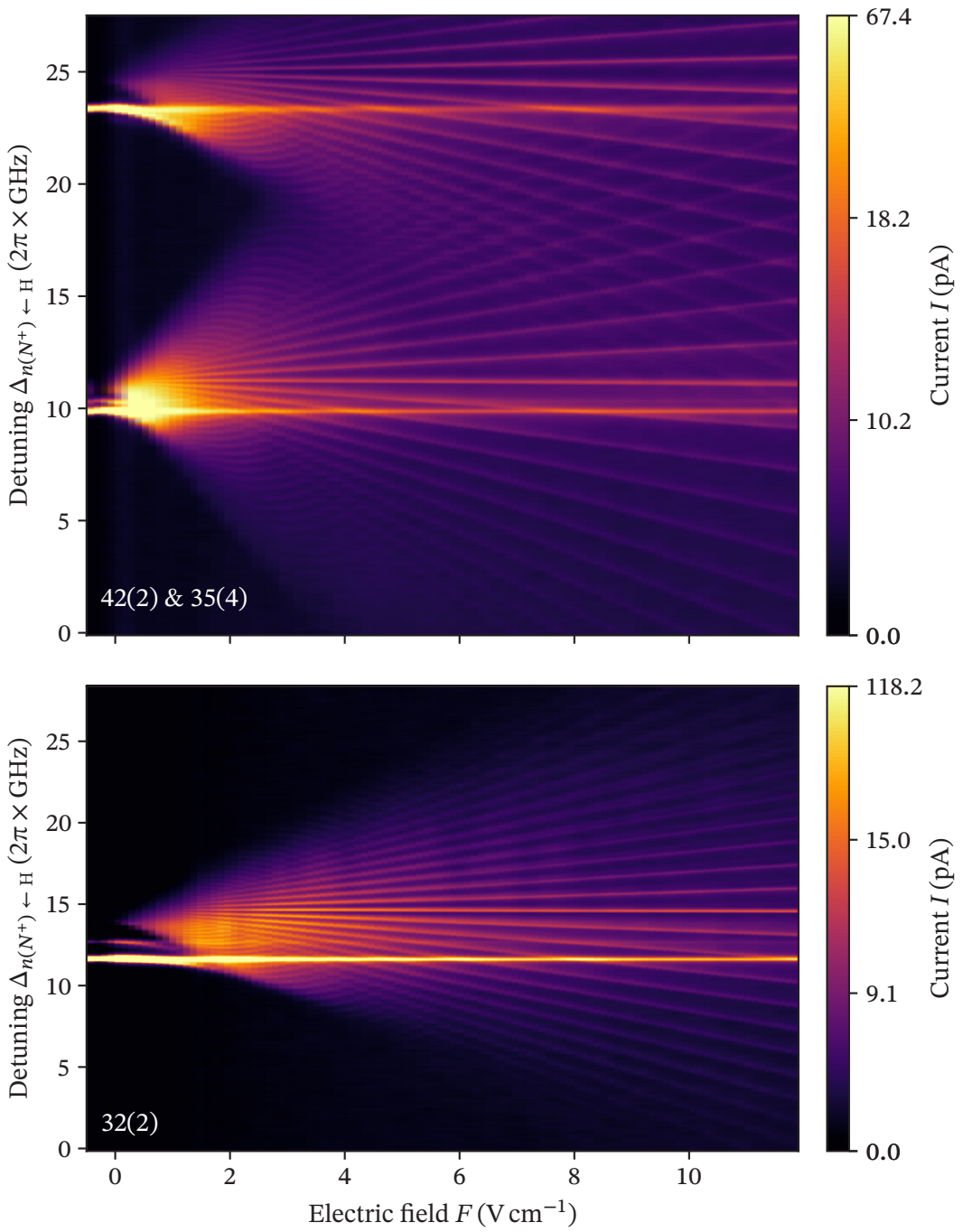

Figure 5.13: Two Stark maps measured with the new cell. The lower map of 32(2) is an example for a state which has no other states nearby. The upper map of 42(2) and 35(4) shows the map for two states next to each other. The measurement parameters are in column C and D in table 5.2.

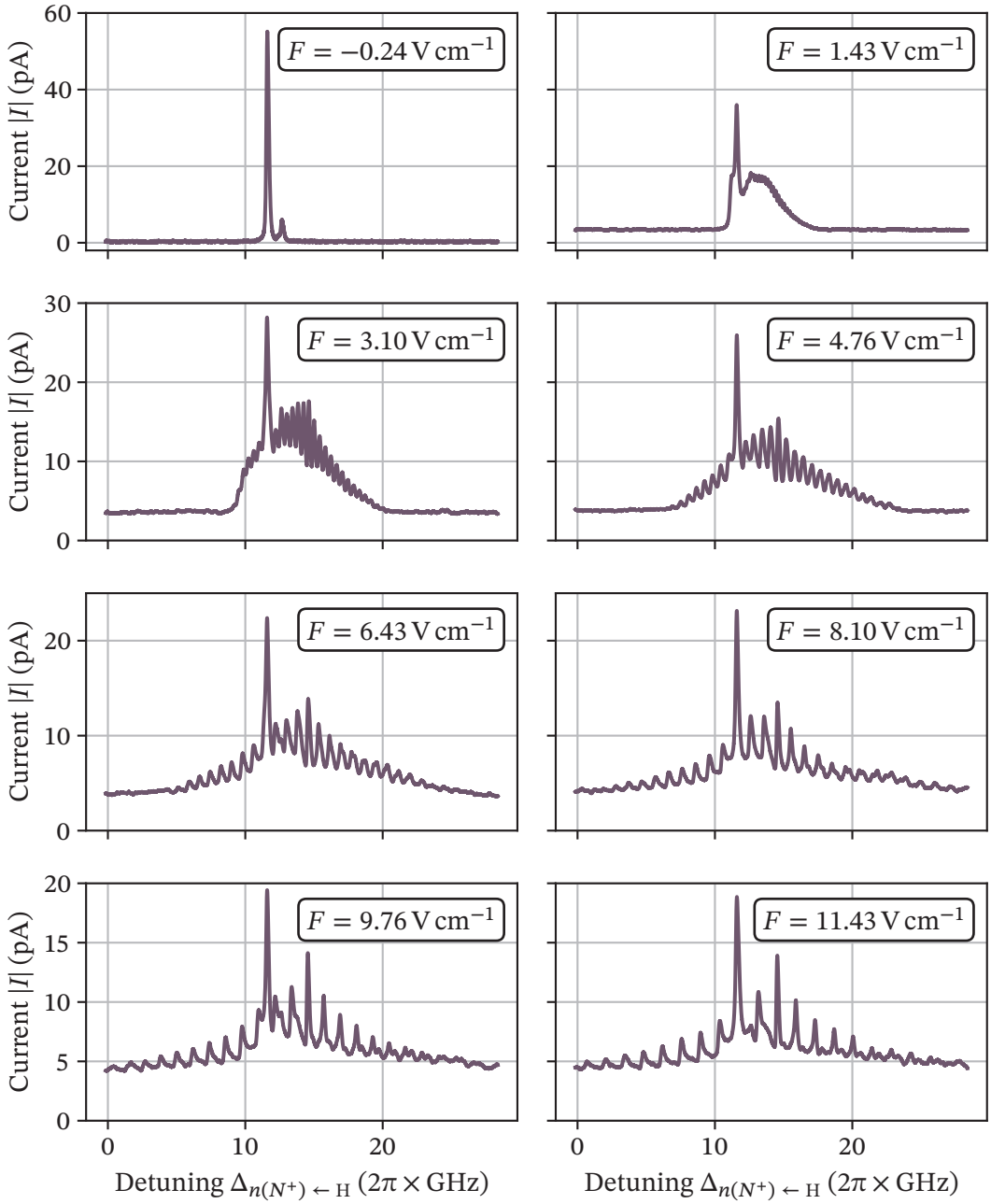

Figure 5.14: Selected single traces for different electric fields F while measuring 32(2). A Stark map of this state is shown in figure 5.13. The measurement parameters can be found in column D in table 5.2.

5.3.5 Outlook

Figure 5.15 shows a Stark map of 22(0) up to fields of about 38 V cm^{-1}. As mentioned, from a theoretical point of view the unaffected lines at a constant detuning $\Delta_{n(N^+)\leftarrow \mathrm{H}}$ should not exist. To our understanding, they should only be visible if there are zero–field positions in the cell, even if the applied voltage is increased. In figure 5.15 these lines show no interaction with the then crossing high–l–manifold. This supports the made argument, as otherwise avoided crossings should be visible. As such, we assume, that we can safely ignore these lines in future discussions.

In literature, the quantum defect up to f–states for NO appears to be well known [3], yet for the g–state only the bounds are known, 0.002 to 0.004 [19, 20]. We can use our measurements to give precise values to the quantum defect δ in g in the future. Here, the distance in frequency between the zero position of the high–l–manifold and any split-off states has to be determined. The extraction algorithm has been described in subsection 5.3.3. In general, it is easier to fit states with low principal quantum number n, as there is a larger splitting in frequency. Note that the fit allows us to ignore any field irregularities, as only the zero–field position is considered. Additionally, a lower principle quantum number n gives higher precision in the

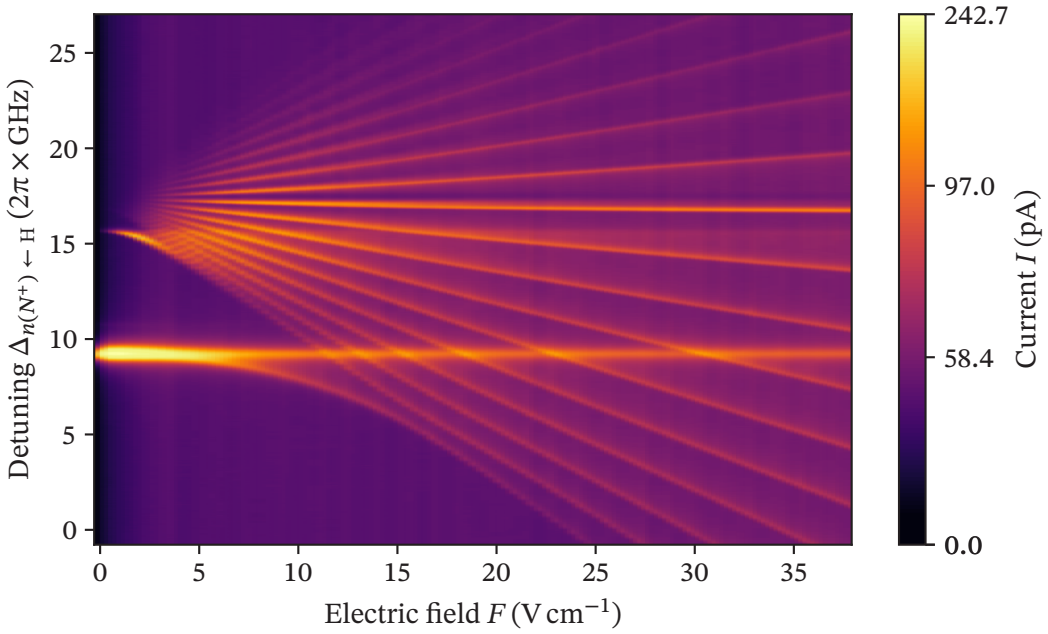

Figure 5.15: Stark of 22(0) for fields F of up to about 38 V cm^{-1}. This map shows, that the unaffected, constant line of the f–state does not interact with the high–l–manifold. If the contribution would not have its origin in remaining zero–field positions in the cell, avoided crossings would be expected.

determined splitting, as the splitting itself is larger. In figure 5.16 another Stark map of 22(0) with markers on the positions found of the high–l–manifold and fits of the lower l states is shown. Note that this Stark map was measured after optimizing the optical setup such, that the direct TIA output can be used. On top, this Stark map is measured with a step size of only about 6 mV cm^{-1}. Other parameters were in the same range as those of previous maps. In contrast to previous maps measured this resolution reveals, that the high–l–manifold does not show a linear behavior for low fields.

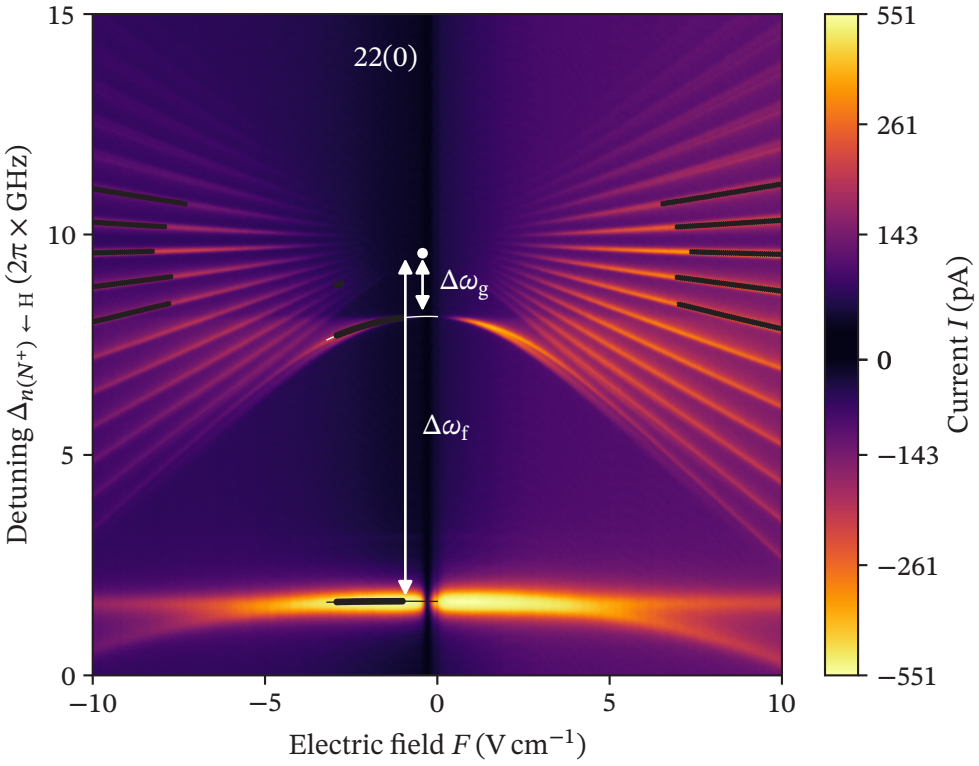

Figure 5.16: Stark map of 22(0), where the high–l–manifolds and lower states are fitted such, that the zero–field position can be deduced. The white and filled circle is the zero–field position if using a linear fit, and only used for labeling. Most likely the lowest state is the 22f(0) and the next higher one is the 22g(0)–state. Their respective splitting to the high–l–manifold are $\Delta\omega_f$ and $\Delta\omega_g$.

At this point our cooperation partners, Stephen Hogan and Matthew Rayment at the University College London (UCL), are working on the theory for these measurements, which is based on their publication [3]. Since a proper fit function is not known yet, the figure only shows the positions found with the already introduced algorithm. The white, filled circle indicates the zero–field position, if a linear fit is used. We assume that the lowest state is the 22f(0)–state, and the next higher one is the 22g(0). As such the splittings are labeled as $\Delta\omega_\mathrm{f}$ and $\Delta\omega_\mathrm{g}$ accordingly. By adjusting the quantum defect used for the g–state in the simulation such, that the simulation results align well with the measured Stark map, the quantum defect for g is deducible. In figure 5.17 a plot of a theoretically simulated Stark map for 22(0) is shown in the upper plot. The right half indicates the expected transition strength of any line shown based on the accessible states (mainly f–states), whereas the right half does not adjust the color. The line directly below the high–l–manifold is the g–state. Figure 5.17 shows the simulation on top of the measured data for 22(0) in the lower plot. While the alignment is acceptable for fields close to zero, there is a strong misalignment for higher ones. We currently investigate, if for example stray magnetic fields or polarization effects can be made accountable for this. On the other hand it is possible to simulate a "separate" Stark map per value of m_N. The figure has $m_N = 3$, yet higher values show somewhat better alignment. The g–quantum defect has been adjusted to 0.0025 for the shown agreement at zero field. In future discussions these results will be refined.

Coming back to the application as a trace–gas sensor, the shown maps clearly show suitable field ranges. In all maps a good sensing range appears to be somewhere between $0.5\,\mathrm{V\,cm^{-1}}$ to $2\,\mathrm{V\,cm^{-1}}$. While the non–affected line is disturbing when considering the Stark effect, we can actually make use of it in a sensor application, as it reduces the demands on any field control.

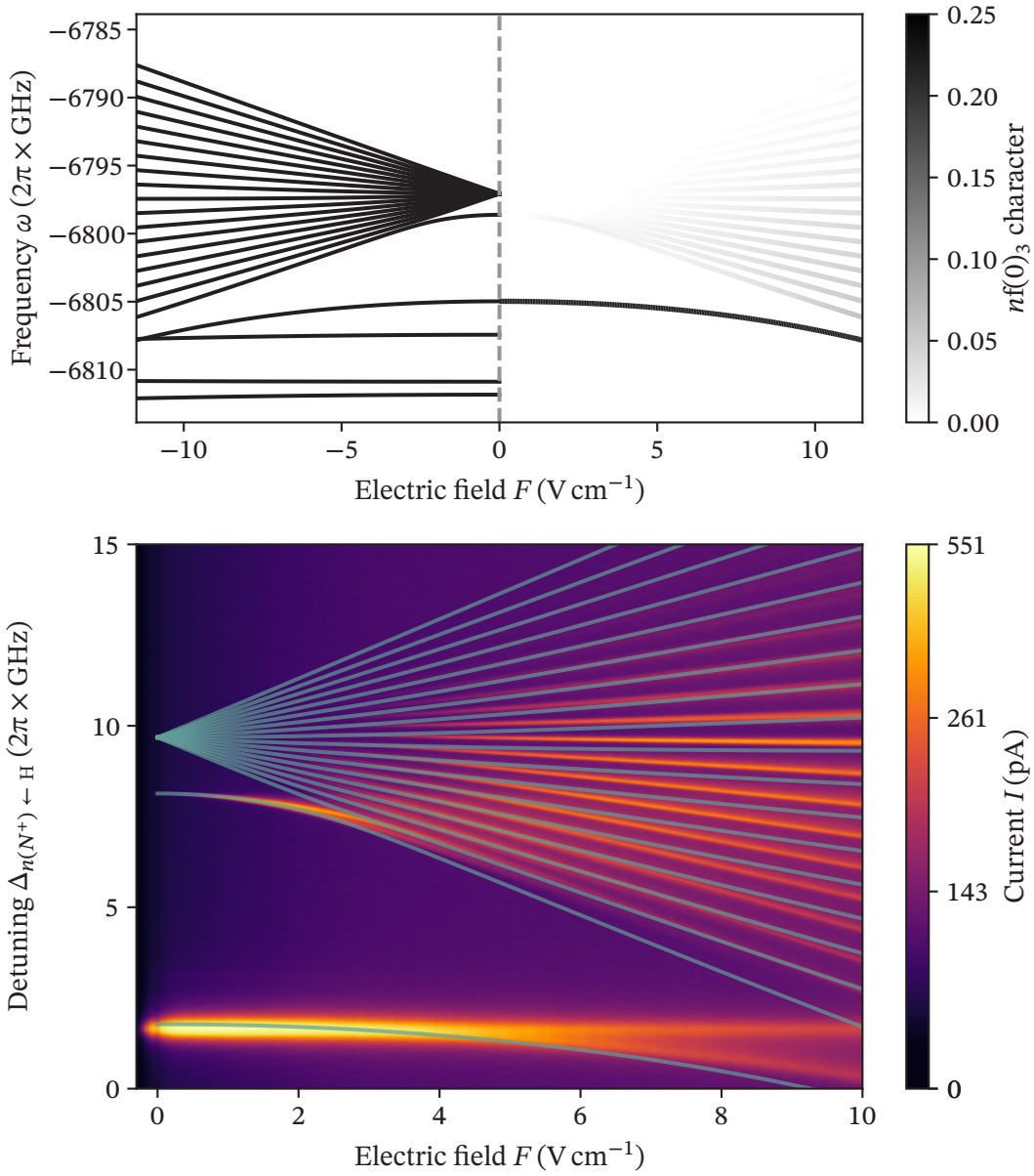

Figure 5.17: Top plot: Theoretically simulated Stark map of 22(0) for $m_N = 3$ in accordance with our excitation scheme. The right half shows the expected transition strength. Here, the f–character of a particular state is visualized. **Bottom plot:** Simulation data on top of our experimental data for 22(0). The agreement for low fields F is already good, whereas for high fields a deviation occurs. It is possible that $m_N = 3$ is wrong, since a better agreement for higher m_N could be seen in first results. However, we do not have any explanation for it yet. The theory data for these plots has been provided by Matt Rayment and Stephen Hogan.

5.4 Collisional shift and broadening of Rydberg lines

This section introduces the frequency shift of the Rydberg line at a constant readout field due to collisions, i. e. scattering of the Rydberg electron with a perturber. Perturbers are other ground state molecules or atoms, in our case not necessarily but possibly of the same species. In general, collisions between a Rydberg molecule or atom and a perturber have an effect on the frequency of the line as well as on the linewidth [70]. The results of this section were summarized in a publication, which is currently under review [25]. Within the scope of developing a trace–gas sensor for NO, the results obtained here give suitable pressure ranges. They allow determining, if the broadening or the frequency shift of the Rydberg line are things to consider.

5.4.1 Collision types

In [70] an overview on possible collision types is given. In contrast to an interaction of a Rydberg atom or molecule with a charged particle, collisions of a Rydberg particle with a neutral particle in its ground state allow treating interactions with the ionic core and the Rydberg electron independently. This can be seen from the dipole–induced dipole interaction scaling with $1/r^6$ (Van-der-Waals), if r is the nuclear separation of perturber and Rydberg particle, as the interaction vanishes if the perturber is outside the orbital radius [70].

If the perturber is a polar molecule (such as NO), the Rydberg electron may interact with the dipole ($\propto 1/r_{\mathrm{sep}}^2$) and quadrupole moments ($\propto 1/r_{\mathrm{sep}}^3$) of the perturber, as well as with the induced moments where the largest electron–induced dipole interaction is scaling $1/r_{\mathrm{sep}}^4$, if r_{sep} is the distance between electron and perturber [70]. On the other hand, for a non–polar perturber, there is no electron–dipole interaction, only quadrupole interaction, which is of shorter range [70]. A distinction is made between elastic and inelastic collisions.

An inelastic collision affects the internal state of both collisional partners. If the perturber is a molecule, different rotational and vibrational states are available. The scattering may now induce a rotational or vibrational change in the molecule. Due to energy conservation the properties of the Rydberg electron have to change as well, i. e. the principal quantum number n and the orbital momentum l are subject to change [70].

In an elastic collision there is only an exchange in translational energy, yet no internal state is changed. As such there may be a change in the phase of the Rydberg electron wave function, i. e. a change in the energy or the frequency of the Rydberg transition.

Perturbers, where elastic collisions are dominant, are rare gases, as an internal state change is almost impossible [70]. Fermi introduced the scattering length a, a unique property of any atom or molecule, and found a formula describing the shift δ_{el} by scattering at the Rydberg electron [21]. There may also be a shift by collisions with the core. For the overall shift one may separate the shifts to

$$\delta = \delta_{\mathrm{ion}} + \delta_{\mathrm{el}} \quad , \tag{5.19}$$

where δ_{ion} is the shift by collisions with the ionic core [70]. This shift is small. Fermi treated both shift types in his paper from 1934 [21].

5.4.2 Elastic collisions and Fermi shift

The alteration in position and shift of spectral lines for Rydberg states in sodium (Na) were already experimentally observed by Amaldi and Segré [22]. In the case of N_2 as perturber only broadening was observed, whereas in the case of hydrogen (H_2) a shift to the blue of the spectral lines for higher pressures was noted. Fermi explained these shifts in [21], and as this theory applies to our results as well a short walk-through is given here, while modern day conventions are used [123–125]. Omont gives a more in–depth treatment in [126]. In his paper, Fermi considers atoms which are in a such highly excited state, that there is a significant amount of neutral perturbers within the orbit of the valence electron. It is claimed that a high principle quantum number justifies the assumption, that the orbit of the single valence electrons contains a significant number of perturbers. The valence electron is subject to two distinguished potentials $U(r)$ and $\sum_i V_i(r)$. The potential [124, 125]

$$U(\boldsymbol{r}) = -\frac{e^2}{4\pi\epsilon_0} \cdot \frac{1}{|\boldsymbol{r}|} \tag{5.20}$$

describes the Coulomb interaction of the core with the valence electron at distance r. The dielectric constant is given by ϵ_0. On the other hand, the potentials

$$V_i = -\frac{1}{(4\pi\epsilon_0)} \frac{\alpha e^2}{2\,|\boldsymbol{R_i} - \boldsymbol{r}|^4} \tag{5.21}$$

take the interaction between perturber and valence electron into account ("potential well" [125]). Here, α is the polarizability. The perturbing atom is at position $\boldsymbol{R_i}$. The Schrödinger equation of the valence electron then reads

$$\left(-\frac{\hbar^2}{2m}\nabla^2 + U(\boldsymbol{r}) + \sum_i V_i(\boldsymbol{r})\right)\psi(\boldsymbol{r}) = E\psi(\boldsymbol{r}) \quad . \tag{5.22}$$

The perturber atoms or molecules are treated as one species, and are considered neutral. The effect of the potential U is significant, if the electron is close-by. On the other hand, V_i is deep, yet narrow in comparison to the de-Broglie wavelength λ_{dB} of the electron. Thus, the wave function ψ of the electron is locally perturbed, yet regular otherwise. One can make use of this by introducing $\overline{\psi}$, which is the mean value of ψ in a small volume compared to λ_{dB}, yet big enough to include a significant amount of perturber particles.

Adjusting the Schrödinger equation yields

$$\frac{\hbar^2}{2m}\nabla^2\overline{\psi} + (E-U)\overline{\psi} - \overline{\sum_i V_i\psi} = 0 \quad . \tag{5.23}$$

If the wave function is locally perturbed by V, the perturbation only depends on r, thus one may introduce $u(r) = r \cdot \psi$, which fulfills approximately

$$\frac{\hbar^2}{2m}\partial_r^2 u(r) = -V(r)u(r) \quad . \tag{5.24}$$

Leaving the potential well means $\psi = \overline{\psi}$, i.e. the wave function becomes linear. This justifies to set the right-hand side of (5.24) to zero, yielding

$$u(r) = (a+r)\overline{\psi} \quad , \tag{5.25}$$

introducing the scattering length a. On the other hand integration of (5.24) for a single atom in Volume V_0 [124] and using (5.25) yields [123]

$$\overline{V}\overline{\psi} = \frac{4\pi}{V_0}\int V(r)U(r)r\mathrm{d}r \quad , \tag{5.26a}$$

$$\overline{V}\overline{\psi} = -\frac{2\pi\hbar^2}{m}a\overline{\psi} \quad , \tag{5.26b}$$

Moving on, we can adjust this to not a single but many perturbers as

$$\sum_i V_i = -\frac{2\hbar^2\pi a N}{m}\psi \quad , \tag{5.27a}$$

$$\delta = \frac{2\hbar^2\pi a}{m}\cdot N \quad , \tag{5.27b}$$

which introduces shift δ in dependence of density N. A sketch which reproduces a figure in Fermi's paper [21] and explains the approximations graphically is shown in figure 5.18.

It is typical to give the scattering length a in units of the Bohr radius a_0, thus equation (5.27b) can be written as

$$\delta = \frac{2\pi\hbar^2}{m} a a_0 N \quad . \tag{5.28}$$

This makes the scattering length a dimensionless.

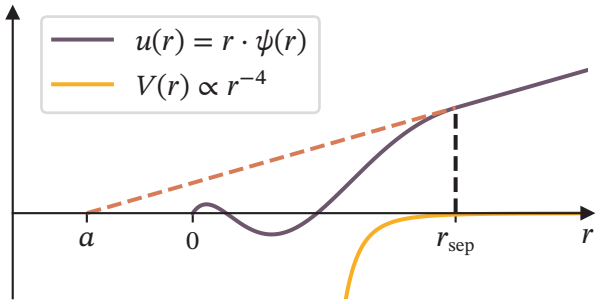

Figure 5.18: Sketch reproduced from [21, 124] explaining the approximation made by Fermi. The potential $V(r)$ is short range and defines the potential well. Outside the potential well, $r > r_{\text{sep}}$, the wavefunction $u(r)$ becomes linear. We continue the linearity into the potential well, $u(r) = (a + r)\overline{\psi}$, and the intersection point on the x–axis is the scattering length a.

5.4.3 Collisional broadening

In subsection 3.4.1 different broadening contributions including collisional broadening were already introduced in general. The broadening cross-section σ^{b} for Rydberg particles can be refined and may be composed out of the sum of three individual contributions [70],

$$\sigma^{\text{b}} = \frac{1}{2}\left(\sigma^{\text{b}}_{\text{el}} + \sigma^{\text{b}}_{\text{inel}} + \sigma^{\text{b}}_{\text{ion}}\right) \quad . \tag{5.29}$$

In equation (5.29) the elastic cross-section $\sigma^{\text{b}}_{\text{el}}$ takes account of the interaction between Rydberg electron and perturber, the inelastic cross-section $\sigma^{\text{b}}_{\text{inel}}$ considers depopulation processes and $\sigma^{\text{b}}_{\text{ion}}$ is the Rydberg ion–perturber cross-section. We expect the ion–perturber cross-section to contribute less than the others.

5.4.4 Evaluation

The measurement data is acquired as shown in subsection 5.2.4. The field is in all cases set to about 11.9 V cm^{-1}, and the laser scanned such, that the high–l–manifold is centered.

Apart from the general evaluation shown in subsection 5.2.4 the data is evaluated further in the following way. To track the width and the shift of the signal, it needs to be fitted. Since the broadening of the line becomes larger the higher the pressure, the fitting routine starts from low pressure and works its way towards higher pressures. As fit function a Voigt (see equation (3.14)) is used. For a justification why a Voigt and not a Lorentzian was chosen, refer to the next section. As the peaks broaden they start to overlap increasingly, which means that the baseline changes significantly for higher pressures. As such a polynomial function of second order is added to the overall fit function, i. e.

$$f_{\text{fit}}(\omega, \gamma, \sigma, a, b, c) = f_{\text{Voigt}}(\omega, \gamma, \sigma) + a\omega^2 + b\omega + c \quad . \tag{5.30}$$

Special care is taken such, that the variables a, b and c stay in small bounds to only alter the FWHM γ and position ω_0 negligibly. The fitted peaks are the centered line, i. e. the line not affected by the Stark effect, and the lines left and right of it. These two are only fitted for cross–checking, but not used for evaluation. In short, the sequence is:

1. The user chooses a trace where the peaks are clearly distinguishable. This is not always the trace at lowest pressure.
2. By clicking the user sets the positional start parameters.
3. The algorithm starts at this pressure, and fits “in both directions”, i. e. to higher and lower pressures step by step. The fit results of the previous step are used as initial parameters. An example for a fitted line is shown in figure 5.19.
4. When all lines are fitted, the positions and widths of the central line are extracted from the result. We calculate the density N by using the ideal gas law, thus
$$N = \frac{p}{k_{\text{B}} T} \quad . \tag{5.31}$$
The temperature is 293 K.
5. As the shift is a relative quantity, we subtract the mean of the first 5 position values at low pressures.

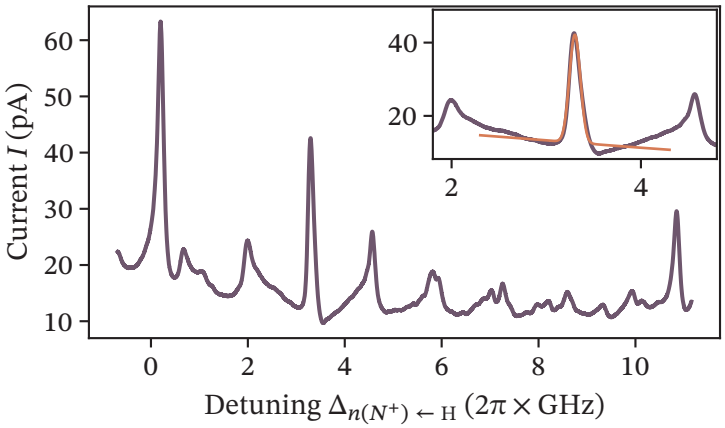

Figure 5.19: Example for the fit of the centered line in a density–shift measurement. Here the state 32(4) at a density of $N_{\mathrm{NO}} \approx 1.91(57) \cdot 10^{15}\,\mathrm{cm}^{-3}$ is shown. As can be seen, the fit is acceptable, if used for the extraction of width and position, however, the baseline is not fitted accurately. The given uncertainty is explained in subsection 5.4.5.

5.4.5 Results

The results for relative shift δ and FWHM γ extracted from the previously explained Voigt fit are shown in figure 5.20. We calculate the FWHM in accordance with equation (3.15). At first, we'll look at the observed broadening. As introduced in section 3.4 several broadening mechanisms contribute to the overall broadening, such as residual Doppler broadening, power broadening, transit–time broadening and any broadening due to polarization effects. While no definite values can be given in the case of NO, a lower bound for the Doppler broadening is $\gamma = 2\pi \times 8\,\mathrm{MHz}$ as introduced in equation (3.11). The shown linear behavior in figure 5.20 additionally suggests that collisional effects are dominating, at least for higher densities N. When considering the molecular orbital diagram of NO in figure 2.4 and transferring to N_2, the similarity suggests similar broadening contributions. On top, any molecule has the additional freedoms of vibration and rotation. The population of rotational levels was given in equation (2.30) and plotted in figure 2.6 for ground state molecules of NO at room temperature. Here, all rotational levels from $J = 0.5$ to $J = 19.5$ have a probability above 1 % indicating significant contribution. This expectation is fulfilled by both measurements in figure 2.4, though the overall slope is lower for N_2. In contrast, any atom would lack these additional contributions [23, 24].

Let us analyze the shift δ by both perturbers next. For collisions of NO perturbed by itself, a linear shift to the red for all states is observed. If however Rydberg states of NO are perturbed by N_2, only a slight shift to the blue is visible. A linear shift is a signature to elastic scattering as introduced by Fermi [21] and seen in equation (5.28).

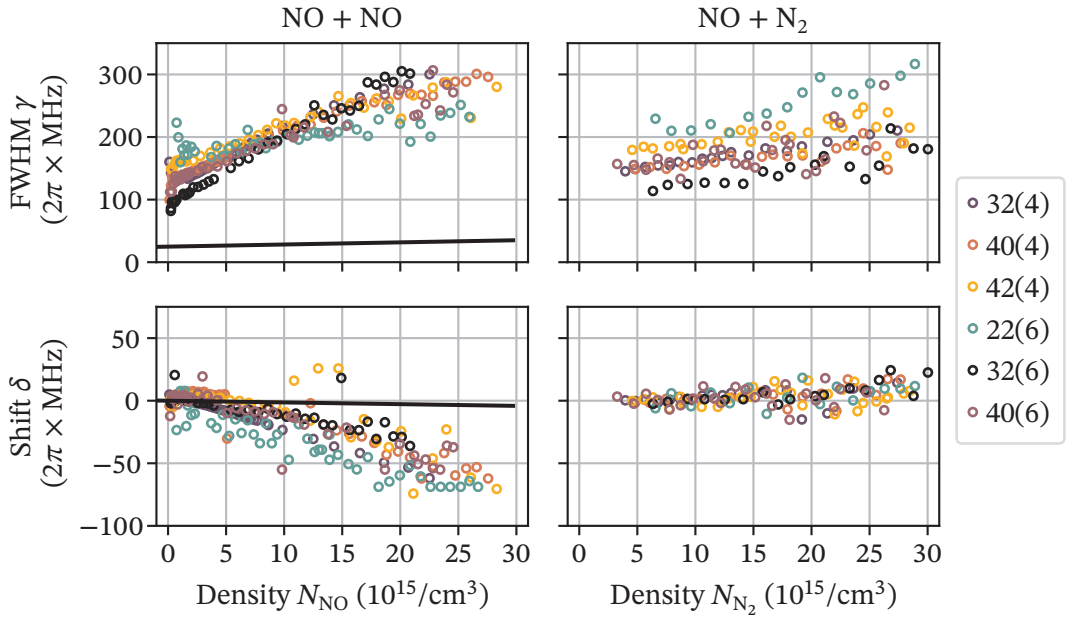

Figure 5.20: Fit results of the FWHM γ and relative shift δ for Rydberg states of NO perturbed by either NO itself or N_2. We performed measurements for different Rydberg states $n(N^+)$ of NO. As the shift δ is relative, its position is moved such, that the first couple of points are close to zero. The additional line in the left column denotes contributions by $H\,^2\Sigma^+$ and is explained in the text. The legend gives the Rydberg state labeled as $n(N^+)$.

In contrast to an elastic collision, inelastic collisions do not change the phase of the Rydberg electron's wavefunction. While we can say, that elastic scattering appears to dominate for perturbations by NO, a similar statement considering inelastic collisions is difficult when referring to N_2.

While elastic scattering is expected for rare gases such as Ar due to their closed shell structure [23, 24], such an argument cannot be made for the considered molecule. By referring to the molecular orbital diagram again, see figure 2.4, one might argue that elastic collisions are likely due to a degenerate level in the anti-bonding 2π orbital. This explanation is supported by the fact, that the short–lived molecule NO^- even exists in biological processes [127]. On the other hand similar reasoning is possible for N_2.

As already mentioned, a Voigt function was fitted to the measurement results. As collisional broadening is of homogeneous type, a Lorentzian shape would have been the expectation. However, it turned out there is significant Gaussian contribution and a Voigt suits the measurement results better. An explanation is the already observed shift on the second transition, $H\,^2\Sigma^+ \leftarrow A\,^2\Sigma^+$. Here, the UV transition

$A\,^2\Sigma^+ \leftarrow X\,^2\Pi_{3/2}$ was locked, and the second transition scanned. The density was increased incrementally. A plot is shown in figure 5.21. Both γ and δ show a linear behavior, and their overall magnitude is way smaller in comparison to what was observed in figure 5.20. A linear fit to both results allows classifying this contribution by additionally taking care of the wavevector mismatch like [128]

$$k_{\text{mis}} \equiv \frac{k_1 - k_2 - k_3}{k_1 - k_2} = \frac{1/226\,\text{nm} - 1/540\,\text{nm} - 1/835\,\text{nm}}{1/226\,\text{nm} - 1/540\,\text{nm}} \approx 0.53 \quad . \tag{5.32}$$

The scaled fitted functions are

$$\begin{aligned} \frac{\gamma(N)}{2\pi} &\approx k_{\text{mis}} \cdot \left[0.64 \cdot 10^{-15}\,\text{MHz}\,\text{cm}^3 \cdot N + 46.53\,\text{MHz}\right] \\ &\approx 0.34 \cdot 10^{-15}\,\text{MHz}\,\text{cm}^3 \cdot N + 24.87\,\text{MHz} \quad , \end{aligned} \tag{5.33a}$$

$$\begin{aligned} \frac{\delta(N)}{2\pi} &\approx k_{\text{mis}} \cdot \left[-0.26 \cdot 10^{-15}\,\text{MHz}\,\text{cm}^3 \cdot N\right] \\ &\approx -0.14 \cdot 10^{-15}\,\text{MHz}\,\text{cm}^3 \cdot N \quad , \end{aligned} \tag{5.33b}$$

and are plotted as solid line next to measurements of NO perturbed by NO in figure 5.20. As can be seen, their contribution to the overall shift and broadening is negligible, yet they might explain the necessity of a Voigt function.

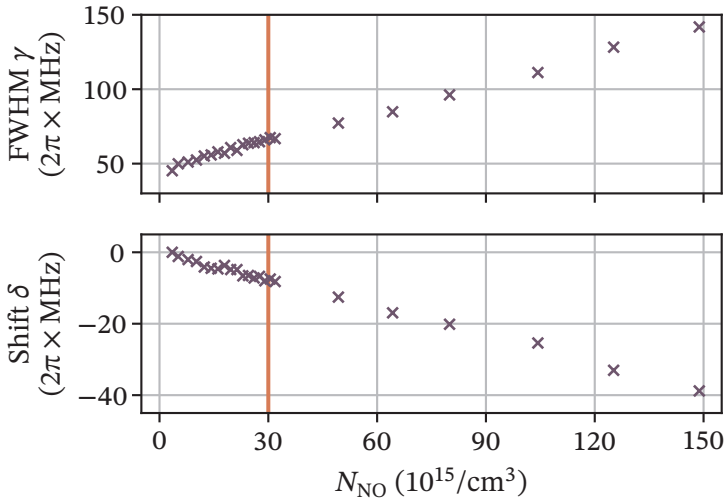

Figure 5.21: FWHM γ and relative shift δ of the signal obtained from the $H\,^2\Sigma^+ \leftarrow A\,^2\Sigma^+$ transition. Here, the Rydberg laser was turned off and only the $H\,^2\Sigma^+ \leftarrow A\,^2\Sigma^+$–laser scanned. The vertical line corresponds to the maximum density measured in figure 5.20.

As a final step the results presented will be compared with results from the literature. However, to our knowledge only literature on the shift and broadening of spectroscopic lines in alkalis exist. Füchtbauer et al. [23] and Weber et al. [24] both measured the shift of alkalis being subject to a perturbing rare gas. Füchtbauer considered shifts of the spectroscopic lines of Na and K by Ne, He and Ar, whereas Weber investigated the shift of nD and nS lines of Rb by Xe, He and Ar. Weber introduced the broadening rate γ/N and shift rate δ/N. Some of their results are given for comparison in table 5.3

To extract these rates from our measurement results, the shift of the individual states $n(N^+)$ is fitted with linear functions. For the broadening as function

$$f_{\text{fit}}(N) = \sqrt{\text{offset}^2 + \left(\frac{\gamma}{N} \cdot N\right)^2} \quad , \tag{5.34}$$

is used, which accounts for the additional broadening contributions in the low densities. The fit results are given in table 5.4 and additionally plotted in figure 5.22. Here an error estimate is assigned to the results, which has its origin in the used pressure gauges (Pfeiffer PKR 251). They have an absolute pressure uncertainty of 30 %. In comparison, our lock error of $\Delta\omega_{\text{Rydberg}} = 2\pi \times 2.5\,\text{MHz}$ is negligible. The error is also resulting in the error bars in figure 5.22. When comparing with [23, 24], the broadening rate γ/N is an order of magnitude higher, and the shift rate for the measurements of NO perturbed by NO differs by a factor of two. Both results together indicate, that additional processes are present in molecules.

Table 5.3: Broadening rate γ/N and shift rate δ/N in $10^{-15} \cdot 2\pi \times \text{MHz}\,\text{cm}^3$ for some exemplary measurements taken by Weber et al. [24] and Füchtbauer et al. [23] in alkalis. For Füchtbauer values of K perturbed by Ar are taken, and for measurements by Weber values of nS–Rydberg states of Rb perturbed by Ar are given. The values of Füchtbauer were calculated by using the ideal gas law.

	Füchtbauer et al. K + Ar	Weber et al. (nS) Rb + Ar	
n	δ/N	δ/N	γ/N
21	-10.97	-4.76	1.46
23	-10.94	-4.94	1.56
25	-11.34	-5.02	1.66
27		-5	1.77
29		-5	1.8
33		-5.16	1.36
35		-5.04	1.36

Table 5.4: Extracted broadening rate γ/N and shift rate δ/N by fitting the measurement results in figure 5.20. The fit functions are explained in the text. For all values the unit is $10^{-15} \cdot 2\pi \times \mathrm{MHz\,cm^3}$. The used pressure gauges have an uncertainty of 30 % in terms of absolute pressure, and as such give the largest error contribution.

State	NO + NO		NO + N_2	
$n(N^+)$	γ/N	δ/N	γ/N	δ/N
32(4)	13(4)	−2.8(8)	5.5(16)	0.25(8)
40(4)	11(3)	−2.5(7)	4.0(12)	0.57(17)
42(4)	9.1(27)	−2.1(6)	4.0(12)	0.19(6)
22(6)	7.5(23)	−2.7(8)	9.2(28)	0.52(16)
32(6)	15(4)	−1.4(4)	4.9(15)	0.82(25)
40(6)	10(3)	−2.3(7)	6.1(18)	0.089(27)

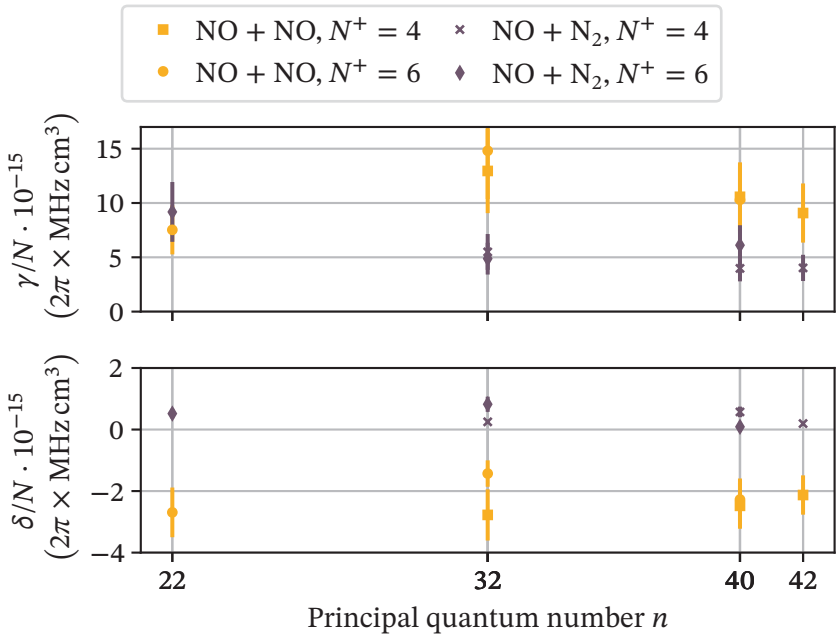

Figure 5.22: Broadening rate γ/N and shift rate δ/N of the measurements performed in NO as seen in figure 5.20. An uncertainty of 30 % in the pressure yields the error bars. Some bars are below the markers.

5.5 Outlook

Finally, let us consider the found results for an application as a trace–gas sensor again. The trade–off at hand is the reduce in excitation efficiency due to broadening, yet an increase in free charges with increasing density. On top, we expect the Rydberg line at a certain frequency position, when used as a sensor. The found results suggest to use low densities, which translates to 10th of μbar of NO in our setup. However, it is certainly advisable to perform similar characterization experiments as introduced in subsection 4.3.1 for the new cell.

6 Conclusion and outlook

6.1 Summary

In this work we investigated Rydberg states in nitric oxide (NO) at room temperature based on the electrical detection of free charges resulting from collisions.

The experimental setup is made of four different components, the gas mixing unit (GMU), the optical setup, the frequency–stabilization setup and the measurement glass cell. The GMU enables the experimentalist to use either pure NO or a mixture of NO and nitrogen (N_2) at a defined pressure. The gas flows through the glass cell, where we excite NO to a Rydberg state $n(N^+)$. For the excitation a three–photon excitation scheme based solely on continuous–wave (cw) laser systems is used. The lasers are stabilized to the frequency–stabilization setup. After the excitation the molecules ionize by collisions with the background gas. Then we can detect these free charges by using the built-in readout electronics. Within the scope of this work several different measurement cells were developed. Two were introduced in this thesis. Any measurement cell features a custom–designed printed circuit board (PCB) with readout electronics on top, and an electrode on the bottom plane pointing to the excitation volume. The readout electronics were designed in cooperation with the Institute of Smart Sensors (IIS), while advice was given at all stages by the Institute for Large Area Microelectronics (IGM). The PCB uses a resistive transimpedance amplifier (TIA)–circuit, and an additional guard ring to reduce the effects of any leakage currents. The bottom electrode is realized with a copper plate. We guide the free charges to the electrodes by applying a potential to them. Typically, we measure currents in the pA–regime.

At the start of this work's project the accessible Rydberg states by the employed excitation scheme were not known. We learned that mainly f–states are accessible, which is a partial result of the different characters of the underlying states. For example, the H $^2\Sigma^+$–state has both s– and d–character [47]. It is the final state before exciting to a Rydberg state. A scan of the Rydberg laser over a large wavelength enabled us to obtain the spectrum of two distinct Rydberg series. In general, the diatomic nature of NO yields different Rydberg series at different rotational quantum numbers N^+ of the ionic core. The effect of N^+ can be understood as an "offset"

to a typical series scaling with $1/n^2$, where n is the principal quantum number. The spectrum obtained showed the $N^+ = 3$ and $N^+ = 5$ series. This was a result of the branches selected beforehand, which has been the $P_{12}(5.5)$–branch on the $A\,^2\Sigma^+ \leftarrow X\,^2\Pi_{3/2}$ transition and the $R_{11}(4.5)$–branch on the $H\,^2\Sigma^+ \leftarrow A\,^2\Sigma^+$ transition. By using the Rydberg formula and the difference in frequency between neighboring states, it was possible to label a particular Rydberg state with principal quantum number n as $n(N^+)$. Since two different series of N^+ were visible, the Rydberg formula could again be used two calculate the frequency difference between the relative thresholds of these series. A rather small deviation in comparison to the theory of diatomic molecules showed, that we understand our excitation scheme, and are able to pick branches such, that a particular Rydberg state $n(N^+)$ is accessible. Up to this point we successfully showed the excitation of Rydberg states from $N^+ = 0$ to $N^+ = 6$.

In a next step we took a look at the Stark effect in Rydberg states of NO. In general the Stark effect is the shift and splitting of energy levels in molecules or atoms due to an applied electric field. At first, we compared a Stark map obtained with the old measurement cell with another obtained with the new one. The difference between old and new cell were mainly the homogeneity of the electric field as well as the rise time of the readout electronics. The results clearly showed the importance of the circuit's time constant. While an additional capacity in the old circuit was a rather natural choice to increase the TIA's bandwidth, it turned out to be a road blocker for the actual measurement. The new cell created was designed such, that both the rise time was minimized, and the homogeneity of the electric field maximized. This was based on a proper numerical and experimental analysis [120, 122]. Such Stark effect measurements may serve as a test of the electric field in future cell designs. Since we are using cw excitation of NO and the already mentioned readout technique, the resolution we obtain in our measurement is to our knowledge unmatched. Our relative frequency reference has an uncertainty of only $2\pi\times2.5$ MHz, and the full width at half maximum (FWHM) of the Rydberg transition is only about $\gamma_{n(N^+)\leftarrow H} \approx 2\pi \times 130\,\mathrm{MHz}$. This also allows a theoretical investigation.

The theory for these measurements is currently developed and refined by our cooperation partners Stephen Hogan and Matthew Rayment at the University College London (UCL). At this point there are literature values for the quantum defect of up to f–states available [3], yet only a range can be given for the quantum defect of g–states [19, 20]. We are quite certain, that we can differentiate the g–state from the f–state and the high–l–manifold, at least for the $N^+ = 0$ series. By adjusting the g–quantum defect to 0.0025 we obtained the best results, though we currently don't fully understand, which m_N is appropriate for our state measurements. Here, m_N is the magnetic quantum number of a Hund's case (d). While the theoretical results

show a good agreement for low fields, they diverge for higher fields. We are confident that a better understanding will be available in the future.

Finally, I presented measurements on the collisional shift and broadening of Rydberg lines in NO. An elastic collision of a perturber with Rydberg electron shifts the line with increasing density. This kind of shift is named Fermi shift, since Fermi explained this theoretically already in 1934 [21]. On the other hand, inelastic collisions do not change the phase of the electronic wavefunction, but instead change a quantum number in the Rydberg state. This doesn't shift the Rydberg line. In our experiment we considered the shift and broadening of Rydberg states in NO being subject to either an increasing density of NO itself, or N_2. In both cases, a similar broadening of the Rydberg line was visible, ranging from a FWHM of $\gamma = 2\pi \times 100\,\mathrm{MHz}$ to $\gamma = 2\pi \times 300\,\mathrm{MHz}$ within the considered density range. However, only perturbations of NO with NO showed a clear shift to the red. For perturbations by N_2 a rather small shift to the blue was visible. This indicates, that for perturbations by NO elastic collisions dominate, whereas such a statement could not be made for perturbations by N_2. When comparing the broadening and shift rate to literature values taken with alkalis [23, 24], we observe an order of magnitude larger broadening, whereas the shift is reduced by a factor of two. We attributed the differing broadening rate to the additional degrees of freedom in a molecule, such as vibration and rotation.

6.2 Outlook

In the short–term future we are going to refine our theory on the Stark effect measurement together with our cooperation partners. We are confident, that this may not only allow us to nail down the g–quantum defect of NO to a new precision, but may also yield further insights.

In the long-term future the project's goal is to set up a trace–gas sensor for NO. The measurements presented in this work may be used as a reference to suitable density and field ranges. However, the currently used glass cell is optimized for the homogeneity of the electric field, but not for sensitivity. New cell designs would allow improving the sensitivity, and subsequently enable us to measure the smallest concentrations of NO. The application of an application–specific integrated circuit (ASIC) developed at the IIS may allow us to focus on the cell design completely, since its properties are advantageous for our setup. It would be beneficial to agree upon standardized quantifications of the signal–to–noise ratio (SNR) and sensitivity, as well as the characterization of the overall noise in new designs. Apart from the medical application, in a wider context, an improved sensitivity may enable us to detect the theoretically predicted bimolecules in NO [35].

Danksagung

Der erfolgreiche Abschluss meiner Promotion wäre wohl nicht ohne zahlreiche Weggefährten möglich gewesen.

Zuallererst möchte ich Tilman Pfau für die Möglichkeit zur Promotion an seinem Institut danken. Zahlreiche spannende Diskussionen und Ideen haben die Motivation über die letzten Jahre hochgehalten. Insbesondere die Möglichkeit bei Problemen und Fragen jederzeit vorbeischauen zu können, habe ich sehr zu schätzen gewusst.

Bei Prof. Jens Anders bedanke ich mich für die Übernahme des Mitberichtes, und bei Prof. Mathias Scheurer für die Übernahme des Prüfungsvorsitzes.

Natürlich muss ich mich auch bei Harald Kübler bedanken. Das freundschaftliche Miteinander, die immer wieder neuen Einfälle und Vorschläge, und natürlich die generelle Projektidee haben das Projekt mehr als nur vorwärtsgebracht. Ich bin dankbar, dass es jederzeit ein gemeinsames Arbeiten war.

Prof. Jens Anders und Prof. Norbert Frühauf sowie Dr. Patrick Schalberger möchte ich dafür danken, dass Sie eine fachübergreifende Kooperation ermöglicht haben. Die Ergebnisse dieser Arbeit wären ohne eine enge Zusammenarbeit mit Ihren beiden Instituten der Elektrotechnik nicht möglich gewesen.

I would like to thank especially Prof. Stephen Hogan and Matthew Rayment. I am more than happy, that we were able to establish an ongoing cooperation, and I am grateful, that my lack of molecular knowledge was tackled with patience in several meetings. I am looking forward to our future discussions.

Additionally, I have to thank Prof. Hossein Sadeghpour, who was always happy to discuss recent experimental results and gave hints, how they could align with the theory behind. And, I have to thank Prof. Ed Grant, who invited me for a stay over at the end of my Master's thesis, and was able to transfer his enthusiasm on molecular Rydberg physics to me.

Wenn wir zu meinen Kollegen kommen, steht natürlich Patrick Kaspar an vorderster Stelle. Ich denke, die Jahre gemeinsamer Arbeit haben zusammengeschweißt, und ich bin dankbar, dass wir trotz so zahlreicher Ausfälle am Experiment es immer wieder geschafft haben, uns aufzurappeln, und weiterzumachen. Die stoische Ruhe, mit

der du fast alles angegangen hast, war für den Erfolg des Experiments entscheidend. Und deine akribische Dokumentation der Ergebnisse hat glücklicherweise dafür gesorgt, dass ich auch alte Messergebnisse jetzt beim Schreiben verwerten konnte.

Als Nächstes gilt ein großer Dank Yannick Schellander. Ich halte es für ein großes Glück, dass direkt mein erster Masterstudent zu einem guten Freund geworden ist, und auch jetzt immer noch Teil des QNOSE–Teams ist. In den letzten Jahren hast du mehr als einmal dafür gesorgt, dass ich hier am Projekt weitergemacht habe.

Ein großer Dank gehört auch meinen weiteren Studenten. Mit Philipp Neufeld konnte ich wesentlich Fortschritte beim Verständnis unseres Anregungsschemas erzielen. Und Alexander Trachtmann, welcher das Experiment exzellent beherrscht, hat alle diesjährigen relevanten Messungen durchgeführt. Außerdem Ettore Eder und Florian Anschütz, die in ihrer Arbeit wesentlich zum Verständnis der Zelleigenschaften und der Auslesemethodik beigetragen haben. Generell hatte ich wohl das große Glück, dass alle meine Studenten über das übliche Maß hinaus gegangen sind.

Weiterhin gilt mein Dank Max Mäusezahl. Ohne dich gäbe es kein funktionierendes Lock–Setup. Du bist bei Fragen jeglicher physikalischer Art immer ein guter Ansprechpartner.

Ein wesentlicher Teil meiner Arbeit hat sich mit dem Design der Glaszelle befasst. Mein Ansprechpartner am IIS war zunächst Lars Baumgärtner, und anschließend Philipp Hengel. Mit euch beiden habe ich wirklich gerne beim Erarbeiten an einer besseren Ausleseelektronik zusammengearbeitet.

Und eine Glaszelle braucht auch einen Glasrahmen. Immer wieder neue Formen und Ideen wurden großartig von unserem Glasbläser Frank Schreiber umgesetzt. Ich bin wirklich froh, dass das so oft so kurzfristig, und gleichzeitig professionell ging.

Mit Kati Kriesch haben wir wohl die bestmögliche Person in unserer Verwaltung sitzen. Danke, dass du mir immer wieder verwaltungstechnische Aufgaben entweder erleichtert, oder gleich ganz abgenommen hast.

Ein Dank gilt auch den Korrektoren meiner Arbeit — Yannick Schellander, Lars Baumgärtner, Max Mäusezahl, Christian Hölzl, Matthias Schmidt, Alexander Trachtmann, Ettore Eder, Florian Anschütz und Harald Kübler.

Abschließend möchte ich mich noch bei meiner Familie bedanken. Ich bin sehr dankbar, dass ihr die gesamte Zeit des Studiums und der Promotion hinter mir gestanden habt, und insbesondere dann aufbauend auf mich eingewirkt habt, wenn es mal wieder nicht so lief.

Publications and supervised theses

Publications

- F. Munkes, A. Trachtmann, P. Kaspar, F. Anschütz, P. Hengel, Y. Schellander, P. Schalberger, N. Fruehauf, J. Anders, R. Löw, T. Pfau, H. Kübler: Collisional shift and broadening of Rydberg states in nitric oxide at room temperature (2023), https://doi.org/10.48550/arXiv.2310.18256
- M. Mäusezahl, F. Munkes, R. Löw: Tutorial on locking techniques and the manufacturing of vapor cells for spectroscopy, *in preparation*
- Y. Schellander, M. Winter, M. Schamber, F. Munkes, P. Schalberger, H. Kuebler, T. Pfau, N. Fruehauf: Ultraviolet photodetectors and readout based on a-IGZO semiconductor technology, Journal of the Society for Information Display (2023), https://doi.org/10.1002/jsid.1202
- P. Kaspar, F. Munkes, P. Neufeld, L. Ebel, Y. Schellander, R. Löw, T. Pfau, H. Kübler: Doppler-free high-resolution continuous-wave optical UV spectroscopy on the $A\,^2\Sigma^+ \leftarrow X\,^2\Pi_{3/2}$ transition in nitric oxide, Phys. Rev. A 106, 062816 (2022), https://doi.org/10.1103/PhysRevA.106.062816

Theses

Bachelor's theses:

- Joshua Fabian: Design einer elektrisch kontaktierten Durchflusszelle zur Detektion von Ionisationsströmen von Rydbergzuständen Stickstoffmonoxids (2020)
- Florian Anschütz: Optimierung des Messsignals eines Spurengassensors für Stickstoffmonoxid mittels einer zweistufigen Lock-In-Technik (2023)
- Ettore Eder: Entwicklung und Optimierung des elektrischen Feldes in einer Durchflusszelle zur Detektion von Rydbergzuständen in Stickstoffmonoxid (2023)

Master's theses:

- Yannick Schellander: Ionization current measurements of Rydberg states in nitric oxide created by continuous-wave three-photon excitation (2020)
- Philipp Neufeld: Collisional ionization of Rydberg states in nitric oxide (2022)
- Alexander Trachtmann: *Working title:* Optimization of the electrical Rydberg signal for a nitric oxide trace-gas sensor, *to be submitted in December 2023*

References

[1] A. Ehresmann et al. “CO Rydberg series converging to the D and C states observed by VUV-fluorescence spectroscopy.” In: *Journal of Physics B: Atomic, Molecular and Optical Physics* 30.8 (Apr. 1997), p. 1907. DOI: 10.1088/0953-4075/30/8/009. URL: https://dx.doi.org/10.1088/0953-4075/30/8/009 (cit. on pp. i, 1).

[2] M. Komatsu et al. “Rotational structure and dissociation of the Rydberg states of CO investigated by ion-dip spectroscopy.” In: *The Journal of Chemical Physics* 103.7 (Aug. 1995), pp. 2420–2435. ISSN: 0021-9606. DOI: 10.1063/1.469665 (cit. on pp. i, 1).

[3] M. H. Rayment and S. D. Hogan. “Quantum-state-dependent decay rates of electrostatically trapped Rydberg NO molecules.” In: *Physical Chemistry Chemical Physics* 23.34 (2021), pp. 18806–18822. DOI: 10.1039/d1cp01930a (cit. on pp. i, iii, 1, 15, 20, 25–29, 31, 86, 95, 106, 109, 111, 126).

[4] R. Wang et al. “mm-wave Rydberg–Rydberg transitions gauge intermolecular coupling in a molecular ultracold plasma.” In: *The Journal of Chemical Physics* 157.6 (Aug. 2022). DOI: 10.1063/5.0083684 (cit. on pp. i, iii, 1, 20, 22, 23, 33, 106).

[5] A. K. Mohapatra, T. R. Jackson, and C. S. Adams. “Coherent Optical Detection of Highly Excited Rydberg States Using Electromagnetically Induced Transparency.” In: *Phys. Rev. Lett.* 98 (11 Mar. 2007), p. 113003. DOI: 10.1103/PhysRevLett.98.113003 (cit. on pp. i, 1).

[6] J. A. Sedlacek et al. “Atom-Based Vector Microwave Electrometry Using Rubidium Rydberg Atoms in a Vapor Cell.” In: *Phys. Rev. Lett.* 111 (6 Aug. 2013), p. 063001. DOI: 10.1103/PhysRevLett.111.063001 (cit. on pp. i, 1).

[7] D. Barredo et al. “Electrical Readout for Coherent Phenomena Involving Rydberg Atoms in Thermal Vapor Cells.” In: *Physical Review Letters* 110.12 (Mar. 2013). DOI: 10.1103/physrevlett.110.123002 (cit. on pp. i, ii, 1).

[8] R. Daschner et al. “Fabrication and characterization of an electrically contacted vapor cell.” In: *Optics Letters* 37.12 (June 2012), p. 2271. DOI: 10.1364/ol.37.002271 (cit. on pp. ii, 1).

[9] R. Daschner et al. “Triple stack glass-to-glass anodic bonding for optogalvanic spectroscopy cells with electrical feedthroughs.” In: *Applied Physics Letters* 105.4 (July 2014), p. 041107. DOI: 10.1063/1.4891534 (cit. on pp. ii, 1).

[10] R. Daschner. “Addressable Rubidium vapor cells for optical and electrical read-out of Rydberg excitations.” PhD thesis. 5th Institute of Physics, University of Stuttgart, 2015 (cit. on pp. ii, 1).

[11] J. Schmidt. “A trace gas sensor based on Rydberg excitations.” PhD thesis. 5th Institute of Physics, University of Stuttgart, 2019 (cit. on pp. ii, 2, 51, 53).

[12] J. Schmidt et al. “A transimpedance amplifier based on a LTPS process operated in alkali vapor.” In: *2017 24th International Workshop on Active-Matrix Flatpanel Displays and Devices (AM-FPD)*. July 2017, pp. 296–298 (cit. on pp. ii, 2).

[13] J. Schmidt et al. “A transimpedance amplifier based on an LTPS process operated in alkali vapor for the measurement of an ionization current.” In: *Quantum Technologies 2018*. Ed. by A. J. Shields, J. Stuhler, and M. J. Padgett. SPIE, May 2018. DOI: 10.1117/12.2309655 (cit. on pp. ii, 2).

[14] J. Schmidt et al. “Proof of concept for an optogalvanic gas sensor for NO based on Rydberg excitations.” In: *Applied Physics Letters* 113.1 (July 2018), p. 011113. DOI: 10.1063/1.5024321 (cit. on pp. ii, 2, 4, 51).

[15] J. Schmidt et al. “An optogalvanic gas sensor based on Rydberg excitations.” In: *Journal of Physics B: Atomic, Molecular and Optical Physics* 53.9 (Mar. 2020), p. 094001. DOI: 10.1088/1361-6455/ab728e (cit. on pp. ii, 2).

[16] P. Kaspar. “Continuous wave Doppler-free spectroscopy on the $A\,^2\Sigma^+ \leftarrow X\,^2\Pi_{3/2}$ transition in thermal nitric oxide.” PhD thesis. 5th Institute of Physics, University of Stuttgart, 2022 (cit. on pp. ii, 2, 17, 23, 33, 37–39, 43).

[17] L. Neuhaus et al. “PyRPL (Python Red Pitaya Lockbox) — An open-source software package for FPGA-controlled quantum optics experiments.” In: *2017 Conference on Lasers and Electro-Optics Europe & European Quantum Electronics Conference (CLEO/Europe-EQEC)*. 2017, pp. 1–1. DOI: 10.1109/CLEOE-EQEC.2017.8087380 (cit. on pp. ii, 41).

[18] Y. Ogi et al. “Laser-induced amplified spontaneous emission from the 3d and nf Rydberg states of NO.” In: *Chemical Physics* 255.2-3 (May 2000), pp. 379–395. DOI: 10.1016/s0301-0104(00)00043-4 (cit. on pp. iii, 15, 20–23, 87, 89).

[19] A. L. Goodgame et al. “The Stark effect in the $v^+ = 1$ autoionizing Rydberg states of NO.” In: *The Journal of Chemical Physics* 116.12 (Mar. 2002), pp. 4922–4937. DOI: 10.1063/1.1450552 (cit. on pp. iii, 25, 26, 29, 109, 126).

[20] A. Fujii and N. Morita. “Three-color triple resonance spectroscopy of highly excited *ng* Rydberg states of NO: Decay dynamics of high-*l* Rydberg states.” In: *The Journal of Chemical Physics* 103.14 (Oct. 1995), pp. 6029–6039. DOI: 10.1063/1.470431 (cit. on pp. iii, 109, 126).

[21] E. Fermi. “Sopra lo Spostamento per Pressione delle Righe Elevate delle Serie Spettrali.” In: *Il Nuovo Cimento* 11.3 (Mar. 1934), pp. 157–166. DOI: 10.1007/bf02959829 (cit. on pp. iv, 114–116, 118, 127).

[22] E. Amaldi and E. Segré. “Effect of Pressure on High Terms of Alkaline Spectra.” In: *Nature* 133.3352 (Jan. 1934), pp. 141–141. DOI: 10.1038/133141a0 (cit. on pp. iv, 114).

[23] C. Füchtbauer, P. Schulz, and A. F. Brandt. “Verschiebung von hohen Serienlinien des Natriums und Kaliums durch Fremdgase, Berechnung der Wirkungsquerschnitte von Edelgasen gegen sehr langsame Elektronen.” In: *Zeitschrift für Physik* 90.5-6 (May 1934), pp. 403–415. DOI: 10.1007/bf01334059 (cit. on pp. iv, 118, 119, 121, 127).

[24] K. H. Weber and K. Niemax. “Impact broadening and shift of RbnS and nD levels by noble gases.” In: *Zeitschrift für Physik A Atoms and Nuclei* 307.1 (Mar. 1982), pp. 13–24. DOI: 10.1007/bf01416067 (cit. on pp. iv, 118, 119, 121, 127).

[25] F. Munkes et al. *Collisional shift and broadening of Rydberg states in nitric oxide at room temperature*. 2023. DOI: 10.48550/ARXIV.2310.18256 (cit. on pp. iv, 113).

[26] L. Gustafsson et al. “Endogenous nitric oxide is present in the exhaled air of rabbits, guinea pigs and humans.” In: *Biochemical and Biophysical Research Communications* 181.2 (Dec. 1991), pp. 852–857. DOI: 10.1016/0006-291x(91)91268-h (cit. on pp. iv, 2).

[27] W. P. Arnold et al. “Nitric oxide activates guanylate cyclase and increases guanosine 3′:5′-cyclic monophosphate levels in various tissue preparations.” In: *Proceedings of the National Academy of Sciences* 74.8 (Aug. 1977), pp. 3203–3207. DOI: 10.1073/pnas.74.8.3203 (cit. on pp. iv, 2).

[28] R. F. Furchgott and J. V. Zawadzki. “The obligatory role of endothelial cells in the relaxation of arterial smooth muscle by acetylcholine.” In: *Nature* 288.5789 (Nov. 1980), pp. 373–376. DOI: 10.1038/288373a0 (cit. on pp. iv, 2).

[29] L. J. Ignarro et al. “Endothelium-derived relaxing factor produced and released from artery and vein is nitric oxide.” In: *Proceedings of the National Academy of Sciences* 84.24 (Dec. 1987), pp. 9265–9269. DOI: 10.1073/pnas.84.24.9265 (cit. on pp. iv, 2).

[30] L. J. Ignarro. “Nitric oxide is not just blowing in the wind.” In: *British Journal of Pharmacology* 176.2 (Dec. 2018), pp. 131–134. DOI: 10.1111/bph.14540 (cit. on pp. iv, 2).

[31] The Nobel Foundation. *The Nobel Prize in Physiology or Medicine*. 1998. URL: https://www.nobelprize.org/prizes/medicine/1998/summary/ (visited on 09/26/2023) (cit. on pp. iv, 2).

[32] “ATS/ERS Recommendations for Standardized Procedures for the Online and Offline Measurement of Exhaled Lower Respiratory Nitric Oxide and Nasal Nitric Oxide, 2005.” In: *American Journal of Respiratory and Critical Care Medicine* 171.8 (Apr. 2005), pp. 912–930. DOI: 10.1164/rccm.200406-710st (cit. on pp. iv, 2).

[33] D. Djekic et al. “A 0.1 % THD, 1 MΩ to 1 GΩ Tunable, Temperature-Compensated Transimpedance Amplifier Using a Multi-Element Pseudo-Resistor.” In: *IEEE Journal of Solid-State Circuits* 53.7 (July 2018), pp. 1913–1923. DOI: 10.1109/jssc.2018.2820701 (cit. on pp. 2, 81).

[34] P. Kaspar et al. “Doppler-free high-resolution continuous-wave optical UV spectroscopy on the $A\,^2\Sigma^+ \leftarrow X\,^2\Pi_{3/2}$ transition in nitric oxide.” In: *Phys. Rev. A* 106 (6 Dec. 2022), p. 062816. DOI: 10.1103/PhysRevA.106.062816 (cit. on pp. 2, 23, 47, 48).

[35] R. González-Férez, J. Shertzer, and H. Sadeghpour. “Ultralong-Range Rydberg Bimolecules.” In: *Physical Review Letters* 126.4 (Jan. 2021). DOI: 10.1103/physrevlett.126.043401 (cit. on pp. 2, 127).

[36] G. Haklar et al. “Different kinds of reactive oxygen and nitrogen species were detected in colon and breast tumors.” In: *Cancer Letters* 165.2 (Apr. 2001), pp. 219–224. DOI: 10.1016/s0304-3835(01)00421-9 (cit. on p. 2).

[37] S. K. (Choudhari) et al. “Nitric oxide and oral cancer: A review.” In: *Oral Oncology* 48.6 (June 2012), pp. 475–483. DOI: 10.1016/j.oraloncology.2012.01.003 (cit. on p. 2).

[38] W. XU et al. “The role of nitric oxide in cancer.” In: *Cell Research* 12.5-6 (Dec. 2002), pp. 311–320. DOI: 10.1038/sj.cr.7290133 (cit. on p. 2).

[39] F. H. Khan et al. “The Role of Nitric Oxide in Cancer: Master Regulator or NOt?” In: *International Journal of Molecular Sciences* 21.24 (Dec. 2020), p. 9393. DOI: 10.3390/ijms21249393 (cit. on p. 2).

[40] D. D. Thomas et al. “The chemical biology of nitric oxide: Implications in cellular signaling.” In: *Free Radical Biology and Medicine* 45.1 (July 2008), pp. 18–31. DOI: 10.1016/j.freeradbiomed.2008.03.020 (cit. on p. 2).

[41] N. Tuteja et al. “Nitric Oxide as a Unique Bioactive Signaling Messenger in Physiology and Pathophysiology.” In: *Journal of Biomedicine and Biotechnology* 2004.4 (2004), pp. 227–237. DOI: 10.1155/s1110724304402034 (cit. on p. 2).

[42] G. Herzberg. *Spectra of Diatomic Molecules*. Second Edition. Vol. 1. Molecular Spectra and Molecular Structure. D. Van Nostrand Company, Inc., 1950 (cit. on pp. 5–13, 16, 17, 19).

[43] J. M. Brown and A. Carrington. *Rotational Spectroscopy of Diatomic Molecules*. Cambridge Molecular Science. Cambridge University Press, 2003. DOI: 10.1017/CBO9780511814808 (cit. on pp. 5, 8–14).

[44] T. L. Brown. *Chemistry: The central science*. Prentice-Hall, 1977. ISBN: 0-13128-769-9 (cit. on p. 5).

[45] J. S. Winn. *Physical Chemistry*. Harpercollins College Publishers, 1995. ISBN: 0-06047-148-4 (cit. on pp. 5, 15).

[46] H. Haken and H. C. Wolf. *Molekülphysik und Quantenchemie*. Springer Berlin Heidelberg, Mar. 22, 2006. 556 pp. ISBN: 3-540-30314-6 (cit. on pp. 5, 7).

[47] K. Kaufmann, C. Nager, and M. Jungen. “Rydberg states and quantum defects of the NO molecule.” In: *Chemical Physics* 95.3 (May 1985), pp. 385–390. DOI: 10.1016/0301-0104(85)80161-0 (cit. on pp. 5, 23, 30, 125).

[48] M. Born and R. Oppenheimer. “Zur Quantentheorie der Molekeln.” In: *Annalen der Physik* 389.20 (1927), pp. 457–484. DOI: 10.1002/andp.19273892002 (cit. on p. 5).

[49] P. M. Morse. “Diatomic Molecules According to the Wave Mechanics. II. Vibrational Levels.” In: *Physical Review* 34.1 (July 1929), pp. 57–64. DOI: 10.1103/physrev.34.57 (cit. on p. 7).

[50] National Institute of Standards and Technology (NIST). *NIST Chemistry WebBook – Nitric oxide*. URL: https://webbook.nist.gov/cgi/cbook.cgi?ID=C10102439 (visited on 09/28/2023) (cit. on pp. 8, 10, 22, 23, 87).

[51] W. Ubachs. *Notes on: Molecular Physics*. Vrije Universiteit Amsterdam. 2004. URL: http://www.nat.vu.nl/~wimu/MolPhysDic_tot.fr.pdf (visited on 08/24/2023) (cit. on pp. 13, 17).

[52] J. M. Brown et al. “The labeling of parity doublet levels in linear molecules.” In: *Journal of Molecular Spectroscopy* 55.1-3 (Mar. 1975), pp. 500–503. DOI: 10.1016/0022-2852(75)90291-x (cit. on p. 14).

[53] F. Munkes. “Continuous-wave absorption spectroscopy on the $X\,^2\Pi_{1/2}$ to $A\,^2\Sigma^+$ transition of nitric oxide.” Master’s thesis. 5th Institute of Physics, University of Stuttgart, 2019 (cit. on pp. 15, 51).

[54] E. Miescher and K. P. Huber. In: *Spectroscopy*. Ed. by A. D. Buckingham and D. A. Ramsay. Vol. 3. International Review of Science: Physical Chemistry Series Two. Butterworth & Co Ltd, 1976. Chap. Electronic Spectrum of the NO molecule. ISBN: 0-40870-602-3 (cit. on pp. 15, 19, 22, 23).

[55] S. Mollet. "Rydberg states and photoionisation dynamics of NO and Cl_2." PhD thesis. ETH Zurich, 2013 (cit. on pp. 15, 20, 21, 23).

[56] P. D. Biévre and P. Taylor. "Table of the isotopic compositions of the elements." In: *International Journal of Mass Spectrometry and Ion Processes* 123.2 (Feb. 1993), pp. 149–166. DOI: 10.1016/0168-1176(93)87009-h (cit. on p. 19).

[57] C. E. Mortimer and U. Müller. *Chemie: Das Basiswissen der Chemie*. 10th ed. Thieme, 2010. ISBN: 978-3-13-484310-1 (cit. on p. 19).

[58] Centers for Disease Control and Prevention. *Medical Management Guidelines for Nitrogen Oxides*. URL: https://wwwn.cdc.gov/TSP/MMG/MMGDetails.aspx?mmgid=394%5C&toxid=69 (visited on 09/30/2023) (cit. on p. 19).

[59] M. Schulz-Weiling. "Ultracold Molecular Plasma." PhD thesis. The University of British Columbia, 2017 (cit. on p. 19).

[60] D. X. Wang, C. Haridass, and S. P. Reddy. "The Gamma ($A\,^2\Sigma^+ - X\,^2\Pi^r$) System of the Nitric Oxide Isotopomers." In: *Journal of Molecular Spectroscopy* 175.1 (1996), pp. 73–84. ISSN: 0022-2852. DOI: 10.1006/jmsp.1996.0011 (cit. on p. 21).

[61] J. Brown, A. Cole, and F. Honey. "Magnetic dipole transitions in the far infrared spectrum of nitric oxide." In: *Molecular Physics* 23.2 (Feb. 1972), pp. 287–295. DOI: 10.1080/00268977200100291 (cit. on p. 22).

[62] G. Herzberg and C. Jungen. "Rydberg series and ionization potential of the H2 molecule." In: *Journal of Molecular Spectroscopy* 41.3 (Mar. 1972), pp. 425–486. DOI: 10.1016/0022-2852(72)90064-1 (cit. on pp. 22, 28).

[63] J. Danielak et al. "Reinvestigation of the Emission γ Band System ($A\,^2\Sigma^+$–$X\,^2\Pi$) of the NO Molecule." In: *Journal of Molecular Spectroscopy* 181.2 (1997), pp. 394–402. ISSN: 0022-2852. DOI: 10.1006/jmsp.1996.7181 (cit. on pp. 22, 31, 89).

[64] R. A. Young and R. L. Sharpless. "Excitation of the β, γ, δ, and Ogawa bands of nitric oxide in the association of atomic nitrogen and oxygen." In: *Discuss. Faraday Soc.* 33.0 (1962), pp. 228–256. DOI: 10.1039/df9623300228 (cit. on p. 23).

[65] E. Miescher. "Absorption spectrum of the NO molecule." In: *Journal of Molecular Spectroscopy* 20.2 (June 1966), pp. 130–140. DOI: 10.1016/0022-2852(66)90047-6 (cit. on p. 23).

[66] K. Huber, M. Huber, and E. Miescher. “Rydberg-series of the NO-molecule in the visible and infrared emission spectrum.” In: *Physics Letters* 3.7 (Feb. 1963), pp. 315–316. DOI: 10.1016/0031-9163(63)90171-9 (cit. on p. 23).

[67] Kovács, I. “On the H $^2\Sigma^+$ – H’ $^2\Pi$ perturbation of the NO-molecule.” In: (1963). DOI: 10.5169/SEALS-113396 (cit. on p. 23).

[68] A. Bernard et al. “On the 3d Rydberg states of the NO molecule.” In: *Molecular Physics* 73.1 (May 1991), pp. 221–234. DOI: 10.1080/00268979100101161 (cit. on p. 23).

[69] G. W. F. Drake, ed. *Springer Handbook of Atomic, Molecular, and Optical Physics*. Springer, 2005, p. 1506. ISBN: 9780387208022 (cit. on p. 24).

[70] T. F. Gallagher. *Rydberg atoms*. Cambridge University Press, 1994, p. 495. ISBN: 0521385318 (cit. on pp. 24, 25, 46, 113, 114, 116).

[71] X. Wu et al. “A concise review of Rydberg atom based quantum computation and quantum simulation.” In: *Chinese Physics B* 30.2 (Feb. 2021), p. 020305. DOI: 10.1088/1674-1056/abd76f (cit. on p. 25).

[72] C. H. Greene and C. Jungen. “Molecular Applications of Quantum Defect Theory.” In: *Advances in Atomic and Molecular Physics*. Elsevier, 1985, pp. 51–121. DOI: 10.1016/s0065-2199(08)60141-4 (cit. on pp. 25, 26, 61).

[73] M. J. J. Vrakking. “Lifetimes of Rydberg states in ZEKE experiments. III. Calculations of the dc electric field dependence of predissociation lifetimes of NO.” In: *The Journal of Chemical Physics* 105.17 (Nov. 1996), pp. 7336–7347. DOI: 10.1063/1.472592 (cit. on pp. 25, 26, 28, 29).

[74] R. Patel, N. J. A. Jones, and H. H. Fielding. “Observation of the Stark effect in $v^+ = 0$ Rydberg states of NO with a matrix-diagonalization analysis.” In: *Journal of Physics B: Atomic, Molecular and Optical Physics* 40.7 (Mar. 2007), pp. 1369–1381. DOI: 10.1088/0953-4075/40/7/006 (cit. on pp. 25, 28, 29).

[75] P. Neufeld. “Collisional ionization of Rydberg states in nitric oxide.” Master’s thesis. 5th Institute of Physics, University of Stuttgart, 2022 (cit. on pp. 25, 28, 72).

[76] R. Gilbert and M. Child. “Effects of polarization in the field ionization spectrum of H2O.” In: *Chemical Physics Letters* 187.1-2 (Nov. 1991), pp. 153–160. DOI: 10.1016/0009-2614(91)90500-9 (cit. on p. 28).

[77] S. Fredin et al. “*s* and *d* Rydberg series of NO probed by double resonance multiphoton ionization – Multichannel quantum defect analysis.” In: *Molecular Physics* 60.4 (Mar. 1987), pp. 825–866. DOI: 10.1080/00268978700100571. URL: https://doi.org/10.1080/00268978700100571 (cit. on p. 29).

[78] S. Hogan and M. Rayment. *Private Communication*. 2023 (cit. on p. 30).

[79] Y. Schellander. “Laser stabilisation for a quantum gas experiment.” Bachelor’s thesis. 5th Institute of Physics, University of Stuttgart, 2018 (cit. on p. 37).

[80] Leybold GmbH. *Vakuumpumpensymbole, die in Diagrammen zur Vakuumtechnolo gie verwendet werden*. URL: https://www.leybold.com/de-de/knowledge/vacuum-fundamentals/reference/symbols-used-in-vacuum-technology-diagrams (visited on 10/14/2023) (cit. on p. 39).

[81] K. Jousten, ed. *Handbuch Vakuumtechnik*. Springer Fachmedien Wiesbaden, 2018. DOI: 10.1007/978-3-658-13386-3 (cit. on p. 38).

[82] W. Demtröder. *Laserspektroskopie 1*. Springer Berlin Heidelberg, 2011. DOI: 10.1007/978-3-642-21306-9 (cit. on pp. 38, 46, 47, 49, 68).

[83] C. Tomschitz. “A photoionization scheme to create cold ionic impurities from Rydberg atoms.” Master’s thesis. 5th Institute of Physics, University of Stuttgart, 2018 (cit. on p. 40).

[84] R. V. Pound. “Electronic Frequency Stabilization of Microwave Oscillators.” In: *Review of Scientific Instruments* 17.11 (Nov. 1946), pp. 490–505. DOI: 10.1063/1.1770414 (cit. on p. 41).

[85] R. W. P. Drever et al. “Laser phase and frequency stabilization using an optical resonator.” In: *Applied Physics B Photophysics and Laser Chemistry* 31.2 (June 1983), pp. 97–105. DOI: 10.1007/bf00702605 (cit. on p. 41).

[86] E. D. Black. “An introduction to Pound–Drever–Hall laser frequency stabilization.” In: *American Journal of Physics* 69.1 (Jan. 2001), pp. 79–87. DOI: 10.1119/1.1286663 (cit. on p. 41).

[87] M. Mäusezahl, F. Munkes, and R. Löw. *Tutorial on locking techniques and the manufacturing of vapor cells for spectroscopy* in preparation (cit. on pp. 41, 42).

[88] M. Seltenreich. “Eigenschaften eines digitalen, vielseitigen und erweiterbaren System zur Laserstabilisierung.” Bachelor’s thesis. 5th Institute of Physics, University of Stuttgart, 2021 (cit. on p. 43).

[89] C. J. Foot. *Atomic physics*. Oxford University Press, 2005, p. 331. ISBN: 019-8506-95-3 (cit. on pp. 46, 47, 68).

[90] L. G. Piper and L. M. Cowles. “Einstein coefficients and transition moment variation for the NO($A\,^2\Sigma^+ - X\,^2\Pi$) transition.” In: *The Journal of Chemical Physics* 85.5 (1986), pp. 2419–2422. DOI: 10.1063/1.451098 (cit. on p. 47).

[91] A. B. Callear and I. W. M. Smith. “Fluorescence of nitric oxide. Part 1.—Determination of the mean lifetime of the $A\,^2\Sigma^+$ state.” In: *Trans. Faraday Soc.* 59 (0 1963), pp. 1720–1734. DOI: 10.1039/TF9635901720 (cit. on p. 47).

[92] R. de Vivie and S. D. Peyerimhoff. “Theoretical spectroscopy of the NO radical. I. Potential curves and lifetimes of excited states.” In: *The Journal of Chemical Physics* 89.5 (Sept. 1988), pp. 3028–3043. DOI: 10.1063/1.454958 (cit. on p. 47).

[93] X. Huang and Y. L. Yung. “A Common Misunderstanding about the Voigt Line Profile.” In: *Journal of the Atmospheric Sciences* 61.13 (July 2004), pp. 1630–1632. DOI: 10.1175/1520-0469(2004)061<1630:acmatv>2.0.co;2 (cit. on p. 49).

[94] J. J. Olivero and R. L. Longbothum. “Empirical fits to the Voigt line width: A brief review.” In: *Journal of Quantitative Spectroscopy and Radiative Transfer* 17.2 (Feb. 1977), pp. 233–236. DOI: 10.1016/0022-4073(77)90161-3 (cit. on p. 49).

[95] D. Weller et al. “Charge-induced optical bistability in thermal Rydberg vapor.” In: *Phys. Rev. A* 94 (6 Dec. 2016), p. 063820. DOI: 10.1103/PhysRevA.94.063820 (cit. on p. 51).

[96] F. Ripka et al. “A room-temperature single-photon source based on strongly interacting Rydberg atoms.” In: *Science* 362.6413 (2018), pp. 446–449. DOI: 10.1126/science.aau1949 (cit. on p. 51).

[97] F. Christaller et al. “Transient Density-Induced Dipolar Interactions in a Thin Vapor Cell.” In: *Phys. Rev. Lett.* 128 (17 Apr. 2022), p. 173401. DOI: 10.1103/PhysRevLett.128.173401 (cit. on p. 51).

[98] Y. Schellander. “Ionization current measurements of Rydberg states in nitric oxide created by continuous-wave three-photon excitation.” Master’s thesis. 5th Institute of Physics, University of Stuttgart, 2020 (cit. on pp. 51, 69).

[99] J. Fabian. “Design einer elektrisch kontaktierten Durchflusszelle zur Detektion von Ionisationsströmen von Rydbergzuständen Stickstoffmonoxids.” Bachelor’s thesis. 5th Institute of Physics, University of Stuttgart, 2020 (cit. on p. 51).

[100] SCHOTT Technical Glass Solutions GmbH. *BOROFLOAT® 33 – Optical Properties*. URL: https://media.schott.com/api/public/content/aafd6d00012848ee922283e3f2ae1a94?v=9e7ab09a&download=true (visited on 08/17/2023) (cit. on p. 52).

[101] J. Anders. *Records of lecture on “Integrated Interface Circuits”*. University of Stuttgart, Institute of Smart Sensors, 2019 (cit. on pp. 54–57, 59).

[102] P. C. D. Hobbs. “Photodiode Front Ends, The REAL story.” In: *Optics & Photonics News* (Apr. 1, 2001) (cit. on pp. 54, 55).

[103] D. Ying and D. A. Hall. “Current Sensing Front-Ends: A Review and Design Guidance.” In: *IEEE Sensors Journal* 21.20 (Oct. 2021), pp. 22329–22346. DOI: 10.1109/jsen.2021.3094830 (cit. on pp. 55, 56, 60, 62).

[104] M. Rajabzadeh et al. “Comparison Study of Integrated Potentiostats: Resistive-TIA, Capacitive-TIA, CT ΣΔ Modulator.” In: *2018 IEEE International Symposium on Circuits and Systems (ISCAS)*. 2018, pp. 1–5. DOI: 10.1109/ISCAS.2018.8351029 (cit. on pp. 55, 56, 62).

[105] L. Baumgärtner. “Design of a Current–Mode Sigma Delta Modulator.” Master’s thesis. Institute of Smart Sensors, University of Stuttgart, 2020 (cit. on p. 56).

[106] J. G. Graeme. *Photodiode Amplifiers. OP AMP Solutions*. McGraw-Hill Professional, 1995, p. 252. ISBN: 9780070242470 (cit. on pp. 56, 57, 60, 61, 66).

[107] H. Göbel. *Einführung in die Halbleiter-Schaltungstechnik*. Springer Berlin Heidelberg, 2019. DOI: 10.1007/978-3-662-56563-6 (cit. on pp. 56–59).

[108] U. Tietze and C. Schenk. *Halbleiter-Schaltungstechnik*. 4th Edition. Springer-Verlag, 1978 (cit. on pp. 57, 59, 91).

[109] Analog Devices. *LTspice*. Version 17.1.14.0. Sept. 26, 2023. URL: https://www.analog.com/en/design-center/design-tools-and-calculators/ltspice-simulator.html (cit. on pp. 58, 64, 67).

[110] U. Tietze, C. Schenk, and E. Gamm. *Halbleiter-Schaltungstechnik*. 16th Edition. Springer Vieweg, 2019 (cit. on pp. 58, 59, 89).

[111] L. Baumgärtner. *Private Communication*. 2023 (cit. on p. 59).

[112] D. Djekic et al. “A 440-kOhm to 150-GOhm Tunable Transimpedance Amplifier based on Multi-Element Pseudo-Resistors.” In: *ESSCIRC 2021 - IEEE 47th European Solid State Circuits Conference (ESSCIRC)*. IEEE, Sept. 2021. DOI: 10.1109/esscirc53450.2021.9567831 (cit. on pp. 60, 80, 81).

[113] H. Schutz et al. “Current Mode Communication Scheme for Subretinal Implants with 8mV RMS Wire Potential.” In: *2018 25th IEEE International Conference on Electronics, Circuits and Systems (ICECS)*. IEEE, Dec. 2018. DOI: 10.1109/icecs.2018.8618050 (cit. on pp. 60, 61).

[114] Analog Devices. *Data Sheet ADA4817-1/ADA4817-2*. URL: https://www.analog.com/media/en/technical-documentation/data-sheets/ADA4817-1_4817-2.pdf (visited on 10/01/2023) (cit. on p. 63).

[115] Altium. *Altium Designer*. URL: https://www.altium.com/de (cit. on pp. 65, 66).

[116] Texas Instruments. *Data Sheet/ Specifications LMP7721*. URL: https://www.ti.com/product/de-de/LMP7721 (visited on 10/01/2023) (cit. on p. 66).

[117] Linear Technology. *Data Sheet LTC6268/LTC6269*. URL: https://www.analog.com/media/en/technical-documentation/data-sheets/62689f.pdf (visited on 10/01/2023) (cit. on pp. 66, 80).

[118] W. Demtröder. *Experimentalphysik 2*. Springer Berlin Heidelberg, 2017. DOI: 10.1007/978-3-662-55790-7 (cit. on p. 80).

[119] C. M. Western. *PGOPHER version 10.1*. University of Bristol Research Data Repository, 2018. DOI: 10.5523/bris.3mqfb4glgkr8a2rev7f73t300c (cit. on pp. 87, 89).

[120] F. Anschütz. "Optimierung des Messsignals eines Spurengassensors für Stickstoffmonoxid mittel einer zweistufigen Lock-In-Technik." Bachelor's thesis. 5th Institute of Physics, University of Stuttgart, 2023 (cit. on pp. 88, 89, 91, 92, 126).

[121] N. J. A. Jones et al. "Observation of the Stark effect in $v^+ = 0$ Rydberg states of NO: a comparison between predissociating and bound states." In: *Journal of Physics B: Atomic, Molecular and Optical Physics* 41.18 (Sept. 2008), p. 185102. DOI: 10.1088/0953-4075/41/18/185102 (cit. on p. 96).

[122] E. Eder. "Entwicklung und Optimierung des elektrischen Feldes in einer Durchflusszelle zur Detektion von Rydbergzuständen in Stickstoffmonoxid." Bachelor's thesis. 5th Institute of Physics, University of Stuttgart, 2023 (cit. on pp. 103–105, 126).

[123] M. L. Cohen. "The Fermi atomic pseudopotential." In: *American Journal of Physics* 52.8 (Aug. 1984), pp. 695–703. DOI: 10.1119/1.13572 (cit. on pp. 114, 115).

[124] J. B. Balewski. "A single electron in a Bose-Einstein condensate." PhD thesis. 5th Institute of Physics, University of Stuttgart, 2014 (cit. on pp. 114–116).

[125] C. R. Gould and E. I. Sharapov. "Fermi's favorite figure: the history of the pseudopotential concept in atomic physics and neutron physics." In: *The European Physical Journal H* 47.1 (Sept. 2022). DOI: 10.1140/epjh/s13129-022-00042-z (cit. on p. 114).

[126] A. Omont. "On the theory of collisions of atoms in rydberg states with neutral particles." In: *Journal de Physique* 38.11 (1977), pp. 1343–1359. DOI: 10.1051/jphys:0197700380110134300 (cit. on p. 114).

[127] M. N. Hughes. "Relationships between nitric oxide, nitroxyl ion, nitrosonium cation and peroxynitrite." In: *Biochimica et Biophysica Acta (BBA) - Bioenergetics* 1411.2-3 (May 1999), pp. 263–272. DOI: 10.1016/s0005-2728(99)00019-5 (cit. on p. 119).

[128] H. Kübler and J. P. Shaffer. "A read-out enhancement for microwave electric field sensing with Rydberg atoms." In: *Quantum Technologies 2018*. Ed. by A. J. Shields, J. Stuhler, and M. J. Padgett. SPIE, Mar. 2018. DOI: 10.1117/12.2309386 (cit. on p. 120).

Ehrenwörtliche Erklärung

Schriftliche Bestätigung der eigenständig erbrachten Leistung gemäß §6 Absatz 2 der Promotionsordnung der Universität Stuttgart

Die eingereichte Dissertation zum Thema

Electrical detection of Rydberg interactions in nitric oxide at room temperature

stellt meine eigenständig erbrachte Leistung dar.

Ich habe ausschließlich die angegebenen Quellen und Hilfsmittel benutzt. Wörtlich oder inhaltlich aus anderen Werken übernommene Angaben habe ich als solche kenntlich gemacht.

Die Richtigkeit der hier getätigten Angaben bestätige ich und versichere, nach bestem Wissen die Wahrheit erklärt zu haben.

Stuttgart, den 3. November 2023 Fabian Munkes